Numerical analysis of blood flow patterns in simplified aortic root with prescribed valve kinematics

G. Fagioli

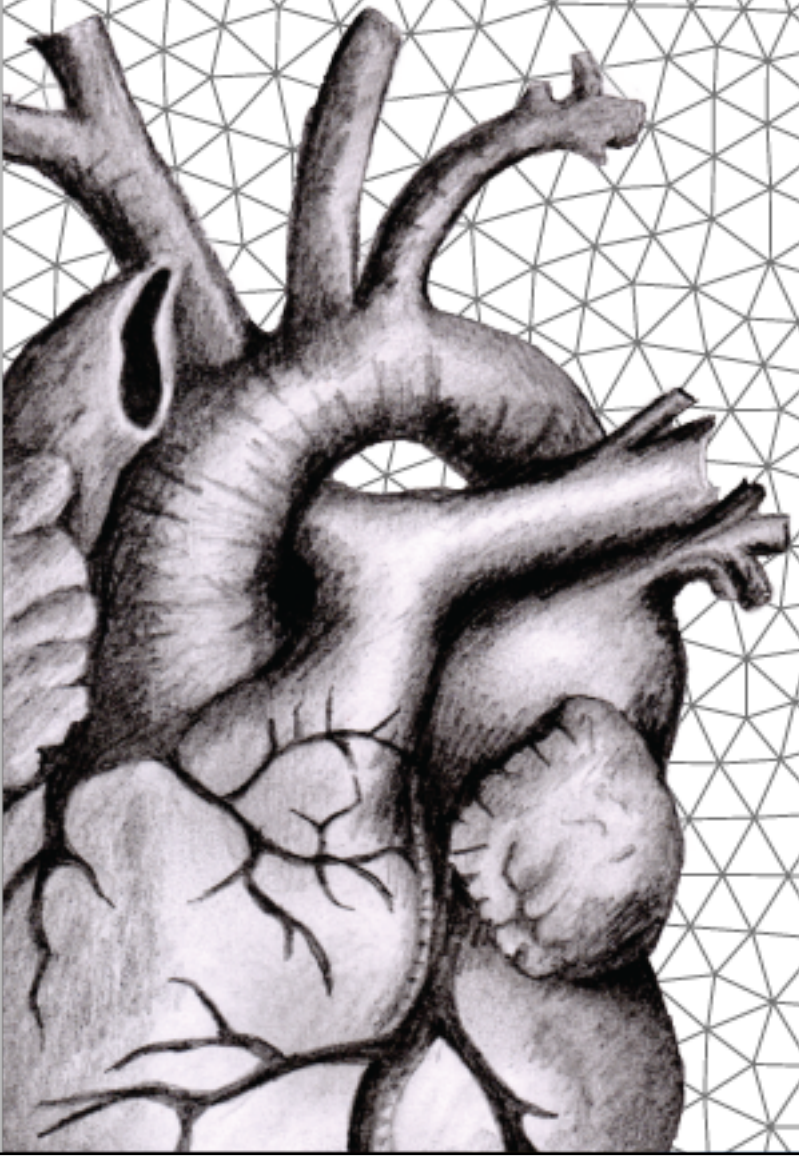

TU Delft Delft University of Technology

Challenge the future

Numerical analysis of blood flow patterns in simplified aortic root with prescribed valve kinematics

by

Giorgio Fagioli

For the degree of Master of Science in Solid and Fluid Mechanics
at Delft University of Technology.

Student number:	4420152	
Department :	Process & Energy (P&E)	
Thesis defence:	28 June 2017	
Thesis committee:	Prof. Dr. Ir. C. Poelma,	TU Delft, chairman
	Prof. Dr. S. Kenjereš,	TU Delft, supervisor
	Prof. Dr. R. Delfos,	TU Delft, committee member
	Dr. Ir. F. Gijsen,	Erasmum MC, guest member

The work in this thesis was supported by the Erasmus Medical Centre of Rotterdam. Their cooperation is hereby gratefully acknowledged.
The research of this thesis was performed under the supervision of Dr. Saša Kenjereš in the Transport Phenomena group of the Applied Physics department.

Abstract

The aortic valve is a valve made of three thin flexible leaflets which open and close in order to allow the unidirectional passage of blood from the left ventricle to the aorta. Because of this repetitive motion at each cycle, the valve is constantly exposed to large variations of pressure and hemodynamic forces. Deterioration in its peculiar functioning could lead to the arising of valvular diseases such as stenosis or regurgitation. A widely spread procedure to cure severely damaged heart valves is the replacement with artificial heart valves. However, up to now, the natural aortic valve properties and functionalities have never been equalised by any manufactured prototypes in terms of efficiency and durability. This limitation has inspired many engineering researches with the purpose of gaining a complete understanding on the working principles of the valve and the evolution of the flow through it in order to enhance the performances of these medical devices.

In this thesis, numerical simulations of blood passing through the aortic valve have been performed. In particular, this study proposes an alternative investigating approach which consists on prescribing the rigid motion of the leaflets *a priori* as taken from experimental values and without the employment of the structural solver. To execute this strategy, the Arbitrary Lagrangian-Euler method along with remeshing techniques has been employed in Ansys Fluent. The main objectives concerned the study of the resulting hemodynamics in the aortic root and the validation with other investigating techniques such as experimental work and Fluid-Structure Interaction simulations.

First, the methodology was tested in a two-dimensional geometry which embodied a simplified representation of the aortic root. The results highlighted the development of two counter-rotating vortices when the valve reached its closed position. Secondly, a more realistic three-dimensional case was analysed with the employment of a commercial bileaflet mechanical valve. In this case, two different methods were adopted to deal with the transition of the flow to a turbulent regime. Namely, the analysis was conducted by the resolution of the unsteady Reynolds-Averaged Navier-Stokes equations with the k-ε model and by maintaining a laminar approach. Generally, the hemodynamics is characterised by the gradual development and decay of three jets followed by the formation of vortical structures in the sinus region.

Finally, validation of the method with available experimental data showed that the two-dimensional case is well reproduced. On the other hand, mainly qualitative agreement is obtained for the three-dimensional case. This suggests that the proposed approach is able to capture the main features of the flow to a certain extent and future investigations are required to obtain more accurate predictions of the flow.

"Blame it on a rush of blood to the head.
Blame it on a rush of blood through the heart."

Acknowledgements

From the end of the course of my studies, I look back at the winding path which has led me to this final destination. Although it was plenty of difficulties, I was constantly driven by the willing to do my best not to disappoint myself and the people who I care the most. To tell the truth, I believe that I would not be here writing this thesis if there had not been some important people who accompanied me throughout this long journey. I owe a lot to them and this is the reason why I would like to dedicate this section to whom I need to express my overall gratitude. I also take the opportunity to free that poetic part of me after being immersed in numbers and technical studies for the last past years.

First of all, I would like to wholeheartedly thank my family for all the support in this period abroad. Thank you *Mamma* & *Papà*, to have made this opportunity real and to never stop believing in me when I needed the most. Thanks to my brother, *Lorenzo*, for being always an example to follow and a wise guide. You taught me what one cannot find in books and you gave me the eyes to interpret the world around me.

Thanks to two important friends who have become like family for me, *Maria* & *Luca* aka *La Banda*. Since we started this adventure together, I really cannot think of a day when you did not make me laugh. I am honestly grateful for all the experiences we shared together and for your support in the darkest days.

Thanks to my new flatmates of Doelenplein 4, *Caterina* aka *Caspiterina*, *Francesco* & *Luca*. I cannot believe how we managed to create this intense bond although we only lived together for a short time. Your positivity has cheered my nights and my weekends and you reminded me that there are important matters and priorities which are worth fighting for.

Another sincere thank goes to the old good friends back in Rome or spread all over Europe. Thanks to *Claudia* & *Daniele* for being like an anchor in a wavy sea. I know that I can always count on you no matter the distance. Thanks to *Elena* who was always there whenever I was about to abandon everything. I really miss being student partners as we used to be in the Bachelor. Although we chose different specialisations, we know we could always rely on each other's help. Naturally, there is much more than this "nerdy" connection and I hope our friendship will be as genuine and plenty of laughing in the future as it has always been.

From the academic point of view, needless to say, a big "hvala" to *Saša* for his constant supervision throughout the project. You were always available to answer all my questions and doubts and to help me at any time. I will never forget the valuable discussions during personal and group meetings. It was certainly an enriching experience from which I have learnt a lot. Thanks to *Saeid* and *Fei* for their contribution in my work and for all the precious technical suggestions. Thanks to *Edoardo*, not only for his collaboration from the

professional point of view but also for bearing all my complaints and for making my working days at university more pleasant.

Last but not least, I would like to thank professor *Roberto Verzicco* because I would not have probably chosen this master specialisation if he did not transmit me the passion for this subject.

Delft, University of Technology G. Fagioli

Table of Contents

Acknowledgements **v**

Preface **xvii**

Glossary **xix**

List of Acronyms . . . xix

List of Symbols . . . xx

1 General Introduction **1**

1.1 The normal aortic valve . . . 2

1.1.1 Anatomical description . . . 2

1.1.2 The role of the aortic valve in the circulatory system . . . 4

1.2 Mechanical heart valve prostheses . . . 5

1.3 Research goal and outline of the report . . . 7

2 Literature Review **9**

2.1 Dynamics of the normal aortic valve . . . 10

2.2 Geometrical description of the normal aortic valve . . . 11

2.3 Fluid dynamics of the aortic valve . . . 15

2.4 Fluid-structure interaction models . . . 17

2.5 Discussion . . . 19

2.5.1 Dynamic mesh and governing equation . . . 19

3 2D analysis and validation **21**

3.1 Introduction and experimental method . . . 21

3.2 Geometry and mesh of the computational model . . . 22

3.3 Boundary conditions . . . 25

3.4 Valve motion and dynamic mesh . . . 26

3.5 Simulation methods . . . 28

3.6 Results and validation . . . 29

3.7 Comparison with two-way FSI . . . 35

3.8 Summary . . . 37

4 3D analysis and validation **39**
4.1 Introduction . . . 39
4.2 Experimental model . . . 40
4.3 Geometry and mesh of the computational domain . . . 41
4.4 Boundary conditions . . . 44
4.5 Valve motion and dynamic mesh . . . 45
4.6 Simulation methods . . . 48
4.7 Results . . . 49
4.8 Validation . . . 54
4.9 Summary . . . 58

5 Conclusions & Recommendations **59**
5.1 General conclusions . . . 59
5.2 Recommendations for future research . . . 60

A Mathematical models **63**
A.1 Analytical representation of the geometry of the natural AV . . . 63
A.1.1 Open valve representation . . . 63
A.1.2 Closed valve configuration . . . 67

B Dynamic mesh theory **69**
B.1 Dynamic mesh models . . . 69
B.1.1 Smoothing methods . . . 69
B.1.2 Dynamic layering . . . 72
B.1.3 Remeshing techniques . . . 72
B.1.4 `DEFINE_CG_MOTION` macro . . . 73

C Numerical theory **75**
C.1 Discretisation schemes . . . 75
C.1.1 Spatial discretisation . . . 75
C.1.2 Temporal discretisation . . . 76
C.1.3 Gradient and derivatives evaluation . . . 77
C.2 Pressure interpolation . . . 78
C.3 Pressure-velocity coupling . . . 78

D Mesh validation **81**
D.1 Two-dimensional case . . . 81
D.2 Three-dimensional case . . . 84

E Turbulence models **87**
E.1 Governing equations . . . 87
E.2 k-ε model . . . 88
E.3 Near-wall treatment . . . 89
E.4 Kolmogorov scale estimation . . . 92

F Codes **95**
F.1 Velocity inlet 95
F.1.1 Two-dimensional case 95
F.1.2 Three-dimensional case 96
F.2 Leaflet motion 96
F.2.1 Two-dimensional case 96
F.2.2 Three-dimensional case 97

G **101**

List of Figures

1.1 Frontal section of the human heart: the position of the aortic root is highlighted in yellow [4]. . . . 2

1.2 Drawing of the leaflet surface. The dashed line separates the coaptive surface above from the load bearing surface below. . . . 3

1.3 Representation of the AR. In *(a)*, lateral view which highlights the bulged shape of the sinuses. In *(b)*, top view shows the interconnections between sinuses and leaflets. Pictures are taken from [34]. . . . 3

1.4 Section of the AR: the interleaflet triangles are represented by the dashed zones. Picture adapted from [16]. . . . 4

1.5 Pressure curves in aorta (grey), left atrium (green) and left ventricle (blue) in the heart cycle. The corresponding behaviour of the volume in the LV is also shown (red) [7]. . . . 5

1.6 Examples of artificial heart valve prostheses. . . . 6

2.1 In (*a*), variation of the commissure perimeter as function of aortic pressure [6]. In (*b*), variation of the base perimeter as function of ventricular pressure [16]. . . . 10

2.2 Example of rubber casts [23]. . . . 12

2.3 Schematic of the aortic root highlighting the design parameters used to characterise the modelling according to Thubrikar [21] in *(a)* and Labrosse [24] in *(b)*. . . . 13

2.4 Representation of one leaflet in both closed (shaded) and open (transparent) positions [24]. . . . 14

2.5 Aortic velocity (black dots) and valve opening area (white dots) as functions of time from experimental measurements [25]. . . . 15

2.6 In *(a)*, representation of the bidimensional experimental setup. In *(b)*, sketch of the geometrical domain for the theoretical model. Both pictures are from [26]. . 17

3.1 Schematic representation of the experimental setup: piston (p), diffuser (p), valve section (vs), reservoir (r), stationary pump (sp) and flow meter (fm) [11]. . . . 21

3.2 Particular of the valve section of the experimental setup [11]. . . . 22

3.3 Sketch of the geometrical model for the 2D case. . . . 23

3.4 Overview of the two-dimensional mesh. The leaflet is highlighted in yellow. . . . 24

3.5 Magnified region of the two-dimensional grid. . . . 24

3.6 Flow pulse from experimental measurements with analytical fitting [11]. . . . 25

3.7 Inlet velocity profile U as function of time. Only one cycle is shown. 26
3.8 Leaflet opening angle as a function of time. Circular markers represent experimental data whereas the solid line shows the interpolated values. 27
3.9 Angular velocity of the leaflet as function of time. 27
3.10 Velocity vector plots at five different istants of the flow pulse. The pictures on the right come from PIV measurements [12]. Streamlines are coloured according to velocity magnitude. 30
3.11 Vorticity contours at five different istants of the flow pulse. 31
3.12 Sections along the channel where velocity profiles have been extracted. 32
3.13 Profiles of the x-velocity at the three outlined sections of the channel at five instants of the flow. 32
3.14 Pressure, x-velocity and y-velocity components as function of time for monitor point 1. 33
3.15 Spectra for the signals recorded at monitor point 2. 34
3.16 Quantitative comparison along section B-B of the channel between the FSI (dotted line) and prescribed motion (solid line) approaches. 35
3.17 Overview of the comparison of the streamwise velocity profiles resulted from FSI (red dotted line) and prescribed motion (black dotted line) for five different instants of the cycle. 36
3.18 Leaflet opening angle as function of time for three different methods. 37

4.1 Schematic representation of the experimental setup: piston (P), left ventricle (LV), aortic valve (AV), aortic root (AR), first compliance (C1), second compliance (C2), resistance (R), reservoir (RV) and atrium (A). The red dots indicate the position of the pressure sensors. 41
4.2 Representation of the geometrical domain with detailed views of the mechanical valve in open configuration. 42
4.3 Sketch of the model corresponding to the central cross section $x = 0$. The main lengths are also reported in the drawing. 42
4.4 Top view of the model shows the asymmetric implementation of the valves with respect to the three sinuses. 43
4.5 In *(a)*, an overview of the surface mesh of the domain. In *(b)*, section of the mesh corresponding to the plane $x = 0$. 44
4.6 Velocity inlet profile as function of time for one cycle. 45
4.7 Schematics of the rotational kinematics of the leaflets. The red dots represent the axes of rotation. 46
4.8 Frames of the experimental valve kinematics for different instants of the cycle. Pictures from Cerroni, with permission [13]. 46
4.9 Experimental (symbols) and interpolated (solid line) opening angle as a function of time for the two leaflets of the valve. 47
4.10 Temporal behaviour of the normalised opening angle for the two leaflets and the inlet velocity pulse. 47
4.11 Angular velocity of the two leaflets as function of time. 48
4.12 Sections A-A and B-B along the plane $x = 0$ for flow investigation. 49
4.13 Velocity contours at five different time instants of the flow pulse along x = 0 and at sections A-A and B-B. 50

4.14 Azimuthal vorticity contours ω_x in the plane x = 0 and streamwise vorticity contours ω_z along planes z = 5.41 mm and z = 23.23 mm from the leaflets' tips. . . 52

4.15 Contours of turbulent quantities on the plane x = 0 for the five time instants. The left images show turbulent kinetic energy; the right ones present the eddy viscosity ratio μ_t/μ. 53

4.16 Streamwise velocity component along section A-A in the central plane at five instants of the flow pulse. Different methods are compared: experimental (black line), FSI (green line), laminar (blue line) and turbulent k-ε model (red line). . . 55

4.17 Streamwise velocity component along section B-B in the central plane at five instants of the flow pulse. Different methods are compared: experimental (black line), FSI (green line), laminar (blue line) and turbulent k-ε model (red line). . . 57

A.1 Side view of one leaflet of the aortic valve in both open and closed configurations. The drawing shows the relevant parameters used for the mathematical formulation. 64

A.2 In *(a)*, top view of the valve when $L_f \leq \pi\frac{\sqrt{3}R_c}{2}$. In *(b)*, the same view when $L_f \geq \pi\frac{\sqrt{3}R_c}{2}$. 64

A.3 Side view of the constructed trileaflet AV. One cusp is highlighted with a different brighter shade. 68

A.4 Space view of the constructed trileaflet AV. One cusp is highlighted with a different brighter shade. 68

B.1 Representation of the equivalent structure of the mesh with interconnecting springs. 70

B.2 Dynamic layering model. 72

C.1 Schematic drawing of a two-dimensional grid discretisation. 76

C.2 Implementation of the steps for the two pressure-based solvers. 79

D.1 Two-dimensional coarse grid with magnified gap region. The leaflet is highlighted in yellow. 82

D.2 Mesh dependency check for the x-velocity (left) and y-velocity (right) components. 83

D.3 Top-view comparison of the two meshes for the three-dimensional case. 84

D.4 Instantaneous streamwise velocity comparison between coarser (blue line) and finer (red line) grids at the three monitoring points indicated in the sketch above. . . . 85

D.5 Streamwise velocity comparison along the line A-A (left) and along line B-B (right) between coarser (blue line) and finer (red line) grids for three different instants of the cycle. 86

E.1 Near-wall velocity profile u^+ as function of the dimensionless grid distance y^+. The different near-wall layers are indicated in the plot. 90

E.2 Scatter plot of y^+ for leaflet 1 at flow peak. The line shows the mean value equal to 2.3. 90

E.3 y^+ contours for the aortic root for five different instants in the flow. 91

E.4 Estimation of the ratio between the Kolmogorov scale and the characteristic cell size. 93

List of Tables

2.1 Comparisons of the dimensions of the design parameters of the aortic valve. . . . 14

3.1 Geometrical properties of the valve model. 23
3.2 Summary of the parameters of the two-dimensional mesh. 23
3.3 Parameters for the inlet velocity formulation. 25
3.4 Settings of the parameters for the dynamic mesh methods. 28
3.5 Settings for the two-dimensional simulation. 28
3.6 Coordinate positions of the monitoring points. 33

4.1 Geometrical dimensions of the three-dimensional domain. 41
4.2 Summary of the parameters of the three-dimensional mesh. 43
4.3 Settings of the parameters for the dynamic mesh methods. 48
4.4 Settings of the parameters for the three-dimensional simulations. 49

D.1 Summary of the parameters of the two-dimensional finer mesh. 81
D.2 Summary of the parameters of the three-dimensional finer mesh. 84

Preface

In this section, I would like to explain my personal motivation for having selected the topic of my thesis.

During my course of studies at TU Delft, I had the chance to follow a course entitled "Biological Fluid Mechanics". I was really enthusiastic of the subject for different reasons that turned out to be the driving forces which led the direction of my studies.

To begin with, I was once again intrigued by how wide the range of applicability of fluids is; in fact, it was a complete new topic for me. This contributed to accentuate that sense of thrill and curiosity that is part of the innate nature of human beings when dealing with something new. In particular, I discovered how much the multidisciplinary background could offer a stimulus to boost and widen my knowledge. In other words, engineering intertwines with biology and medicine, creating a new strong bond which allows to tackle a problem through an enriched point of view.

Furthermore, the idea that studies in this topic could bring along several great breakthroughs for the medical field was fundamental. A thorough understanding of the complex phenomena that occur in our body will contribute to meliorate our health in many ways. For instance, the development of some new medical equipment or techniques for surgical operations, the specialisation of decision making in cures or in surgical treatments and improvement of post-intervention care of patients are the most compelling evidence of the powerfulness of this investigation.

Therefore, bearing in mind all these elements, I decided that I wanted to work on a topic related to this matter. I longed for the idea to make my research a useful contribution for science that could also have an impact from a medical point of view. Here, at the TP group at TU Delft, I had the chance to make my ambition possible.

To conclude, I do think that we all care about our health and as meticulous researches in this field allow us to improve the quality of our lives, we are all committed to continuing them in order to find concrete results and eventually foster a better future.

Glossary

List of Acronyms

6DOF	Six Degree of Freedom
ALE	Arbitrary Lagrange-Euler formulation
AR	Aortic Root
AV	Aortic Valve
CURVIB	Curvilinear Immersed Boundary method
CVD	Cardiovascular Disease
DES	Detached Eddy Simulation
DNS	Direct Numerical Simulation
FSI	Fluid-structure Interaction
GCL	Geometric Conservation Law
IB	Immersed Boundary method
LDV	Laser Doppler Velocimetry
LES	Large Eddy Simulation
LV	Left Ventricle
MRI	Magnetic Resonance Imaging
PIV	Particle Image Velocimetry
RANS	Reynolds-Averaged Navier-Stokes
SJM	St. Jude Medical
TKE	Turbulent Kinetic Energy
TP	Transport Phenomena

TU Delft	Delft University of Technology
UDF	User-Defined Function
VHD	Valvular Heart Disease

List of Symbols

α	Leaflet commissural angle
κ	Von Karman's constant
Λ	Dimensionless leaflet opening angle
λ	Leaflet opening ratio
μ	Dynamic viscosity
μ_t	Turbulent viscosity
ν	Kinematic viscosity
Ω	Leaflet angular velocity
ϕ	Leaflet base-plane angle
ρ	Density
τ	Period
θ	Leaflet angle
$\vec{\omega}$	Vorticity field
$\hat{n}$	Normal unit vector
D	3D outlet diameter
d	3D inlet diameter
f	Frequency
H	Valve height
h	2D channel height
I	Turbulent intensity
L	Leaflet length
L_f	Leaflet free-edge length
L_h	Leaflet height
P	Pressure
R	2D sinus radius
r	Fillet radius
Re	Reynolds number
R_b	Base radius
R_c	Commissural radius
St	Strouhal number
t	Time
u_τ	Friction velocity

V	Volume
y^+	Dimensionless wall distance
u, v	Velocity field

1 General Introduction

Cardiovascular diseases (CVDs) are a group of disorders which affect heart and blood vessels. According to the World Health Organisation, approximately 17.1 million people die every year because of CVDs, representing about 30% of the overall global deceases [1]. As a consequence, CVDs are considered to be the main cause of death worldwide.
In addition to a predisposed genetic condition, the most common factors which lead to the development of CVDs are linked to an unhealthy lifestyle quality. This includes high alcohol consumptions, smoke, poor physical activity and incorrect diet.
The major weapon to fight against these aforementioned risks is prevention. As a matter of fact, campaigns have been spread in order to raise awareness of how much harmful these factors are for our health. In particular, in 2013, 194 Nations signed a plan with the aim of reducing the number of premature mortality due to CVDs by 25% by 2025 [2].
Within the group of CVDs, valvular heart diseases (VHDs) represent a category of pathologies which affect heart valves. The heart is divided into four chambers, namely two atria and two ventricles. At the inlet and the outlet of the ventricles, mechanical valves are responsible to regulate the blood flow. Hence, there are four valves in total. Among these, the aortic valve (AV) is the most prone to problems which can be mainly classified into two types, i.e. stenosis and regurgitation [3]. The former is caused by the thickening or stiffening of the leaflets. This impedes the valve to reach its fully open configuration with a consequent obstruction of blood flow. On the other hand, the latter occurs when the valve does not seal properly and it is responsible for a back flow of blood in the ventricle. Clearly, both cases have got a negative effect on the overall efficiency of the pumping function of the heart since additional work load is produced. These problems can be either congenital, meaning that they are present since birth, or they can develop later in time with ageing or because of illnesses such as rheumatic fever. In both situations, the frequent occurrence of these VHDs has given rise to a constant search for better improvements in order to treat these diseases. Undoubtedly, health care intervention is almost necessary and the techniques which are exploited range from artificial heart replacement through mechanical or bioprosthetic valves to direct surgical repair.
Nevertheless, up to now, the natural aortic valve properties and functionalities have never

been equalised by any manufactured prototypes in terms of efficiency and durability. For this reason, researches are still carried out to deeply understand the working principles of the valve and the influences of these diseases on its mechanisms in order to enhance medical devices and applications.
In this matter, the engineering field has gained a major role as it can be helpful to achieve this ultimate goal thanks to powerful and advanced computational methods. In this thesis, attention is brought to the aortic valve. In brief, the design and modelling of its elements and their interconnections with the physiological nature of blood are investigated.

1.1 The normal aortic valve

1.1.1 Anatomical description

The aortic root (AR) is the region which connects the left ventricle (LV) to the ascending aorta, that is the main artery which delivers oxygenated blood to the rest of the body. Figure 1.1 shows a frontal section of the heart with the aim of introducing the different anatomical parts and their names to the reader. In particular, the position of the aortic root is highlighted.

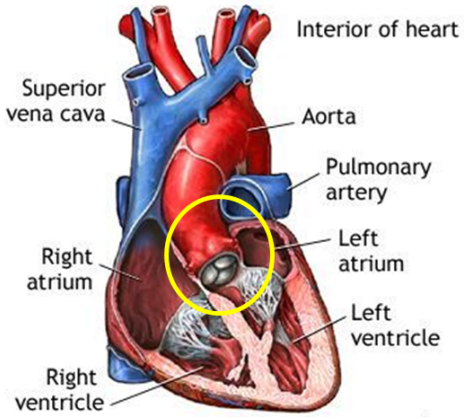

Figure 1.1: Frontal section of the human heart: the position of the aortic root is highlighted in yellow [4].

The aortic root hosts the aortic valve and the sinuses of Valsalva. It is limited distally by the sinotubular junction and inferiorly by the aortic root base. Whereas the former marks a well-defined border through a truly circular structure when viewed from the aorta side, the bottom boundary has been the focus of a debate regarding the description of its shape and name. From the surgical point of view, the lower boundary is generally referred as the aortic ring or annulus because it is used as a reference for the sizing and fitting of prosthetic valves. Actually, thorough anatomical investigations have proved the absence of this continuous circle-like structure [5]; thus, the choice of this name should be considered improper. Nonetheless, an annular shape can be recreated if the points of attachments of the leaflets are ideally joined together. To avoid any future misunderstandings, this part will be addressed with the more generic term of aortic base for the rest of this thesis.

The aortic valve is composed of three highly flexible leaflets or cusps, i.e. the moving components of the system. Two surfaces can be identified in each leaflet. The first one is called *lunula* because of its semi-lunar shape. Furthermore, this area plays an important role when the valve is in its fully closed position as the *lunulae* of adjacent leaflets overlap in order to ensure perfect sealing. For this reason, this part is also called coaptive surface. The second is called load bearing surface as it is the major area which withstands stresses and pressure. In addition, it is the only part that it is visible from the ventricle side.

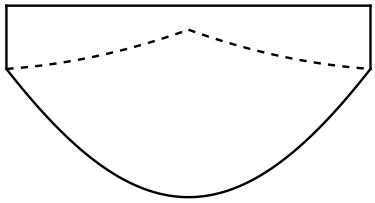

Figure 1.2: Drawing of the leaflet surface. The dashed line separates the coaptive surface above from the load bearing surface below.

At the bottom, the leaflets are hinged to the wall of the aortic root whereas the highest points of the leaflets are found to be in the plane of the sinotubular junction. These points are named commissures. In conclusion, the only free boundary of the leaflet is defined by the top margin of the coaptive surface and it is called free edge.
The sinus cavities create the housing and the necessary space for the leaflets to move. In details, they are three bulged portions of the aortic wall made of a thinner elastic material (Fig. 1.3). They are named according to the presence of the coronary arteries. Hence, the left, the right and the non-coronary sinuses can be distinguished. The role of these components was found to be important in the valvular function both from the mechanical and fluid dynamical points of view. In fact, vortexes which remain entrapped in the cavities are found to aid the closure of the valve and to minimise stresses by preventing contraction of the wall.

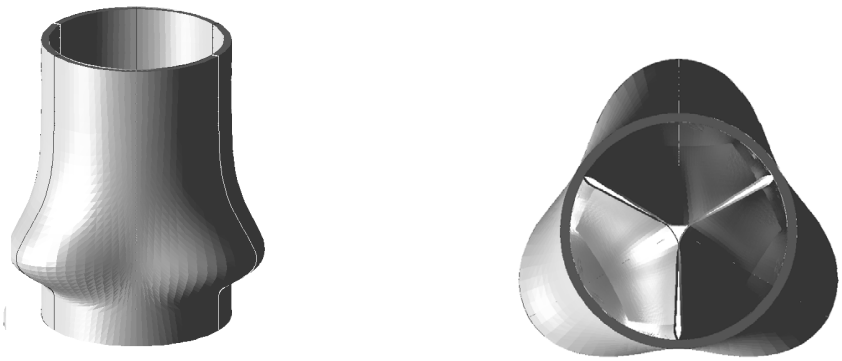

(a) **(b)**

Figure 1.3: Representation of the AR. In *(a)*, lateral view which highlights the bulged shape of the sinuses. In *(b)*, top view shows the interconnections between sinuses and leaflets. Pictures are taken from [34].

Each sinus is separated the one with the other at its base by triangular-like structures known as interleaflet triangles. They are portions of the ventricular wall which are delimited by the lines of attachments of the leaflets and extend up to the level of the commissures. These elements are better seen if a cut is performed as shown in Figure 1.4.

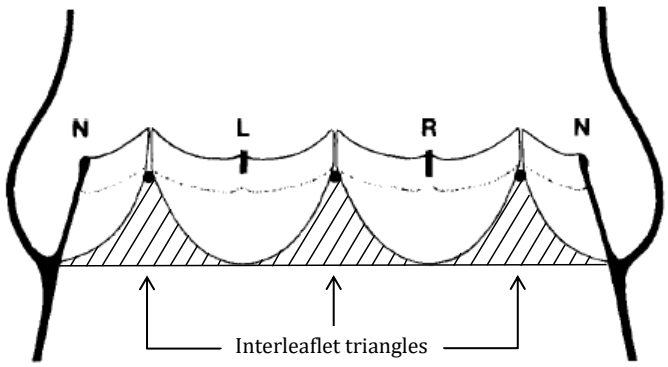

Figure 1.4: Section of the AR: the interleaflet triangles are represented by the dashed zones. Picture adapted from [16].

1.1.2 The role of the aortic valve in the circulatory system

To understand the role and the functioning of the aortic valve within the circulatory system, a very brief explanation of the cardiac cycle is required.
The cardiac cycle is the interval of time which coincides with the duration of the heart beat. It can be divided into four phases, namely diastole, isovolumetric contraction, systole and isovolumetric relaxation.
During diastole, pressure in the left ventricle drops below the pressure of the left atrium, causing the opening of the mitral valve. On the other hand, the aortic valve remains closed at this stage. Blood starts to rapidly fill the left ventricle and a consequent expansion of the chamber to accommodate the fluid takes place.
When the mitral valve closes, the isovolumetric contraction interval begins. In this phase, both valves are closed and pressure rises considerably with no change in volume.
When the increasing left ventricle pressure exceeds the pressure in the aorta, the aortic valve opens. This determines the onset of systole. This phase is characterised by the contraction of the left ventricle which pushes blood into the ascending aorta. First, blood is rapidly ejected into the artery; later, as the ventricular pressure starts to decline, it flows more slowly. The systolic phase ceases when the aortic valve closes. After this, the isovolumetric relaxation follows. The ventricle relaxes without any change of volume and pressure falls significantly. This completes the sequence and the cycle may start over.
Figure 1.5 summarises the behaviour of pressure in the aorta, left ventricle and left atrium as a function of time. Indications relative to the opening and closing of the valves and the names of the different phases in the cycles are also shown.

From what stated above, it appears clear that the main function of the aortic valve is to

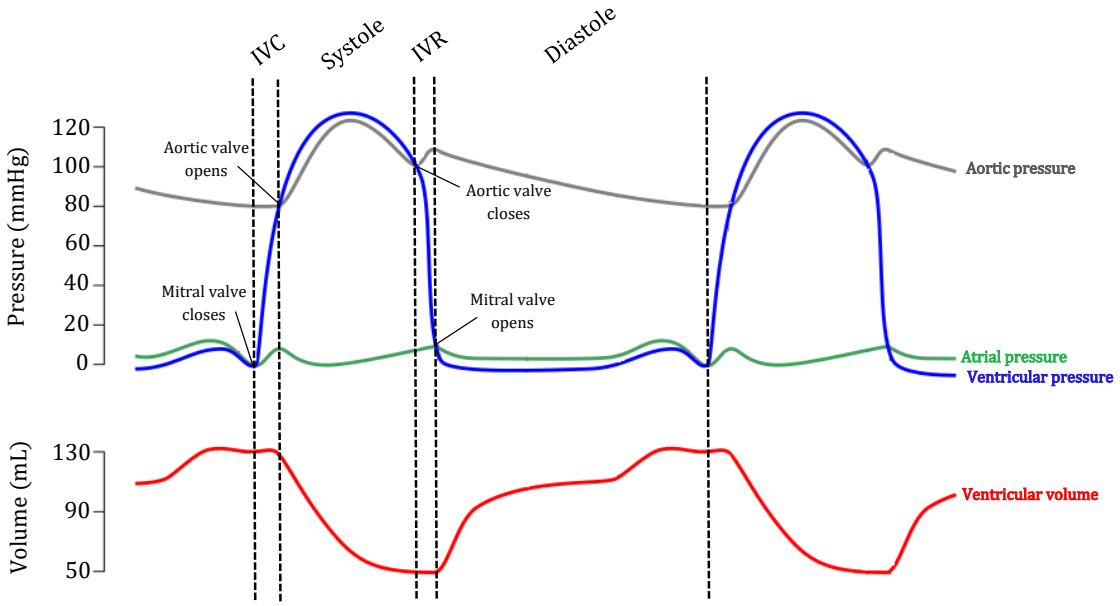

Figure 1.5: Pressure curves in aorta (grey), left atrium (green) and left ventricle (blue) in the heart cycle. The corresponding behaviour of the volume in the LV is also shown (red) [7].

let blood flow in only one direction and to prevent back flow into the left ventricle. It is important that this process takes place without causing any resistance to the flow. The aortic valve was thought to be a passive component. Nonetheless, several studies have proved the contrary. In fact, it is considered to be a dynamic structure as it is able to adapt to changes of aortic pressure and ventricular pressure. During opening, the base perimeter is at its maximum, allowing movement of the leaflet outwards. Furthermore, it helps reducing the bending stresses on the coaptation line. During closing, the shrinkage of the base perimeter displaces the leaflets inwards, reducing the distance to travel so it guarantees complete closure of the orifice [6]. Hence, it appears clear that all its components must work in harmony in order to guarantee normal functioning.

1.2 Mechanical heart valve prostheses

Artificial heart valves have been widely used in the recent years in order to cure diseased heart valves whenever direct surgical repair is not possible. This occurs when the valve is severally damaged, representing a risk for human health. Every year about 290 000 heart valve replacements are completed worldwide and this number is expected to grow annually at a rate of 10-12% [8]. There are two categories of heart valve prostheses: biological or bioprosthetic and mechanical valves (Fig. 1.6).

Bioprostethic valves are similar in structure to the normal aortic valve as they are characterised by three flexible leaflets. They are made of biological material which can have either animal (porcine or bovine tissues) or human origins. The main advantage of this group of valves is better seen in terms of their hemodynamical performances. In fact, biological valves

do not drastically change the fluid dynamics of blood since pressure gradients and flow behaviour resemble those of the natural valve. Nevertheless, they are gradually exposed to wear due to mechanical stresses and calcification of tissues. Generally, their expected lifespan is between 10 to 15 years, after which they need to be replaced.

Mechanical valves are usually manufactured from carbon. They are characterised by a closing mechanism which regulates the passage of blood. The overall structure is made of three principal components:

- the *occluder*, the mobile part of the prosthesis, must be able to open and close without causing any restriction to the flow;
- the *housing*, which has got the function of driving and limiting the movement of the occluder;
- the *sewing ring*, which connects the prosthesis to the cardiac tissues.

The principal advantage of mechanical heart valves is represented by their good durability. However, alteration of the physiological blood patterns are found to enhance platelet activation; this activity leads to harmful consequences such as thrombosis. Thus, the patient needs to follow a lifelong anticoagulation therapy.

(a) Mechanical valve [9]. **(b)** Biological valve [10].

Figure 1.6: Examples of artificial heart valve prostheses.

Various mechanical heart valve designs have been developed. They mainly differ in terms of geometry, manufacturing materials and number of leaflets. The first attempt of heart valve replacement dates back to 1952 when Dr. Charles Hufnagel performed the implementation of the so-called ball-caged prosthesis in the descending aorta of a patient. In this design, a ball which lays on a metal ring is contained within a cage. In the closed state, the ball blocks the orifice creating a tight seal and low leakage. Although the ball is pushed towards the cage during forward flow, it remains in the main flow area. Consequentially, the shortcomings of this design are high shear stresses and excessive induced turbulent through the valve [8]. An additional improvement was achieved upon the introduction of the Bjork-Shiley prosthesis in

1967. The working principle is based on an oscillating tilting disc which is able to move aside at a specific angle in the open position. Therefore, the flow disturbance is minimised with respect to the previous configuration. The most popular mechanical design is represented by the bileaflet mechanical heart valve. It was first manufactured by St Jude Medical Inc. (SJM) in 1978. This prosthesis is composed of two semicircular carbon discs with pyrolytic coating. Each disc is able to pivot about a hinge, creating three orifices for the flow. The central one is rectangular whereas the two lateral ones have got a semicircular shape. More recent designs are based on the SJM model. Several progresses have been possible as a result of modified parameters such as shape of the leaflets, frame of the hinge structure and leaflet opening angle.

1.3 Research goal and outline of the report

The work of this thesis is part of an extended research which is aimed at reproducing the behaviour of a patient-specific heart valve. This thesis presents itself as an introductory study which deals with the numerical analysis of the behaviour of the aortic valve modelled as a rigid body. The research objective is only oriented on the fluid dynamics of the model since the analysis of the structure is not considered. Thus, the opening and closing motion of the leaflet is taken from experimental values and it is prescribed *a priori* in the simulations. The final goal of this project is to study the influence of this approach on the resulting blood patterns in the aortic root. In particular, the main investigation tries to understand whether this method is able to yield comparable results with respect to both experimental measurements and fluid-structure interaction simulations. The strategy to achieve this purpose consists of two major analyses. First, a two-dimensional case is tested in order to create a benchmark for this method. Successively, a more realistic three-dimensional case has been considered.

The outline of the thesis will be here introduced in order to guide the reader through the work of this project. The remainder of the report will be organised in different chapters.
In Chapter 2, a review of the current available literature will be presented. First, the state of the art for both experimental and computational works will be discussed. Then, the method adopted for the current investigation will be explained and justified.
In Chapter 3, the two-dimensional simulation of the aortic valve modelled as a rigid body is shown. This test will be used in order to create a benchmark for the approach chosen. The results will be compared to experimental values based on the research of Dumont *et al.* [11] and Stijnen *et al.* [12]. In addition, the comparison between the present method and two-way FSI analysis performed in the same research group will be reported.
In Chapter 4, the approach is extended to three-dimensional simulations. In this case, a commercially available mechanical valve is simulated to reproduce the experimental work of Cerroni [13]. Additionally, further references for this case can be retrieved in the paper of De Tullio *et al.* [14].
In Chapter 5, conclusions will be drawn and suggestions for future work will be included.

2

Literature Review

Studies of the aortic valve already date back to the 15th century thanks to Leonardo da Vinci. He can be considered the pioneer in this field for his early investigations. In fact, collections of sketches and drawings which were realised upon direct observation of dissected hearts can be found in one of his works. Actually, he did not only focus on the anatomical description and the geometrical dimensions of the various components of the aortic valve but also on its role and functioning. As his annotations evince, he tried to understand the opening and closing mechanism of the valve and its behaviour as the fluid flows through it. In addition, he also brought innovative discoveries. He was the first one to ever propose a rudimentary design of an artificial valve and he was able to predict, through some simple experiments, associated phenomena which were also observed in the last century [15].
A great breakthrough in the study of the aortic valve could be achieved in the last 40 years as a consequence of the development of modern investigating techniques. The contributions aimed to deepen our understanding of the aortic valve have been acquired through either experimental methods or numerical simulations in the last decades. In particular, three main categories can be distinguished. In the first one, the work was focussed on the structural dynamics of the aortic valve using models derived from casts and moulds or by *in vivo* experiments through radiopaque markers or sonomicrometric crystals. The second group is mainly focussed on the kinematic point of view. Particle Image Velocimetry (PIV) or 3D Magnetic Resonance Imaging (MRI) phase contrast methods were used in experimental works to visualise flow behaviour and vorticity fields. Finally, an other approach represents the computational analysis achieved through the fluid-structure interaction technique in which mutual interactions between solid deformations and the fluid flow are coupled together. Overall, the purpose of this chapter is to present the state of the art of the research on this topic on each of the aforementioned aspects.

2.1 Dynamics of the normal aortic valve

Number of devices and surgical techniques are employed for the treatment of CVDs. Few examples include the use of stents to cure stenoses or artificial heart transplant. In the recent years, new techniques have been developed to solve some valvular diseases which consist of modifying directly the valve rather than substituting it with mechanical prostheses. For this reason, a precise description of the geometry of the aortic valve together with a trustworthy knowledge of its working principle are of paramount importance for flow calculations or prior to the design of prosthetic heart valves. This has brought many researchers to investigate accurately the details of the functioning of the aortic valve.
The work carried out by Thubrikar is remarkable and his research can be considered a milestone for this field [6, 16, 21]. He performed an insightful investigation of the behaviour of the aortic valve through *in vivo* experimental measurements on dogs. More in details, the position and the movement of radiopaque markers were monitored through x-ray analysis. By exploiting this technique, attention is drawn on the dynamic response of the aortic valve. Two main factors were found to influence the dynamics of the aortic valve; precisely these are both pressure in the left ventricle and in the aorta section. During the cardiac cycle, an average change of 12% of the commissural perimeter was recorded and a quantitative relation was derived with respect to the aortic pressure (Fig. 2.1.a) [16]. Furthermore, changes in the aortic root base were also observed. The base perimeter reaches its maximum value during the opening phase triggering an outward pull on the leaflets; on the other hand, a reduction in size takes place during the closing phase. This shrinkage displaces the leaflets inwards so that the distance the leaflets have to travel is reduced and a complete closure is guaranteed. Overall, the increase of the base perimeter was found to be between 5% and 28% (Fig. 2.1.b) [6].

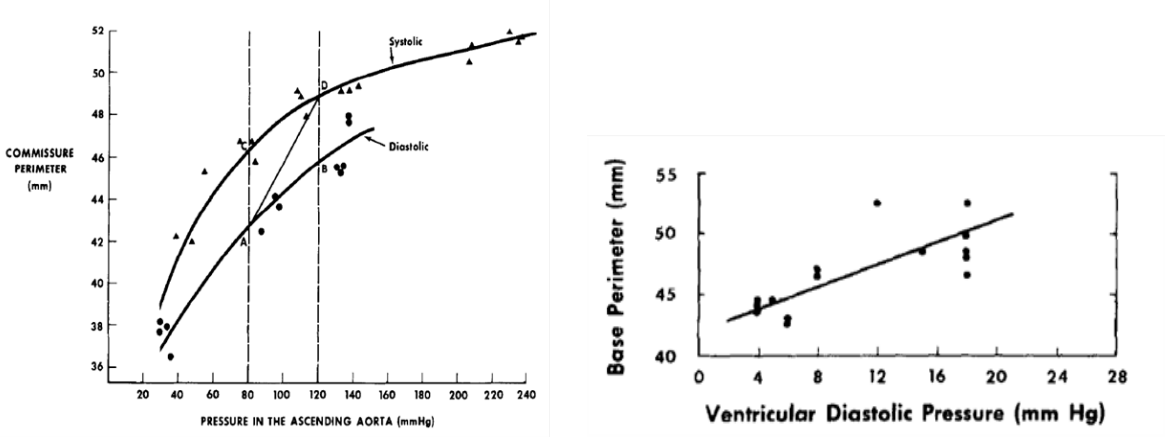

Figure 2.1: In (*a*), variation of the commissure perimeter as function of aortic pressure [6]. In (*b*), variation of the base perimeter as function of ventricular pressure [16].

Other more recent experimental works have been conducted by Dagum [17] and Lansac [18].

In both cases, experimental measurements were carried out on ovine aortic valves although two different techniques were employed. Geometrical dimensions and variations of the parameters of the aortic root were accurately measured on each interval of the heart cycle to characterise the dynamic behaviour of the valve. Dagum *et al.* [17] performed a four-mode deformation analysis focussing on the stresses in different directions, including the longitudinal, shear, torsional and circumferential components. In addition, expansion and shrinkage of the aortic perimeter at the base and at the level of the commissures were reported not to be uniform but varying according to the side of the leaflet [17]. Similarly, Lansac *et al.* [18] found a repetitive pattern regarding the changes of the aortic root within the cardiac cycle. The results were obtained by an open-chest investigation realised with micro ultrasonic crystals. The aortic root undergoes an expansion of about 11.3% [18]. This phenomenon was found to occur before ejection, allowing the structure to settle on a pronounced truncated cone shape. In contrast, a more cylindrical shape was attained during systole because of the expansions that are mainly induced in the commissural region. Changes of this part in the first third of systole were found to be of 32% [18].
Another technique which has been involved in order to examine *in vivo* the aortic valve is called echocardiography. This technique is based on the emission of ultrasounds at high frequencies from a transducer held in contact with the skin. As the beam of sound waves travels through the tissue, it will be eventually reflected at the interfaces between blood and cardiac muscles. The time it takes for the signal to bounce back is employed to determine the distance of the reflecting surface. An image of this reflecting surface can be generated at that depth and it can be displayed on a screen for direct assessment. Since echocardiography is noninvasive and it does not produce any side effects, this method could extend the study of the aortic valve dynamics directly on human beings. Early researches date back to 1970s where Gramiak *et al.* [19] measured an increase in the sinus diameter of about 4% during systole, comparable to what had been found on animals. However, the bidimensional analysis is a limitation since only two of three leaflets are visible. Moreover, the valve opening cannot be often exactly recorded during the systolic phase because of its fast movements. Recently, improvements could be attained with the introduction of 3D echocardiography. Handke *et al.* [20] proved the potentiality of this approach by quantitative evaluations of the main characteristics of the aortic valve. Orifice area and shape, opening or closing velocities and time could be fully determined from the processing of the images derived from this method.

2.2 Geometrical description of the normal aortic valve

Experimental studies have highlighted the great adaptability of the aortic valve to change with pressure during the cycle. This is thought to be an advantageous mechanism because it naturally minimises energy losses and stresses and, at the same time, it maximises flow ejection [17,18,21]. On the other hand, the introductory discussion in the previous paragraph also aimed to highlight the complexity of the topic. This intricate problem suggests that a mathematical representation of neither the equations of motion nor constitutive equations can be easily derived. For this reason, biomechanical engineers have tried to overcome this issue by focussing on an alternative simplified representation of this structure. Hence, a reference model based on some design parameters which could entirely characterise the aortic valve geometry was developed. To achieve this, some simplifying assumptions are necessarily required in order to make the problem more approachable. First of all, the three leaflets are

considered to be equal in size and in shape. So, they lie at 120° from each other. Actually, this is not entirely true as measurements on moulds and casts have shown that the right coronary leaflet is slightly bigger than the other two [22]. Another significant consideration is that the planes passing through the base of the valve and through the top of the commissures are parallel. Similar to the previous case, real measurements have shown that the two planes are inclined with an average angle of 5.47° [22]. Nevertheless, this is considered to be quite small and have little influence on the results. Finally, the dimensional changes during the heart cycle are not considered. The foregoing assumptions were common traits that could be recognised in every study involving aortic valve modelling.

The work of Swanson and Clark [23] is one of the first attempts to derive a design of the human aortic valve based on geometrical characteristics. They performed measurements on a series of silicone rubber casts created by varying the intra-aortic pressure from 0 to 120 mmHg in human hearts. Their optimal design was developed using average values at 100 mmHg. All the values were nondimensionalised with respect to the inflow diameter because its variations with pressure were found to be negligible. Swanson and Clark's contribution also clarified that the surface of the leaflet is derived from a section of a cylindrical surface both in open and closed positions. In addition, based on stress considerations, it was also observed that the attachment line of the leaflet has got an elliptical shape as it results from the intersection of a plane and the cylindrical inflow tract. A mathematical representation of this surface was also provided.

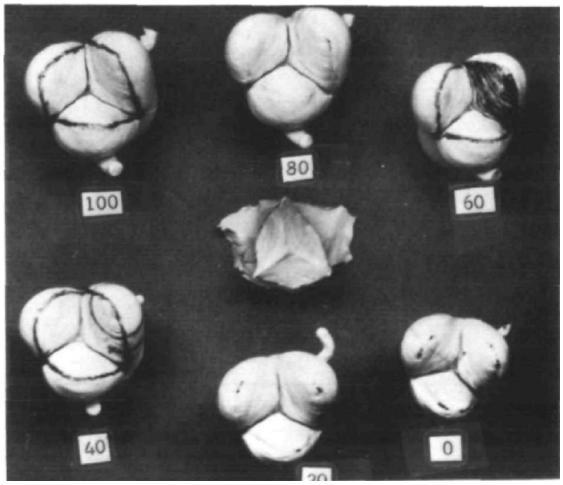

Figure 2.2: Example of rubber casts [23].

In the same manner, Thubrikar also emphasizes the search for the optimal parameters for the design of the normal aortic valve [21]. Based on an attentive monitoring during several cardiac cycles, five parameters were identified to fully describe the aortic valve. These are:

1. the angle ϕ that the free edge forms with the plane passing through the commissures;
2. the angle α that the leaflets forms with respect to the plane at the base;
3. the radius of the base, R_b;

4. the radius of the commissures, R_c;
5. the vertical height, H.

The optimal parameters were chosen at middiastole, i.e. the middle of the interval where the valve is in its closed configuration. A configuration of these parameters within the structure can be found in Figure 2.3.a.

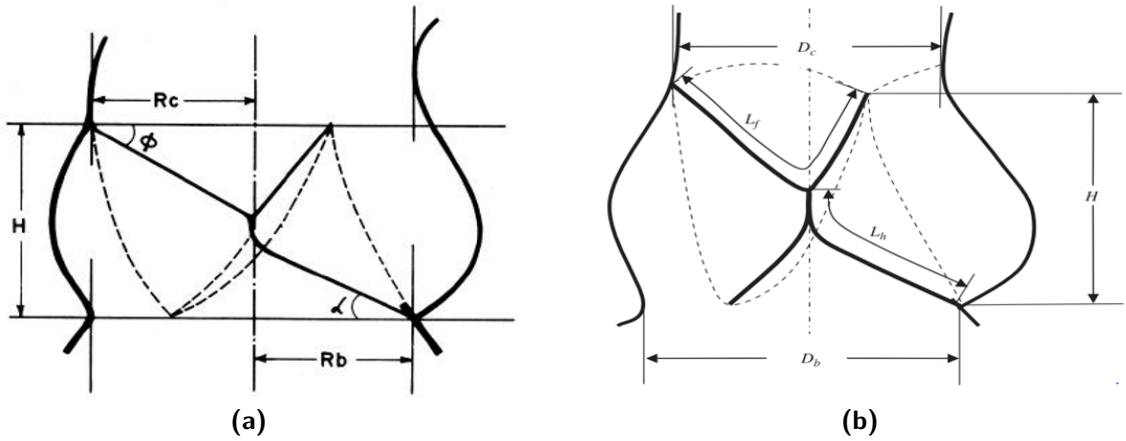

Figure 2.3: Schematic of the aortic root highlighting the design parameters used to characterise the modelling according to Thubrikar [21] in *(a)* and Labrosse [24] in *(b)*.

The relevance of choosing the design parameters in an accurate manner has been stressed since variations from the optimal design is typical of malformed heart valves. As a matter of fact, the study demonstrated that these values cannot be chosen empirically because they are intercorrelated the one with the other. So, changing one parameter will lead to change in others resulting in incompetent or diseased valve representations. Examples of how negatively this can affect the results are as follows. For instance, having a large angle ϕ causes the free edge to fold in open configuration so to increase stresses that may damage the structure. On the contrary, if the angle α is too small then the valve will not entirely open. Consequently, the leaflets will obstruct the flow producing a reduced efficiency for the valve and a work overload for the heart.
A similar investigation can be also retrieved in the work carried out by Labrosse [24] where a combination of experimental methods and analytical procedures were combined to formulate a set of equations to represent the aortic valve. The starting point consists of a set of primary design parameters which could be directly measured on rubber moulds. For this case, these parameters are slightly different from those used by Thubrikar [21], as it can be seen in Figure 2.3.b. Besides the top and bottom radii and the aortic valve height, the leaflet free edge length, L_f, and the leaflet height, L_h, have been preferred to the angles α and ϕ. Two extra assumptions are further taken into account. The first one follows the observations of Swanson and Clark claiming that the load-bearing surface of the leaflet tends to settle into a cylindrical shape [23]. The second one states that the open and closed configurations are mirrored with respect to the plane which contains the attachment line of the leaflets. A

schematic representation of one leaflet drawn following these two principles is shown in Figure 2.4.

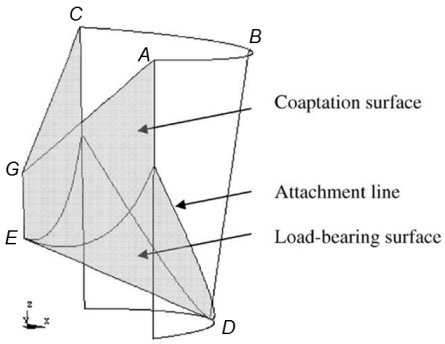

Figure 2.4: Representation of one leaflet in both closed (shaded) and open (transparent) positions [24].

These geometric design criteria were transformed into a set of non linear equations which can be solved numerically. The primary design elements together with additional secondary components were used as input to feed these equations and to solve out the model depending on the status of the leaflets. For sake of completeness, details and derivation of these formulae are shown in Appendix A.

In conclusion, either measured or calculated values for the design by these three researchers are summarised in Table 2.1. Thubrikar's outcome is represented in the form of ratio in order to minimise the error in the measurements. If these coefficients are compared to the measured results of Swanson and Clarks, the mean values of the parameters are in good agreement [23].

Table 2.1: Comparisons of the dimensions of the design parameters of the aortic valve.

Authors	Type of valve	α [deg]	H [mm]	ϕ [deg]	R_b [mm]	R_c [mm]	L_f [mm]	L_h [mm]
Swanson & Clark [23]	Human	22	14.2	34	10	$R_c \approx R_b$	–	–
Thubrikar [21]	Canine	20 ± 1	$1.4R_b$	34 ± 0.9	10	$1.2R_b$	–	–
Labrosse [24]	Human	19	16.8	10	13	12	30	17

At the starting point of the project, this current was being followed in order to tackle the problem. However, this approach was later believed to be somewhat cumbersome for the purpose of the research goal. The main reason is that the discussed procedures are only able to describe the work in either fully open or fully closed configurations whereas intermediate positions could not be resolved mathematically. As a consequence, they could not be represented from the geometrical point of view. All things considered, this approach was not deeply developed and another strategy had to be chosen.

2.3 Fluid dynamics of the aortic valve

To provide a complete picture on the aortic root, studies which dealt with the fluid dynamics of the blood through the orifice will be presented. Analytical derivations are accompanied by validating experimental investigations. The combination of these two methods contributed to yield a more precise description of the behaviour of the fluid. In this paragraph, two different models will be briefly presented.

To begin with, Bellhouse *et al.* [25] developed a model of the aortic valve made of rigid Perspex glass except for the leaflets. On the contrary, these were 0.1 mm thick and they were realised with a nylon net coated with silicone rubber. The overall dimensions for the model were chosen as to represent those of an adult man. The set up was tested in a water tunnel where the inflow could be adapted to recreate steady and pulsatile conditions. In addition, the flow was rendered visible thanks to dye injection.
First, a steady state analysis was conducted. In this case, the leaflets were positioned in their fully open configuration. It could be observed that a vortex formed in each sinus region although the core was shifted close to the ridge. From the theoretical point of view, the entrapped vortex was modelled as one half of a Hill spherical vortex. Pressure measurements showed that pressures on both sides of the cusp matched so no significant variations in the radial direction were recorded.
Transient analysis allowed to measure aortic velocity and leaflet position as functions of time, as shown in Figure 2.5.

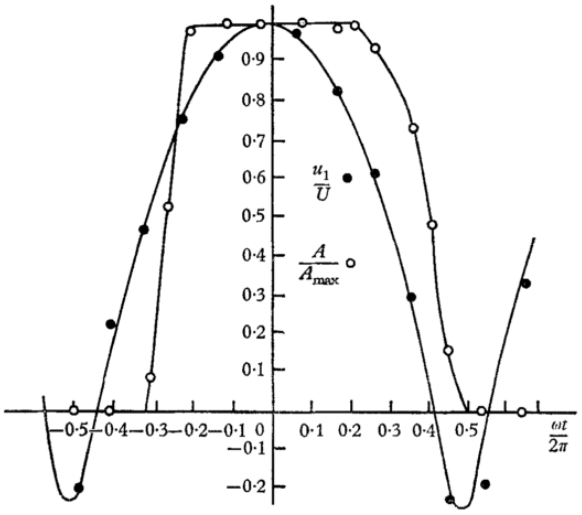

Figure 2.5: Aortic velocity (black dots) and valve opening area (white dots) as functions of time from experimental measurements [25].

The data collection was realised through a heated element gauge connected to an oscilloscope and a ciné camera. Four major phases within one cycle could be distinguished from direct observation of successive frames. These are:

1. the *opening phase* which takes 15% of the systolic time. The leaflets rapidly reach the fully open condition;

2. the *quasi-steady phase* which occupies about 55% of the systolic pulse. In this case, the leaflets remain in their fully open state;

3. the *aortic deceleration phase* which lasts 30% of the systolic pulse. The onset of the flow deceleration causes the pressure of the aortic side of the leaflet to be smaller than that on the sinus side. This pressure difference generates a force which drives the valve towards the closed position. When the forward flow stops, the valve is almost closed;

4. the *reversed flow phase* represents the final phase where backflow aids the complete sealing of the cusps.

A theoretical model based on the solution of the unsteady inviscid equation was employed in order to provide a mathematical expression for the pressure difference which drives the closure mechanism of the leaflet after peak systole. The combination of conservation of mass and the momentum equation yields the final expression which is formulated as

$$\Delta P = 0.08\rho u_1^2 - \left(2a - \frac{1}{2}L\right)\rho\frac{du_1}{dt} \tag{2.1}$$

where u_1 is the upstream velocity, a is the radius of the channel and L the length of the leaflet. The pressure difference ΔP computed according to this procedure was compared to measurement values. The values were found to be in the range of 1-2 mmHg [25]. Although this derivation produces valid results only for small time values after the peak, it provided a preliminary understanding of the valve closure mechanism.

Another fluid dynamic model was presented by Steenhoven *et al.* [26]. Their research was aimed to understand the relation between flow deceleration and the closure mechanism of the valve. In particular, Steenhoven *et al.* reported that the model of Bellhouse *et al.* overestimates the pressure difference across the leaflets computed during the deceleration of the flow [26]. In fact, their theory is based on the assumption that cusps cannot withstand any pressure difference because of their negligible mass. The experiments were conducted in a two-dimensional setup, as sketched in Figure 2.6. The model was composed of half of a cylinder on top of a rectangular channel to represent respectively the sinus cavity and the aorta. The leaflet was realised with a foil with a thickness of $2\,\mu m$. Water was used as test fluid and the flow was visualised through the hydrogen bubble technique. The flow is characterised by two dimensionless numbers: Reynolds number (Re) and Strouhal number (St). The former is defined as Uh_0/ν, where U represents the main maximum velocity upstream, h_0 is the channel height and ν is the kinematic viscosity. The range of Re was between 2250 and 4500 so comparable to realistic values of the human system. On the other hand, the latter is defined as $R/U\tau$ where R is the sinus radius and τ is the time the flow takes to decelerate from U to zero. Typical value for humans is 0.06 whereas in this model St was allowed to vary between ∞ and 0.045 by imposing either a stepwise or more gradual velocity decrease [26]. The experiments were performed at different deceleration rates and it could be concluded that flow patterns and leaflet behaviour were highly dependent on the Strouhal number. In this matter, only the case for low Strouhal numbers ($St < 0.15$) will be considered as it is more appropriate to describe the human situation. From the initial steady state position, the leaflet remains straight and rotates around its point of attachment into the aorta. The profile

of the main flow remains flat downstream so no strong pressure gradients are established. A theoretical model was developed to explain the phenomena observed from experiments.

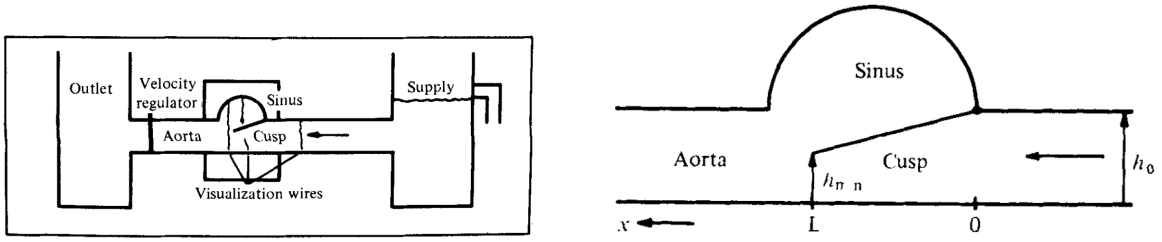

Figure 2.6: In *(a)*, representation of the bidimensional experimental setup. In *(b)*, sketch of the geometrical domain for the theoretical model. Both pictures are from [26].

To simplify the model, the flow is considered to be quasi one dimensional so that the main quantities are dependent only on space and time. An additional dimensionless parameter is introduced and it is defined as $\lambda = h/h_0$, where h_0 is the height of the rectangular duct and h is the distance from the bottom of the channel to the tip of the cusp. The leaflet spans a horizontal length L; the height of the fluid underneath the cusp is variable and it can be expressed as a function of space, namely $h(x) = h_0 \left[1 - (1 - \lambda)x/L\right]$. The derivations for this model lead to a second order differential equation in λ of the form

$$\frac{d^2\lambda}{dt^2} + \frac{16}{3}\frac{u_0}{L}\frac{d\lambda}{dt} - (1-\lambda)\left[4\frac{u_0^2}{L^2} + \frac{8}{3}\frac{1}{L}\frac{du_0}{dt}\right] = 4\frac{1}{L}\frac{du_0}{dt} \tag{2.2}$$

with initial conditions $d\lambda/dt = 0$, $\lambda = 1$ at $t = 0$. Equation 2.2 describes the leaflet motion as a function of time for small values of $1 - \lambda$. It was solved numerically and theoretical predictions were found to have fair agreement with experimental measurements [26].

2.4 Fluid-structure interaction models

Fluid-structure interaction (FSI) of the aortic valve has been treated quite extensively in the last decade. This has led to the development of different techniques which are able to tackle the problem in various ways. To begin with, it must be mentioned that the interaction between the solid and fluid interfaces for aortic valve problems becomes complicated due to the large motion of a thin structure within the computational fluid domain. In addition, the governing equations of the fluid are better described with respect to the Eulerian reference system whereas the Lagrangian approach is more suitable for the solid counterpart. To cope with this incompatibility, boundary conforming methods have been proposed. The most common method for this category is known as the Arbitrary Lagrange-Euler (ALE) formulation. According to this approach, the mesh is allowed to deform dynamically in time in order to adapt to the boundaries of the computational domain. However, the disadvantage is that this

method has to be restricted to simple geometries if a good quality mesh is to be preserved. In combination with the ALE formulation, a remeshing technique can be exploited for improvements but the resulting computational time increases and artificial diffusivity is introduced in the model.
To eliminate the need of a grid which adjusts with the movement of the boundaries, non-boundary conforming procedures have been developed. In this case, the fluid domain is discretised according to the Eulerian formulation and it remains unaltered during the whole computation. On the other hand, the solid moving domain is discretised by a set of pointwise constraints which are coupled with the equations of motions using the Lagrangian method. Several techniques which fall within this group are available. Nonetheless, two of them have been largely proposed in the literature. Namely, they are the Immersed Boundary (IB) and the Fictitious Domain methods. The IB was already computationally investigated by Peskin back in 1970s and introduced in his early works on heart valves [27]. This method consists on using a number of control points along the interface. Forces known *a priori* are applied to these points and then distributed to the neighbouring nodes through first-order accurate methods. His work was limited to the study of Reynolds number far below the actual physiological values because of numerical instabilities arisen from the misalignment of the boundary layers and the grid lines on immersed surfaces [28]. Therefore, improvements of this methodology were lately found out for example by the exploitation of ghost cells, i.e. cells belonging to the solid domain which have at least one neighbouring element in the fluid part. Other contributions to renew this method in this field was given by Fadlun *et al.* [29] and Cristallo & Verzicco [30]. This last work was applied by De Tullio *et al.* [14, 31] in combination with Direct Numerical Simulation (DNS) in order to solve turbulent flows through mechanical bileaflet heart valve at higher Reynolds numbers.
Equally important, the fictitious domain method is strictly related to the previous one. On top of the fluid domain, a solid mesh is allowed to freely move without modifying the former. The main difference is that in this situation the two domains are coupled at the interface through Lagrange multipliers. Generally, the constraint imposed is related to the kinematics since the velocities on both domains are set to be equal. The advantage of this technique is that the classical formulations for the two domains can be maintained. This new approach was first introduced by Glowinski *et al.* [32] and it was later adopted by De Hart [33, 34]. First of all, he was able to apply this method to the simulation of a two-dimensional model for the normal aortic valve [33]. Later, he also continued this work on a three-dimensional trileaflet aortic valve, extending the analysis to a stented case besides the normal one [34]. The main disadvantage of this method consists in the high computational cost as a result of large grids required to simulate the flow at physiological Re.
To overcome this issue, sharp-interface immersed boundary methods have been proposed. Within this category, the curvilinear immersed boundary methods (CURVIB) combines structured curvilinear boundary fitted grids with the sharp-interface of IB method [35]. This methodology has been applied to simulate pulsatile flows through bileaflet mechanical aortic valve [36,37]. In conclusion, another typical characteristic of FSI models regards the coupling of the two domains. The interactions between the fluid and structural regions are accounted for through the boundary conditions at the interface. The coupling can be either loose or strong. The first means that the structural domain is updated once at each time step using the forces obtained by the fluid domain in the previous time step. On the other hand the strong coupling makes sure that both domains reach convergence before passing through the next time step. For this reason, this last approach is considered to be more robust and stable.

2.5 Discussion

Although three-dimensional FSI simulations allow to acquire important aspects derived from the coupling of the structure with the flow, they can become expensive from the computational point of view. For this reason, a simplifying analysis method is proposed. In this study, the kinematics of the leaflet is not derived by means of coupled FSI simulations but rather its opening and closing motion is prescribed in advance based on available experimental values. In the literature, only few studies which follow the procedure chosen for the present work have been reported [38–40]. Ge *et al.* [38] prescribed the kinematics of the leaflets for a mechanical bileaflet aortic valve although the housing was not considered. Dasi *et al.* [39] combined experimental PIV measurements with DNS numerical simulations to visualise vorticity structures of a similar aortic valve. However, the valve was implemented in a simplified axisymmetric model for the aorta and the discretisation method was based on the CURVIB model developed by Ge and Sotiropoulos [39].
In the current research, the simulations were computed through the commercial software ANSYS Fluent using dynamic mesh. First, a two-dimensional case was investigated in order to check the reliability of the software; successively, this *modus operandi* was extended and applied to the three-dimensional case. The results of the simulations were validated with experimental measurements in order to demonstrate the numerical reproducibility of the flow features and the influence of this method on the resulting hemodynamics.

2.5.1 Dynamic mesh and governing equation

The dynamic mesh model of ANSYS Fluent is enabled in order to handle moving objects or boundaries in the domain. The model can deal with both rigid body motions and deformations. Because the shape of the domain changes with time, an additional convective term which contains the velocity of the mesh is introduced in the governing equation. For a given scalar function ϕ on an arbitrary control volume V with moving boundaries ∂V, the integral form of the conservation equation can be formulated as

$$\frac{d}{dt}\int_V \rho\phi\, dV + \int_{\partial V} \rho\phi(\vec{u}-\vec{u}_b)\cdot\hat{n}\, dS = \int_{\partial V} \Gamma\nabla\phi\cdot\hat{n}\, dS + \int_V S_\phi\, dV \tag{2.3}$$

where ρ is the density of the fluid, $\vec{u}$ is the velocity vector, $\vec{u}_b$ is the velocity of the moving boundaries, Γ is a diffusion coefficient and S_ϕ is a source term of ϕ.
A geometric conservation law (GCL) is introduced in order to ensure that a uniform flow on the moving mesh is preserved. This formulation guarantees that numerical errors do not arise because of the additional convective term in the transport equation [41]. The integral formulation of the GCL is given by

$$\frac{d}{dt}\int_V dV = \int_{\partial V} \vec{u}_b\cdot\hat{n}\, dS,$$

meaning that the rate of change of the control volume is equal to the volume swept by the moving boundary. The GCL is solved numerically. First, a spatial discretisation is applied for a control volume V with a number of faces equal to N, yielding

$$\frac{d}{dt}\int_V dV = \sum_{j=1}^{N}(\vec{u}_b \cdot \hat{n}\, dS)_j.$$

The dot product for each face j of V is evaluated according to the time integration scheme selected in Fluent (§ Appendix C). For a first-order backward difference formula, the expression is calculated from

$$(\vec{u}_b \cdot \hat{n})_j = \frac{\delta V_j}{\Delta t}$$

where δV_j is the volume swept by the boundary of j over the time step Δt. Instead, for a second-order upwind backward difference scheme, the dot product is evaluated as

$$(\vec{u}_b \cdot \hat{n})_j^{n+1} = \frac{3}{2}\left(\frac{\delta V_j}{\Delta t}\right)^n - \frac{1}{2}\left(\frac{\delta V_j}{\Delta t}\right)^{n-1}$$

where δV_j^n and δV_j^{n-1} are the volumes swept by the boundary of j at the current and previous time levels over a time step Δt.

The adjustment of the mesh is automatically accounted for by the software. In particular, there are different methods which are used in order to update the volume mesh. These are:

- smoothing methods;
- dynamic layering;
- local remeshing techniques.

Each model is selected according to the motion of the zones and to the composition of the mesh. Further details will be presented in Appendix B.

3

2D analysis and validation

This chapter deals with the two-dimensional simulation of the aortic valve. The leaflet is modelled as a rigid body and its kinematics is prescribed *a priori*. This test will be used in order to benchmark the current approach so that this methodology can be extended in 3D. The results will be compared and validated with experimental values and two-way FSI simulations.

3.1 Introduction and experimental method

In order to investigate the applicability of our approach to analyse the blood patterns in the aortic root, computational predictions are validated with *in vitro* experiments based on the experimental setup similar to the one used by De Hart [33]. However, the experimental measurements performed by Stijnen [12] and Dumont [11] have been preferred for this purpose because a stiff model for the leaflet was used. A schematic representation of the setup is shown in Figure 3.1.

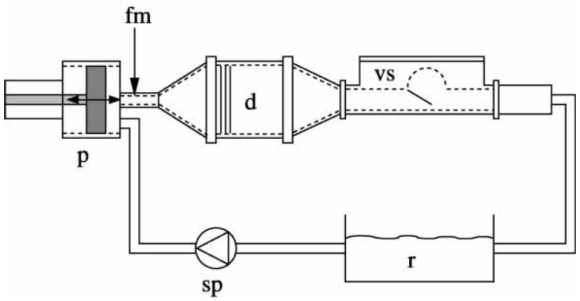

Figure 3.1: Schematic representation of the experimental setup: piston (p), diffuser (p), valve section (vs), reservoir (r), stationary pump (sp) and flow meter (fm) [11].

It is composed of a steady pump (sp), a computer controlled piston (p), a diffusor (d) and the valve section (vs). The last compartment corresponds to the measurement section of the setup. It is a plexiglass channel which contains a stiff strip of lexane in order to represent the leaflet. The strip is attached to the rest of the structure using three pieces of water resistant tape of which two are fixed at the side walls and one in the centre. A magnified picture of this compartment is shown in Figure 3.2 whereas a more detailed description can be found in the next paragraph.

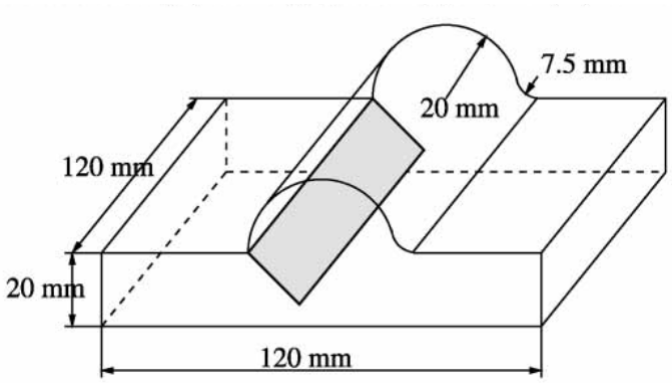

Figure 3.2: Particular of the valve section of the experimental setup [11].

The test fluid was a mixture of glycerol in water in order to resemble viscosity and density of blood. The velocity field was analysed using the Particle Image Velocimetry (PIV) technique. A CCD camera (Kodak ES-1.0) was employed to record images of the leaflet and fluid field [12]. The opening angle of the valve could be directly derived from these images.
Stijnen *et al.* uses this experimental work to validate a FSI study using a fictitious domain method [12]. Dumont *et al.* exploits the commercial software Fluent to perform simulations [11]. The dynamic mesh model employed for the fluid domain was coupled with a user-defined iterative code in order to recreate FSI analysis. Results were compared with experimental measurements for validation. However, up to date, a pure computational analysis using a commercial software where the motion of the body is prescribed in advance is missing. The scope of this chapter is to present the implementation of this method in order to fill this gap.

3.2 Geometry and mesh of the computational model

The geometry of the computational model mimics the compartment in the experimental set-up which represents the two-dimensional longitudinal cross section of the aortic valve. The geometry contains an inflow tract, an outflow part and a cylindrical structure. They are meant to represent an analogy with the components of the aortic root. Therefore, the inlet, the outlet and the circular section stand for respectively the left ventricle, the aorta tract and the sinus of Valsalva. The dimensions were chosen as to be as close as possible to the actual dimensions of the setup. The height of the channel h is 20 mm and the radius R of the half cylindrical part is equal to h. The conjunction between the downstream side of the cavity and the outflow channel is realised through a fillet radius r equal to 7.5 mm.

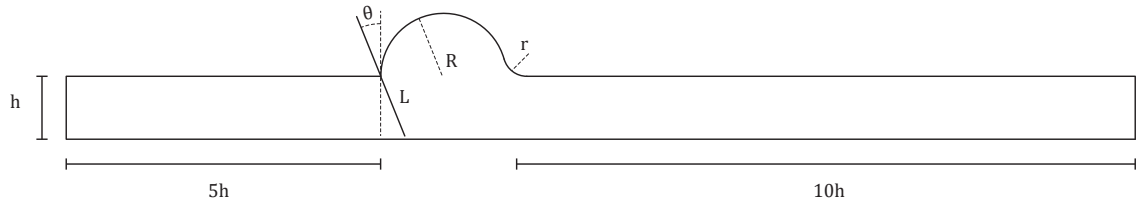

Figure 3.3: Sketch of the geometrical model for the 2D case.

At the initial position, the leaflet forms an angle θ of 22° with the vertical. The length of the leaflet L has been chosen in order to have a gap between the cusp tip and the bottom wall of 1/20 of the overall height of the channel. This gap is necessary because the fluid domain cannot be discontinuous since the mass conservation equation needs to be satisfied at all instants. Thus, perfect closeness will never be achieved. The entrance length is five times the characteristic height and it has been computed according to $L_{\mathrm{e,lam}} = 0.06\mathrm{Re}D_h$, where Re is the Reynolds number and D_h is the equivalent diameter since the cross section is not circular. Finally, the outflow tract is ten times the height of the channel. These parameters are summarised in Table 3.1 and in Figure 3.3.

Table 3.1: Geometrical properties of the valve model.

h [mm]	R [mm]	θ [deg]	L [mm]	r [mm]
20	20	22	20.5	7.5

The fluid domain has been discretised using triangular elements. The grid was generated by using the meshing software ICEM CFD. The mesh contains approximately 48900 cells and 24300 nodes of which the minimum element size measures 0.0575 mm. Local refinements have been applied to particular regions of the domain. Since the leaflet is subject to fast movements, strong gradients are likely to be created. Thus, a local refinement has been applied in the area close to the leaflet in order to be able to resolve accurately the flow. For the same reason, the gap that is present when the valve is in closed position was also refined. The quality of the mesh has been tested by the evaluation of some criteria such as skewness and aspect ratio. To check whether the results were mesh independent, a mesh validation analysis has been also performed. This study has been reported in Appendix D. In conclusion, the main features of the mesh are summarised in Table 3.2 whereas the computational mesh is shown in Figure 3.4 of which a magnified view is shown in Figure 3.5.

Table 3.2: Summary of the parameters of the two-dimensional mesh.

Elements	Nodes	Min size [mm]	Max size [mm]	Min skew	Min quality	Max aspect ratio
48.9k	24.3k	0.0575	0.9	0.76	0.88	3.24

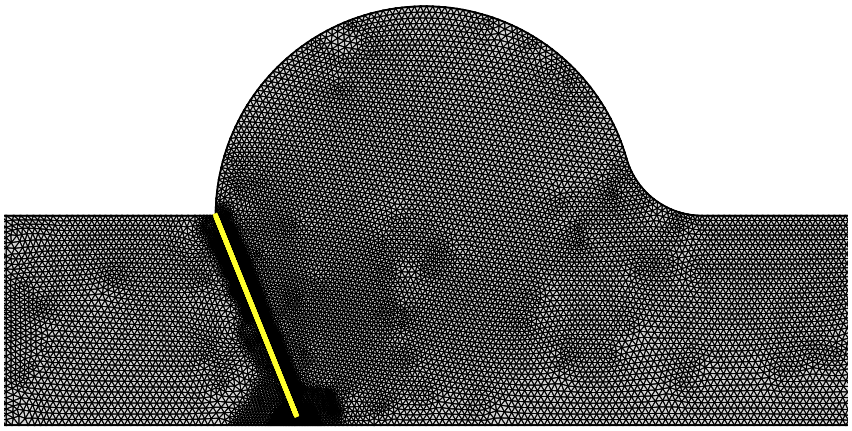

Figure 3.4: Overview of the two-dimensional mesh. The leaflet is highlighted in yellow.

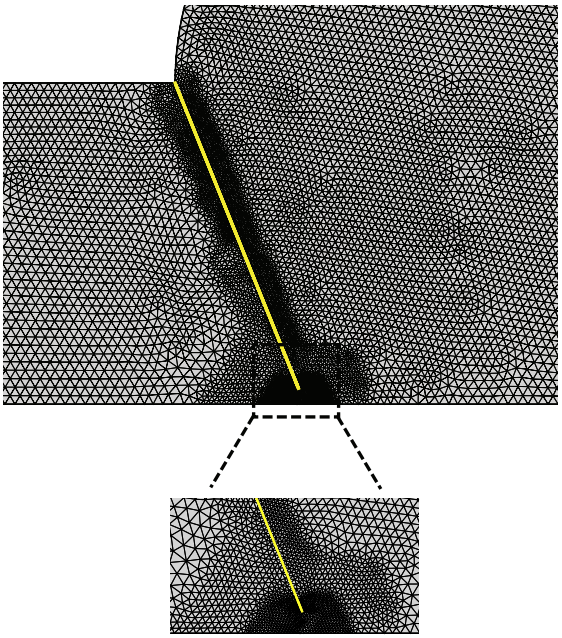

Figure 3.5: Magnified region of the two-dimensional grid.

3.3 Boundary conditions

The velocity inlet is a pulsatile flow which has been derived from the experimental flow data. It was obtained by the superimposition of a steady flow governed by a pump with a pulsating flow generated by the periodical motion of the computer controlled piston [11]. The flow pulse was measured by an electromagnetic probe and an analytical fitting is applied to the signal (Fig. 3.6).

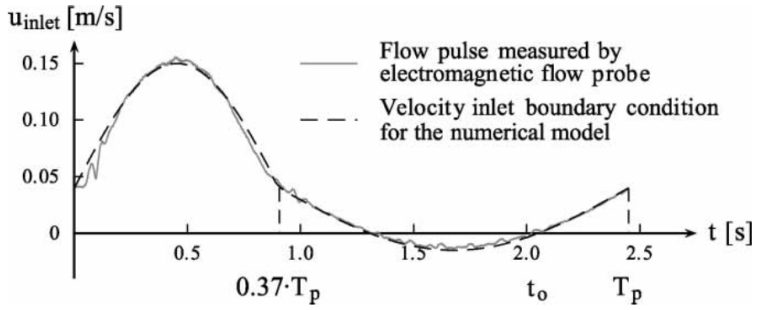

Figure 3.6: Flow pulse from experimental measurements with analytical fitting [11].

The flow pulse component in the x-direction can be described mathematically as a function of time by the following equations as described in [11]. A temporal shift of t^* has been applied so to have an accelerating flow at the initial time $t_0 = 0\,s$. The inlet formula is represented by

$$U(t) = \begin{cases} u_{\text{mean}} + \frac{1}{2} u_{\text{amp}} \sin\left(\frac{2\pi(t-t^*)/\tau + 0.26}{1.26}\right), & \text{if } 0 < t < t^* \text{ and } t^* + 0.37\tau < t < \tau, \\ u_{\text{mean}} + u_{\text{amp}} \sin\left(\frac{2\pi(t-t^*)}{0.74\tau}\right), & \text{if } t^* < t < 0.37\tau. \end{cases}$$

The parameter u_{mean} and u_{amp} represent respectively the mean velocity and the amplitude velocity during the period τ. Their specific values are given in Table 3.3.

Table 3.3: Parameters for the inlet velocity formulation.

u_{mean} [m/s]	u_{amp} [m/s]	u_{max} [m/s]	τ [s]	t^* [s]
0.04	0.11	0.15	2.45	0.4

The flow pulse has been shaped such that it resembles the realistic aortic pulsatile flow. In fact, the peak is reached after 37% of the overall period. This instant coincides with the maximum systolic ejection. The flow pulse can be observed in Figure 3.7. The equations were implemented in a user-defined function (UDF) in Fluent whose code can be found in Appendix F.

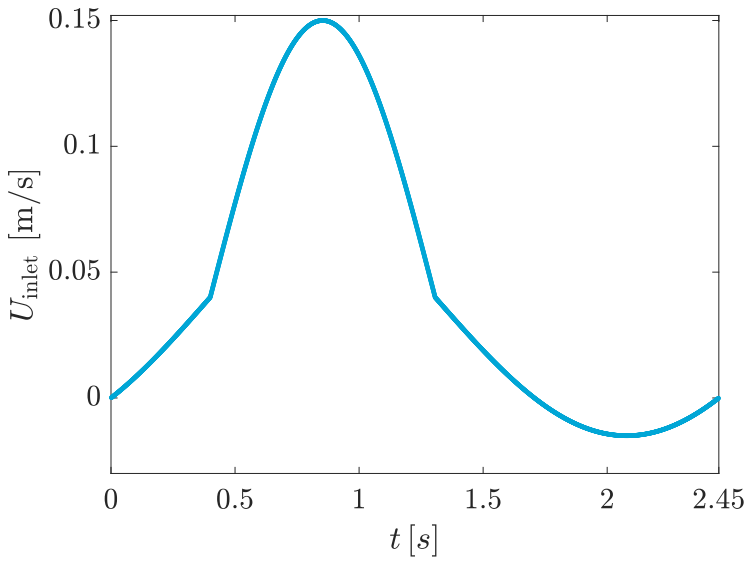

Figure 3.7: Inlet velocity profile U as function of time. Only one cycle is shown.

The maximum inlet velocity $u_{\max}$, the density ρ of 1090 kg/m^3 and the dynamic viscosity μ of 0.004 kg m^{-1}s^{-1} are used to determine the characteristics of the flow. In particular, the dimensionless numbers used are:

$$\text{Re} = \frac{\rho u_{\max} h}{\mu} = 750, \tag{3.1}$$

$$\text{St} = \frac{h}{\tau u_{\max}} = 0.055. \tag{3.2}$$

Although the former considerably differs from the realistic physiological value range, the latter is quite realistic. In fact, experiments with Strouhal number in this range were also carried out by Steenhoven *et al.* (§ Section 2.3) [26].
At the outlet, a constant gauge pressure of 0 Pa has been specified whereas the other boundaries are considered as walls, to which the no-slip condition is applied.

3.4 Valve motion and dynamic mesh

The motion of the valve has been derived from the experimental work starting from the opening angle of the leaflet. The experimental data have been interpolated by using piecewise cubic Hermite polynomials in Matlab. This method was primarily chosen because it guarantees that the interpolating functions have continuous first and second derivatives. The opening angle of the leaflet as a function of time is described in Figure 3.8.
The angular velocity of the leaflet has been derived from the opening angle, knowing that $\Omega = d\theta/dt$. The computation of the first derivative has been evaluated using an adaptation of a Matlab code called `splinetx.m` [42]. The resulting angular velocity as function

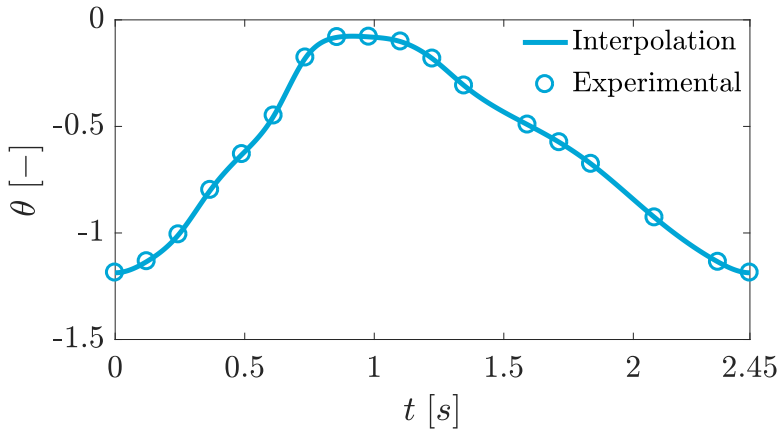

Figure 3.8: Leaflet opening angle as a function of time. Circular markers represent experimental data whereas the solid line shows the interpolated values.

of time is shown in Figure 3.9. For each time interval, the coefficients of a second-degree polynomial have been obtained so that the opening and closing mechanism can be described mathematically.

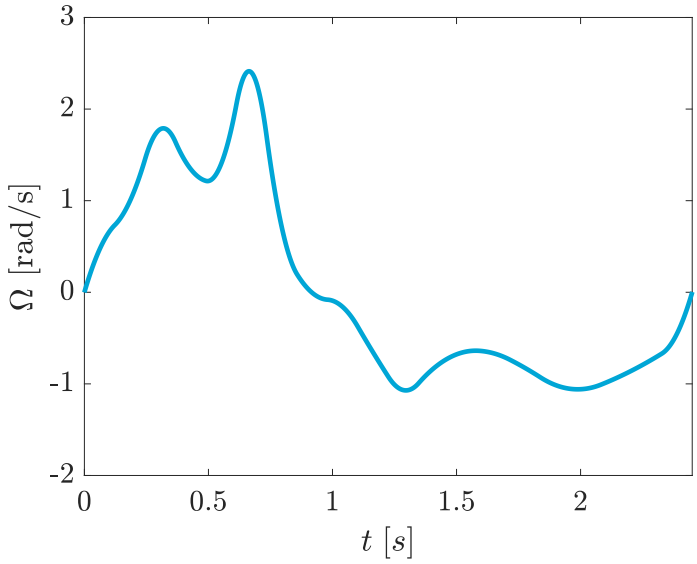

Figure 3.9: Angular velocity of the leaflet as function of time.

Since the motion of the valve is prescribed in advance in this approach, it is input in the simulations using a UDF. The implementation was realised by the `DEFINE_CG_MOTION` macro because it provides the angular velocity of the particular dynamic zone to the solver for each time step (§ Appendix B). Then, Fluent automatically updates the position of the nodes based on a rigid body motion expressed by the following law

$$\theta^{n+1} = \theta^n + \Omega \Delta t.$$

The script was structured such that the position of the leaflet can be integrated accurately by the solver according to the Simpson's scheme. In this manner, it is guaranteed that the movement of the leaflet is the same for each cycle. Therefore, the angular velocity is computed according to

$$\Omega^* = \frac{1}{6}\left[\Omega(t_n) + 4\Omega\left(t_n + \frac{\Delta t}{2}\right) + \Omega\left(t_n + \Delta t\right)\right].$$

Dynamic mesh is enabled in order to account for the rotation of the leaflet during the simulation. Two different methods have been selected in order to guarantee a proper quality and density mesh, namely smoothing and remeshing. Each technique is characterised by a set of parameters which are presented in Table 3.4. On the other hand, more detailed theoretical explanations can be found in Appendix B.

Table 3.4: Settings of the parameters for the dynamic mesh methods.

Smoothing		Remeshing	
Options	Setting	Options	Setting
Spring Constant Factor	0.8	Minimum Length Scale	0.13 mm
Convergence Tolerance	0.001	Maximum Length Scale	2.158 mm
Number of Iterations	20	Maximum Cell Skewness	0.4
Elements	Tri	Size Remeshing Interval	1

3.5 Simulation methods

The flow is analysed in transient mode with the laminar model. The settings that have been selected for the simulation in Fluent are listed in Table 3.5. Methods and discretisation schemes are treated in more details in Appendix C. To aid convergence, the under relaxation factor for momentum has been decreased from its default value to 0.5. The residuals for momentum equation were set to 10^{-5} whereas the residual for continuity was set to 10^{-4}. The time step used is $\Delta t = 1\,\text{ms}$ and the simulation is run for 15 cycles.

Table 3.5: Settings for the two-dimensional simulation.

Options	Settings
Solver Type	Pressure-based
Pressure-velocity Coupling	SIMPLE scheme
Gradient	Green-Gauss Node Based
Pressure	Standard
Momentum	Second Order Upwind
Transient Formulation	Second Order Implicit

3.6 Results and validation

In the post-processing, the velocity field has been investigated. Figure 3.10 shows the velocity vectors at five different instants of time superimposed by streamlines coloured according to the velocity magnitude. Moreover, the computational results are shown in comparison with the PIV measurements carried out by Stijnen *et al.* [12].
In the first place, the analysed instants of the flow cycle correspond to five specific moments of the inlet flow pulse. These are at:

1. $t/\tau = 0$, when the flow is at the beginning of the acceleration;
2. $t/\tau = 0.16$, when the flow reaches its average value during acceleration;
3. $t/\tau = 0.35$, when the flow achieves its peak value;
4. $t/\tau = 0.53$, when the flow reaches its mean value during deceleration;
5. $t/\tau = 0.85$, when the flow reaches the end of back flow.

At the beginning of the flow cycle, the valve is in its fully closed position. In this moment, two counter-rotating vortices of different sizes are present in the sinus cavity. Then, the valve starts to open and at the maximum inflow it has already reached its fully open configuration. During this phase, the secondary vortex has disappeared whereas the intensity of the one in the sinus cavity has severely decreased.
The deceleration of the main flow causes the development of a large vortex in the sinus cavity. In this stage, the valve has already started its closing motion although the flow is still directed forward. This is in agreement with the observations of other experimental investigations available in literature. The vortex in the cavity is thought to have an important function because it aids the early closure mechanism of the leaflets [25,26]. Finally, the vortex strength increases as soon as the flow changes direction. In particular, an additional smaller vortex which rotates in the opposite direction appears at the minimum of the back flow. Although only a qualitative comparison can be established between the computational and experimental results, the velocity vectors are considered to be in fair agreement.

Furthermore, the contours for the z-vorticity component are reported for the same five different instants during the flow in Figure 3.11. The vorticity vector field is computed from the curl of the velocity field, $\vec{\omega} = \nabla \times \vec{u}$. Because the analysis is carried out in a plane, the only non-zero component is expressed as

$$\omega_z = \frac{\partial u_y}{\partial x} - \frac{\partial u_x}{\partial y}.$$

The plots confirm the observations on the evolution of the flow derived above. Moreover, they show that the leaflet tip sheds a vortex which is advected downstream in the channel. Other additional vortices are present further downstream in the outflow duct and they tend to decrease in strength when the valve is in the open position because of advection of the mean flow. They are later more visible when the valve closes.

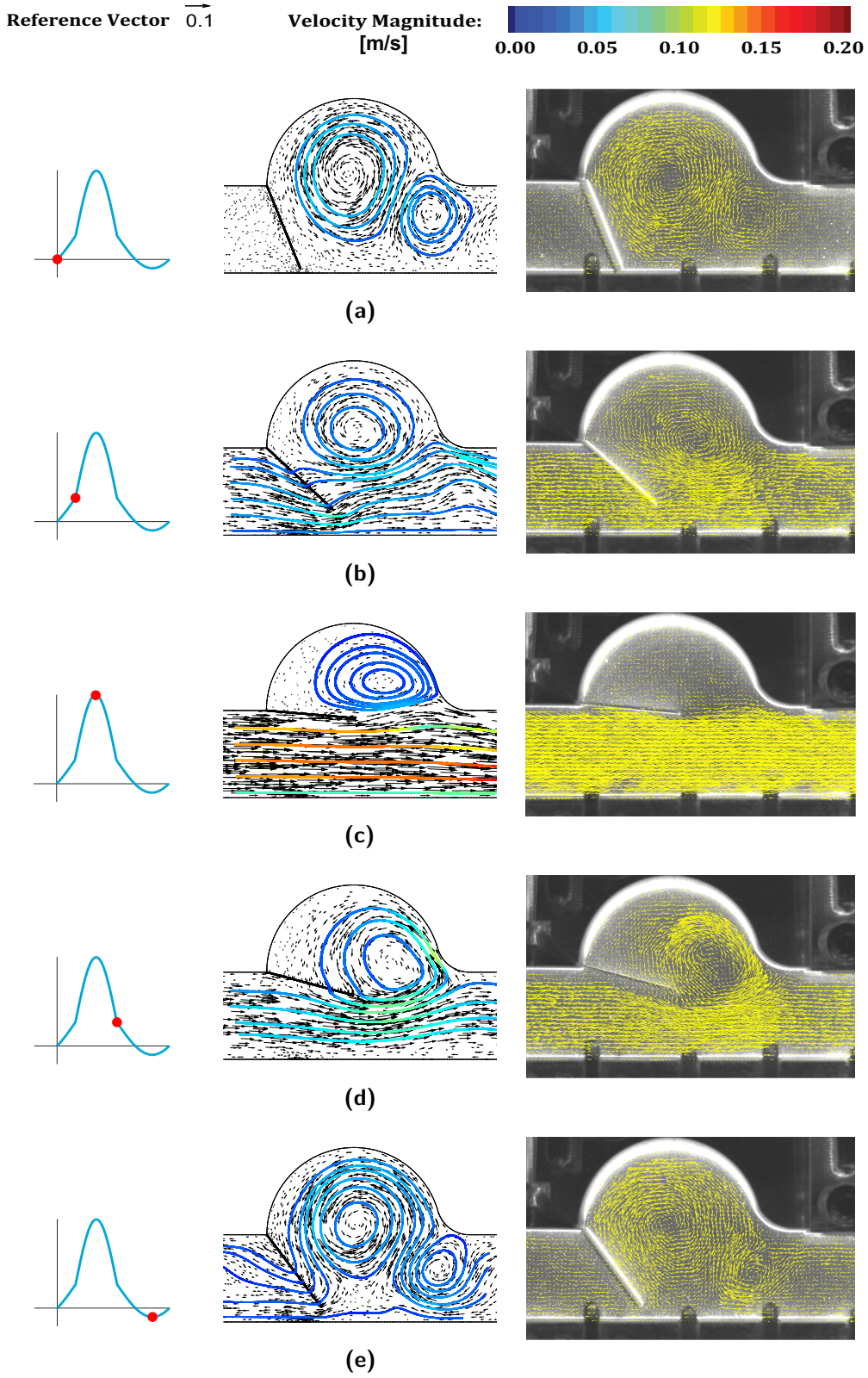

Figure 3.10: Velocity vector plots at five different istants of the flow pulse. The pictures on the right come from PIV measurements [12]. Streamlines are coloured according to velocity magnitude.

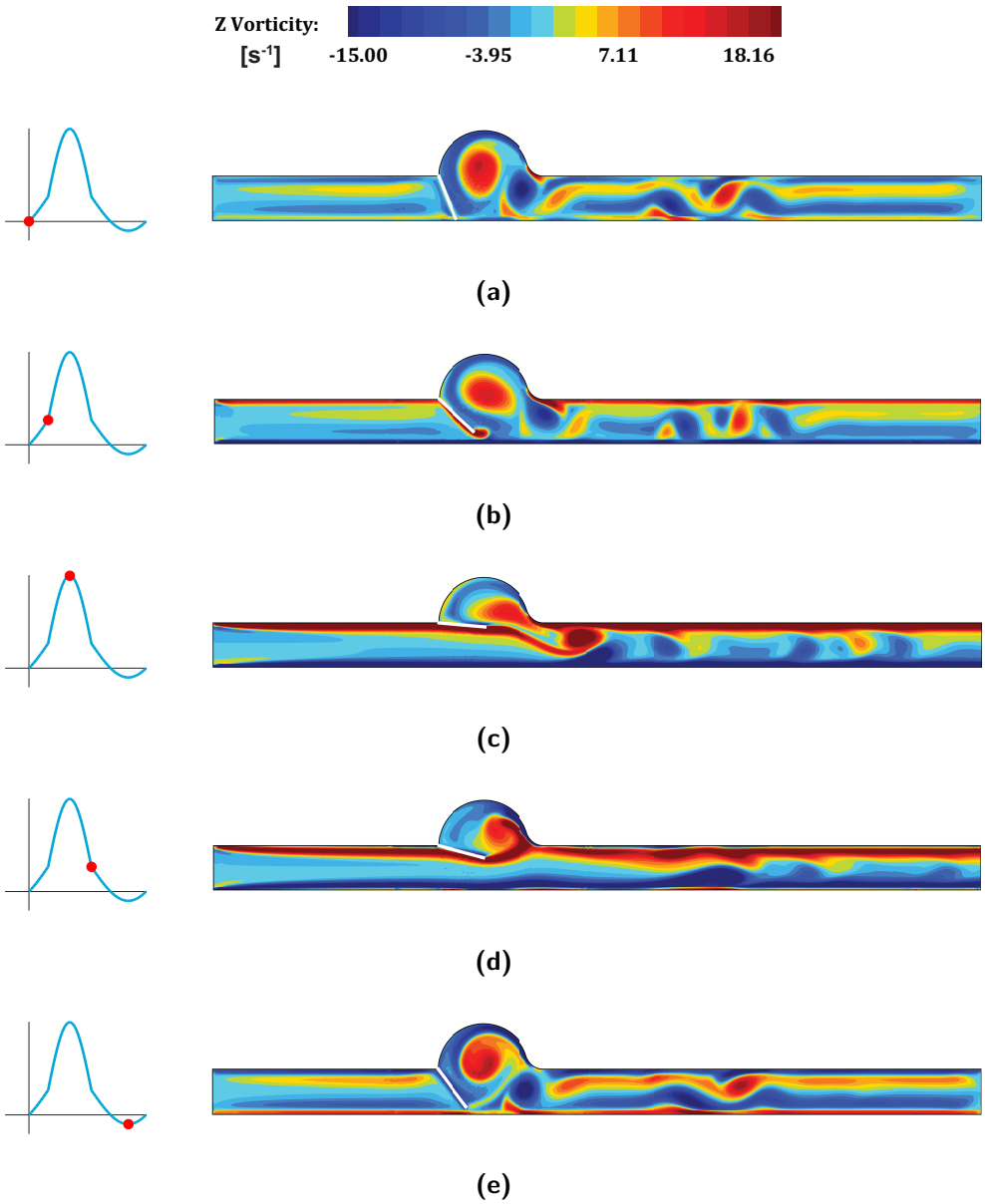

Figure 3.11: Vorticity contours at five different istants of the flow pulse.

The x-component of the velocity has been extracted in three different sections along the channel. Sections A-A, B-B and C-C are placed respectively four, six and eight times the channel height from the inlet. These three locations were chosen so to analyse the behaviour of the flow before the valve, at the centre of the cavity and downstream in the duct.

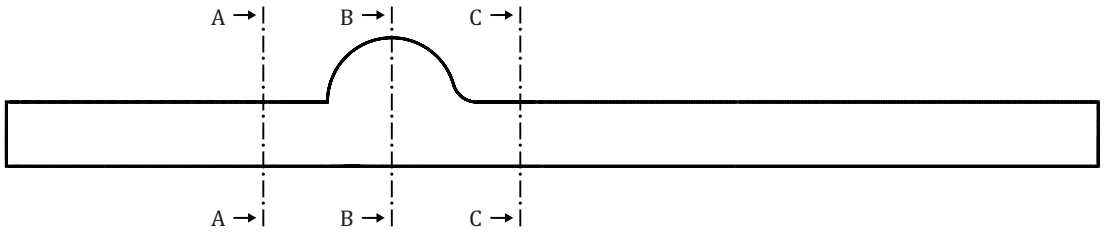

Figure 3.12: Sections along the channel where velocity profiles have been extracted.

Figure 3.13 represents the profiles for the five instants of the flow for the three sections. They have been normalised by the height of the channel along the vertical axis and by the maximum inlet velocity along the horizontal axis. It can be observed that during the forward flow, a plug profile is established in the centre with boundary layers close to the top and bottom walls. In the central section, the presence of the leaflet and the development of the sinus vortex influence the profile in the cavity. When the flow decelerates, reversed flow occurs in the boundary layers in the proximity of the walls highlighting the unsteady nature of the flow.

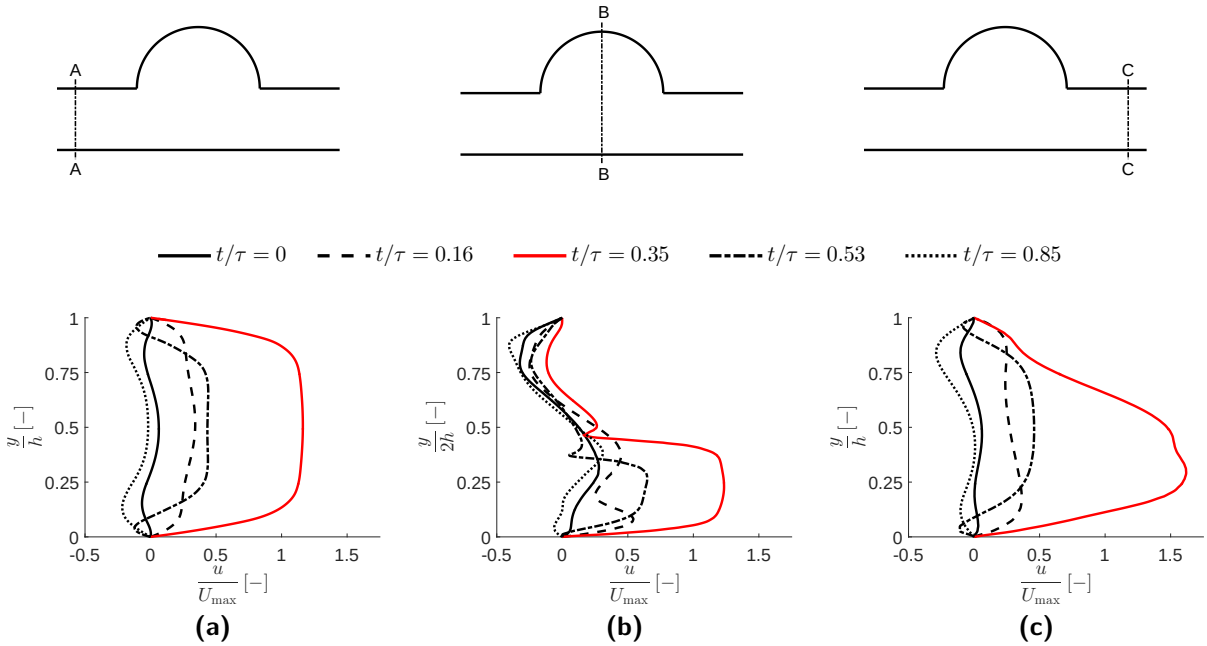

Figure 3.13: Profiles of the x-velocity at the three outlined sections of the channel at five instants of the flow.

To conclude the analysis, time series for pressure and velocity components were also investigated at four different monitor points. One monitoring point was located in the middle of the sinus cavity, two were placed further downstream in the outflow tract separated by a distance h and the last one was manually selected in the gap between the valve in the closed configuration and the bottom wall. The detailed coordinates of the monitoring points are summarised in Table 3.6.

Table 3.6: Coordinate positions of the monitoring points.

Monitoring point	x [mm]	y [mm]
1	120	30
2	160	10
3	180	10
4	100	0.4

A preliminary analysis of the time series reveals a periodic evolution of the signal for all the tracked quantities. An example is reported in Figure 3.14 which shows pressure, x-velocity and y-velocity plotted as function of time for monitor point 1. The first cycle has not been included because it did not produce reliable results due to the initialisation of the simulation.

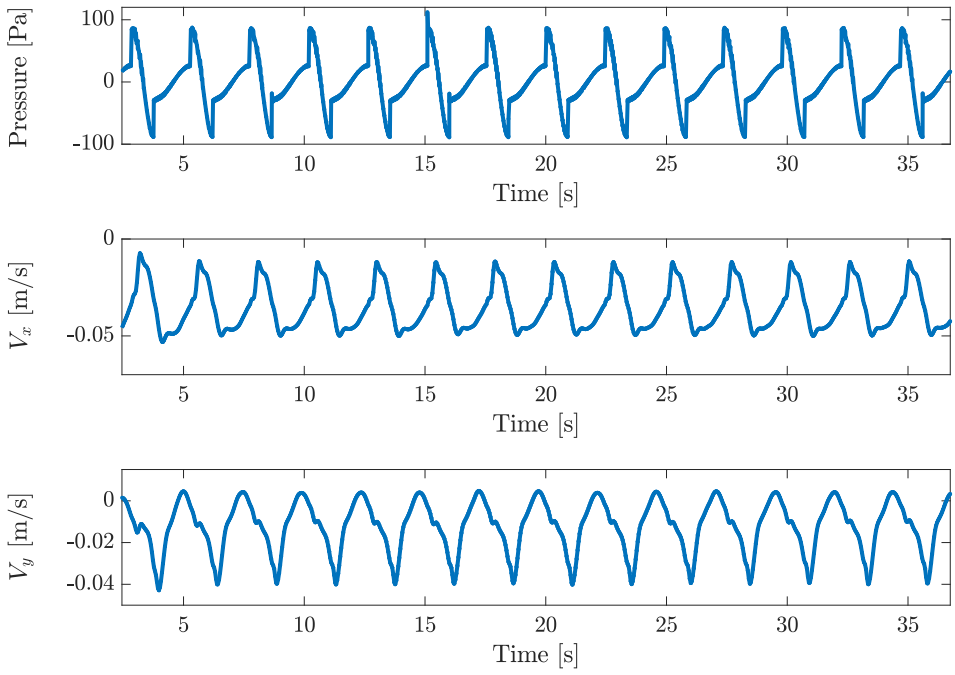

Figure 3.14: Pressure, x-velocity and y-velocity components as function of time for monitor point 1.

Successively, the signals have been studied in the frequency domain in order to gain a complete understanding of the driving frequency of the flow. Hence, a fast Fourier Transform has been applied to the time series. Little differences could be observed for all the corresponding cases of the four monitoring points. For this reason, only the responses for monitor point 2 are shown in Figure 3.15. Power spectra for pressure and for the x-velocity component show a similar behaviour. The signal is governed by the leading frequency $f_0 = 0.4082$ Hz. Remarkably, it is verified that

$$\frac{1}{f_0} = 2.45\ s.$$

The result is coherent with the period derived from the opening and closing of the leaflet. In addition, the spectrum for pressure shows two other minor spikes, respectively at $f_1 = 0.8163$ Hz and $f_2 = 1.224$ Hz. However, these frequencies are found to be harmonics of the basic frequency since they are related to f_0.
The spectrum for the y-velocity component results in a slightly different trend. As it can be seen in Figure 3.15.c, the dominant frequency is still f_0. However, the frequency spectrum is much larger than the previous two. This can be explained by the fact that the flow along the vertical direction is more subject to fluctuations. Therefore, it is more sensitive to instabilities.

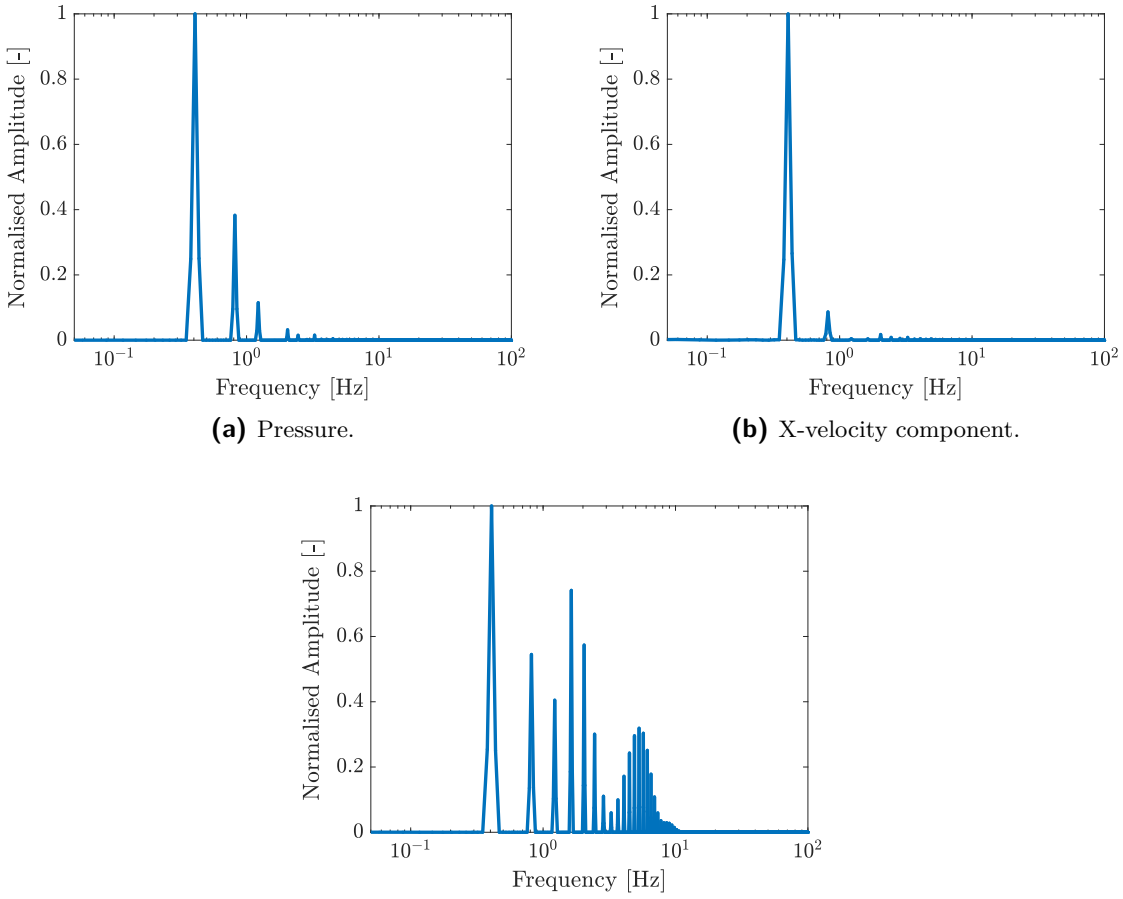

(a) Pressure.

(b) X-velocity component.

(c) Y-velocity component.

Figure 3.15: Spectra for the signals recorded at monitor point 2.

3.7 Comparison with two-way FSI

The current approach has been also compared with two-way FSI simulations performed by Antonini in a parallel study within the same research group [43]. The two numerical methods mimic the experimental setup introduced in section 3.1. However, some modifications were necessary for the FSI geometry. Because the coupling between fluid and structure can only be specified through surfaces in FSI simulations, the two-dimensional domain was extruded in the third dimension. The extrusion thickness was set to 1 mm and symmetry boundary conditions were applied to the lateral borders. The streamwise component of the velocity was selected as the criterion for the comparison between the two numerical approaches. Figure 3.16 shows a quantitative comparison of the profiles extracted in section B-B (see Fig. 3.12). This zone corresponds to the line passing through the centre of the sinus cavity. The plots are depicted for three precise instants of the flow, namely at the beginning of the acceleration when the valve is still closed, at the maximum flow when the valve is in its fully open position and at the maximum reversed flow when the valve has already started the closing phase.

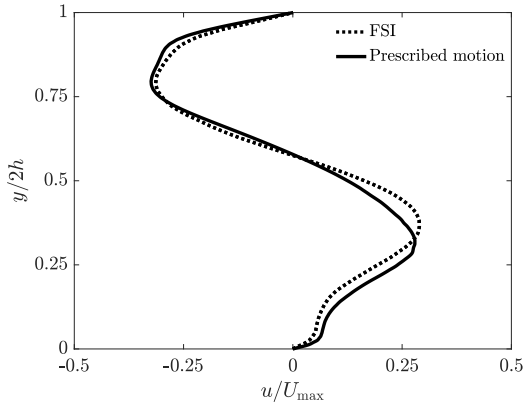

(a) Beginning of flow acceleration.

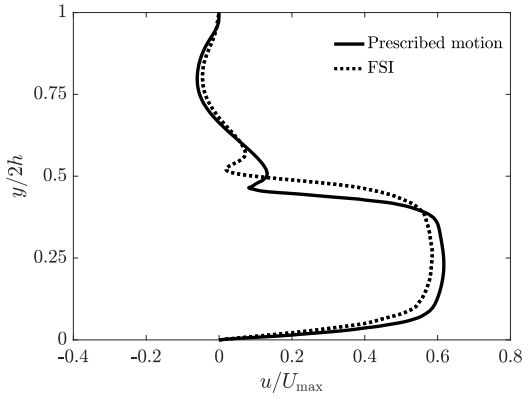

(b) Peak flow.

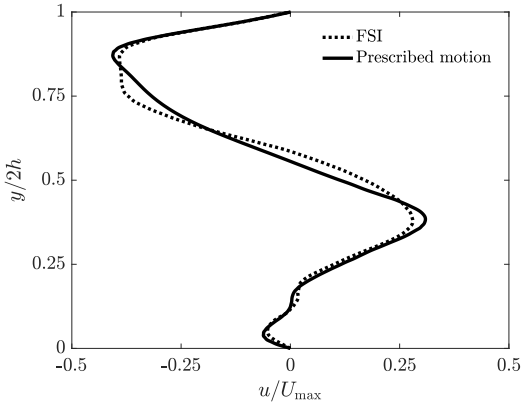

(c) Maximum reversed flow.

Figure 3.16: Quantitative comparison along section B-B of the channel between the FSI (dotted line) and prescribed motion (solid line) approaches.

Besides, a qualitative overview of the normalised velocity profiles for the other sections is given in Figure 3.17. This additional investigation is aimed at providing a more complete analysis on the similarities of the results coming from the two methodologies.

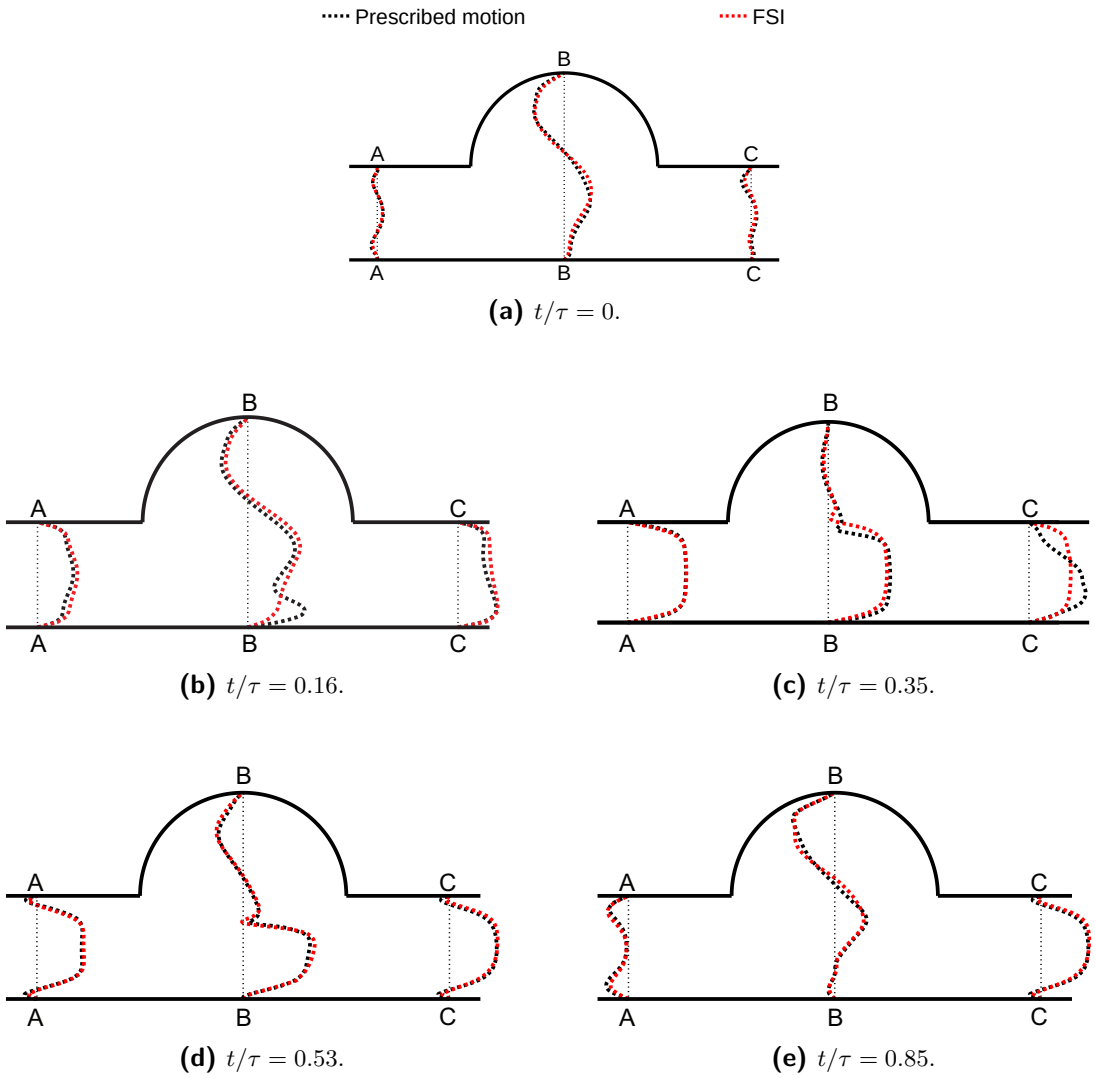

(a) $t/\tau = 0.$ **(b)** $t/\tau = 0.16.$ **(c)** $t/\tau = 0.35.$ **(d)** $t/\tau = 0.53.$ **(e)** $t/\tau = 0.85.$

Figure 3.17: Overview of the comparison of the streamwise velocity profiles resulted from FSI (red dotted line) and prescribed motion (black dotted line) for five different instants of the cycle.

Finally, it can be concluded that the results of the two numerical approaches are in good agreement. Nevertheless, slight differences can still be observed especially for the second and third case of Figure 3.17. A possible explanation of these minor variations lies in the value of the opening angle specified by the two methods. Figure 3.18 reports the position angle of the leaflet as a function of time for the experiments as used in the current model compared with the one computed from FSI simulations of Antonini [43]. Furthermore, the result from the FSI study of Dumont *et al.* [11] is also shown for the validation of the FSI outcome. The

deviation between FSI simulations and experimental measurements is maximum during the acceleration of the flow. The difference can be caused by the side wall effects of the setup which might impede the opening angle of the valve [12]. Since the leaflet reaches a greater opening angle for the FSI simulation, the area available for the flow to pass through is wider for this case than for the prescribed motion situation. Thus, the fluid undergoes stronger accelerations for the current model since it has to flow through a smaller orifice in order to satisfy mass conservation law.

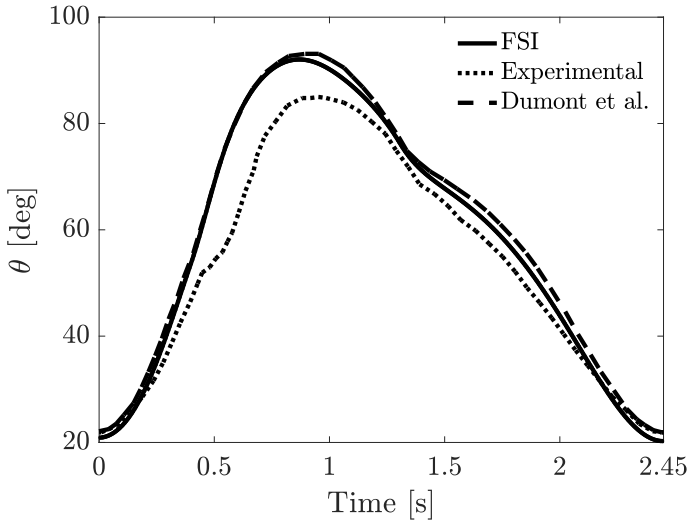

Figure 3.18: Leaflet opening angle as function of time for three different methods.

3.8 Summary

This chapter showed the numerical analysis of a two-dimensional model of the aortic valve by prescribing the motion of the leaflet in advance. In the first place, the experimental measurements from which the valve motion is taken has been presented. Then, the computational model and the settings of the simulations have been described. The resulting hemodynamics in the aortic root is validated qualitatively with experimental results and the two cases have shown to have fair agreement. A large vortex form in the sinus cavity during deceleration of the flow. In addition, a secondary weaker counter-rotating vortex develops just before valve closure. Further investigations on the vorticity contours confirm the observations derived from the analysis of the velocity field. Moreover, a mesh independence test is also performed and the study is shown in Appendix D. The results of the current model were also compared with genuine two-way FSI. The x-velocity components were analysed for different sections along the channel for five instants of the cycle. The two numerical models are found to be in good agreement. Little deviations can be explained by the different kinematics of the valve. In conclusion, the suggested approach is able to reproduce the proposed case to a great extent.

4

3D analysis and validation

The approach tested in the previous chapter is extended to a fully three-dimensional domain. This section deals with the analysis of a physiological flow pulse through a mechanical aortic valve. The kinematics of the leaflet is prescribed in advance as taken from experimental values. The results are validated by a comparison with both experiments and FSI simulations.

4.1 Introduction

The analysis of the three-dimensional case was conducted on a mechanical heart valve. This preference has been chosen in order to be able to work with the following advantages:

- leaflets could be modelled as rigid bodies;
- valve kinematics could be prescribed in advance as taken from experimental values available in literature.

In this manner, the same methodology used in the previous chapter could be maintained and tested on a more realistic case.
On the other hand, the presence of man-made valves influences the physiological flow through these devices. For this reason, prosthetic valves have been largely studied both from the computational and the experimental point of view. In particular, several works in the computational field demonstrated that the flow passing through a mechanical valve is characterised by the arising of complex phenomena. Hence, the need for highly resolved three-dimensional simulations has been highlighted by many authors [8, 38, 44]. The development of such intricate flows can be related to the transition to turbulence especially at the peak of systolic ejection. To deal with this situation, many of the works available in the literature exploit the use of turbulent models. These approaches consist of solving the unsteady Reynolds-Averaged Navier-Stokes (RANS) equations with the aid of additional equations to close the

system. Stevenson was the first one to employ the k-ε model [45]. His work aimed at testing the turbulent effects in a two-dimensional model of trileaflet valves. Successively, Kiris developed his own method to solve the RANS equations based on a finite-volume code and with an algebraic mixing-length turbulence model [46]. Bluestein simulated the unsteady flow through an open bileaflet valve using the k-ω model and compared the results with experimental measurements [47]. Ge performed a three-dimensional analysis of the flow solving the RANS equations using the one-equation Spalart-Almaras model [38]. From the previous considerations, it can be concluded that a unique method which better describes the phenomena of this type of flows has not been identified yet. Generally, all these models allow to perform the simulations with larger integration time steps and with a reduced number of nodes for the grids. Nevertheless, the drawback is that there is a loss of information regarding the dynamics of the flow at the turbulent smallest scales [48]. The alternative method to overcome this issue is to perform DNS. This approach consists of a direct numerical integration of the Navier-Stokes equations. Although this technique allows to resolve all the time and length scales of the flow, it requires very fine mesh and very small time intervals for the simulations. Fewer works have been carried out with this method because of the high computational costs. Dasi investigated the dynamic vorticity of the flow through a bileaflet valve in an axisymmetric domain [39]. De Tullio embedded this method in a FSI code to study the characteristics of the flow patterns by including the motion of the leaflets [14].
Experimental studies complement computational works. Measurements are performed with the purpose of understanding the main features of the flow, especially the velocity field both in the proximity of the device and further downstream. In addition, experimental works serve as a validation tool for simulations. Early studies were conducted under steady flows; later, more realistic pulsatile inlet conditions have been treated. From available literature, the techniques employed are different such as Laser Doppler Velocimetry (LDV) [49, 50] or PIV [51–53]. In all these cases, flow separation and vortex formation have been observed. In this thesis, the experimental work of Cerroni [13, 14] has been reproduced due to the availability of data. These experiments were performed at the University of Rome "La Sapienza" under the context of the SMART-PIV IST-2002-37548 European Project led by Professor Romano [13,14]. The simulations were run both in laminar and in turbulent regimes. Further details on the numerical options will be presented in the next paragraphs.

4.2 Experimental model

The experimental setup consists of an open loop mock circulatory system designed by RWTH Aachen [13]. The different elements which compose the system are mounted in order to have a vertical arrangement. In this manner, the valve can operate under the action of a vertical flow to mimic realistic conditions. The testing fluid is a solution of glycerol and water in order to obtain a density and viscosity similar to that of blood. A schematic representation of the setup is shown in Figure 4.1. The system is equipped by a PC-controlled electric motor which drives a vertical piston. The piston is directly connected to a chamber which hosts a silicon model of the left ventricle. The movement of the piston actively regulates the cyclic contraction and expansion of the ventricle. The ventricle compartment is connected to the aortic root through a mechanical bileaflet valve produced by the Sorin Biomedica group. Further geometrical characteristics of the valve will be presented in the next section. The rest of the circuit is composed of two compliances which are air-filled chambers, a resistance

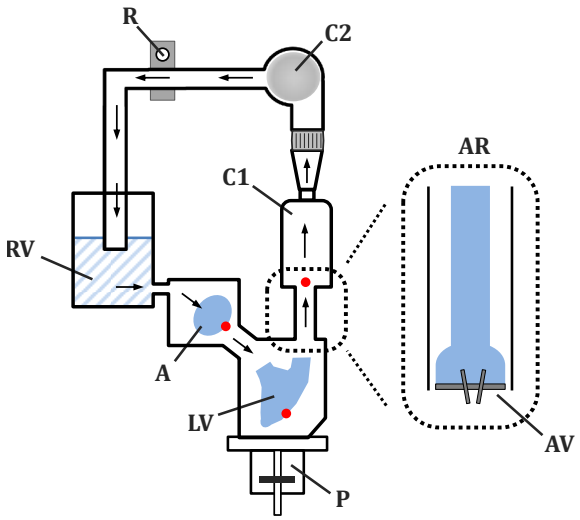

Figure 4.1: Schematic representation of the experimental setup: piston (P), left ventricle (LV), aortic valve (AV), aortic root (AR), first compliance (C1), second compliance (C2), resistance (R), reservoir (RV) and atrium (A). The red dots indicate the position of the pressure sensors.

which accounts for the peripheral circulation of blood throughout the body, a reservoir and the atrium compartment. Three sensors are placed in the circuit for the pressure measurements, namely in the atrium, in the ventricle and at the end of the aortic root. The experimental analysis has been conducted through bidimensional PIV in various planes of the aortic root. The results are extracted using a high-speed camera able to record at 1024 frames per second. Data were acquired using a variable time interval which ranged between 400 and 3000 μs depending on the phase of the cycle.

4.3 Geometry and mesh of the computational domain

The computational model tries to represent the geometry of the experimental setup of Cerroni and Romano [13]. The model is composed of an inflow tract, the housing with the leaflets, the three sinuses of Valsalva and an outflow duct. All the main dimensions are scaled with respect to the inlet channel diameter d which measures 27 mm. The quantities are summarised in the graphical sketch of Figure 4.3 whereas the corresponding relations are listed in Table 4.1.

Table 4.1: Geometrical dimensions of the three-dimensional domain.

Dimension	Relation	Value [mm]
d	–	27
H	$1.14d$	30.78
h	$0.26d$	7.02
D	$1.26d$	34.02
L_{out}	$10d$	270
L_{in}	d	27

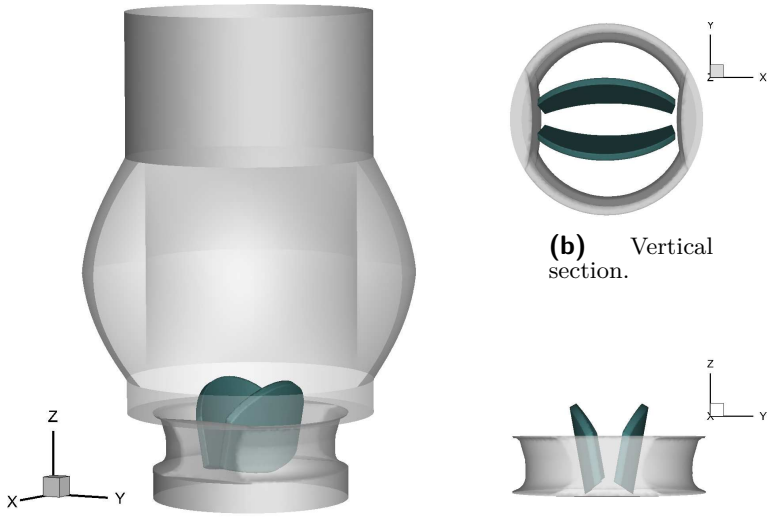

(a) 3D view of AR and AV.

(b) Vertical section.

(c) Horizontal section.

Figure 4.2: Representation of the geometrical domain with detailed views of the mechanical valve in open configuration.

The valve represents the bileaflet Bicarbon Aortic Valve model of the Sorin-Group. The housing and the leaflet geometries have been kindly provided by the research group of Politecnico of Bari for the current analysis. The housing of the valve has got an airfoil profile which decreases in width from the inflow towards the outflow side. The outer diameter measures 27 mm whereas the internal one is variable and its minimum is equal to 23 mm. The two leaflets are symmetric with respect to the valve central plane and they are characterised by a curved profile. In the commercial valve, a microscopic hinge mechanism allows the leaflets to rotate around a pivot for the opening and closing phases. Nevertheless, this feature has not been included in the computational model in order to simplify the overall structure and its kinematics. On the other hand, a small gap is introduced between the two leaflets and between each leaflet tip and the housing. This is done in order to guarantee continuity of the fluid domain required to satisfy mass conservation equation. Further details on the valve motion are discussed in section 4.5.

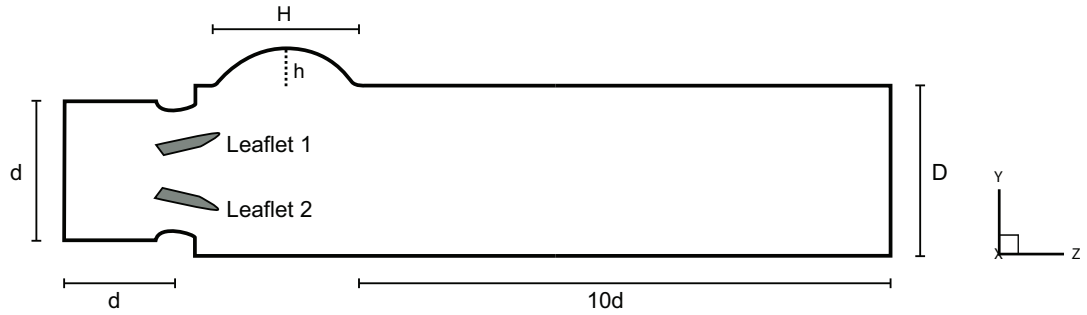

Figure 4.3: Sketch of the model corresponding to the central cross section $x = 0$. The main lengths are also reported in the drawing.

The sinuses of Valsalva are assumed to be symmetric. Thus, they are placed at equal distance the one with the other forming an angle of 120°. Since the valve is mounted in an intra-annular configuration, the housing does not extend into the sinus cavities. Finally, the valve is oriented asymmetrically with respect to the sinuses. This feature can be seen in Figure 4.4.

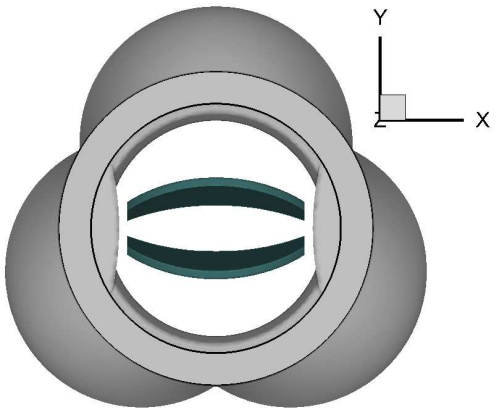

Figure 4.4: Top view of the model shows the asymmetric implementation of the valves with respect to the three sinuses.

In an analogous manner of the two-dimensional case, the mesh has been realised through the ICEM CFD software. The mesh is an unstructured grid realised with tetrahedral elements for the body and triangular elements for the surfaces. Figure 4.5 gives an example of the grid used for the simulations. The total number of elements is approximately equal to 1.2 million whose minimum size is of the order of 10^{-5} metres. Local refinements have been applied in specific regions of the domain. In particular, they have been applied to the gaps the leaflet form with the boundaries and also to the areas in the proximity of the leaflet surfaces in order to capture the phenomena occurring during their fast movements. A mesh sensitivity test has been performed and the outcome has been reported in Appendix D. In conclusion, the main features of the mesh are summerised in Table 4.2.

Table 4.2: Summary of the parameters of the three-dimensional mesh.

Elements	Nodes	Min size [mm]	Max size [mm]	Min skew	Min quality	Max aspect ratio
1.16M	200k	0.0354	3.63	0.69	0.73	14.69

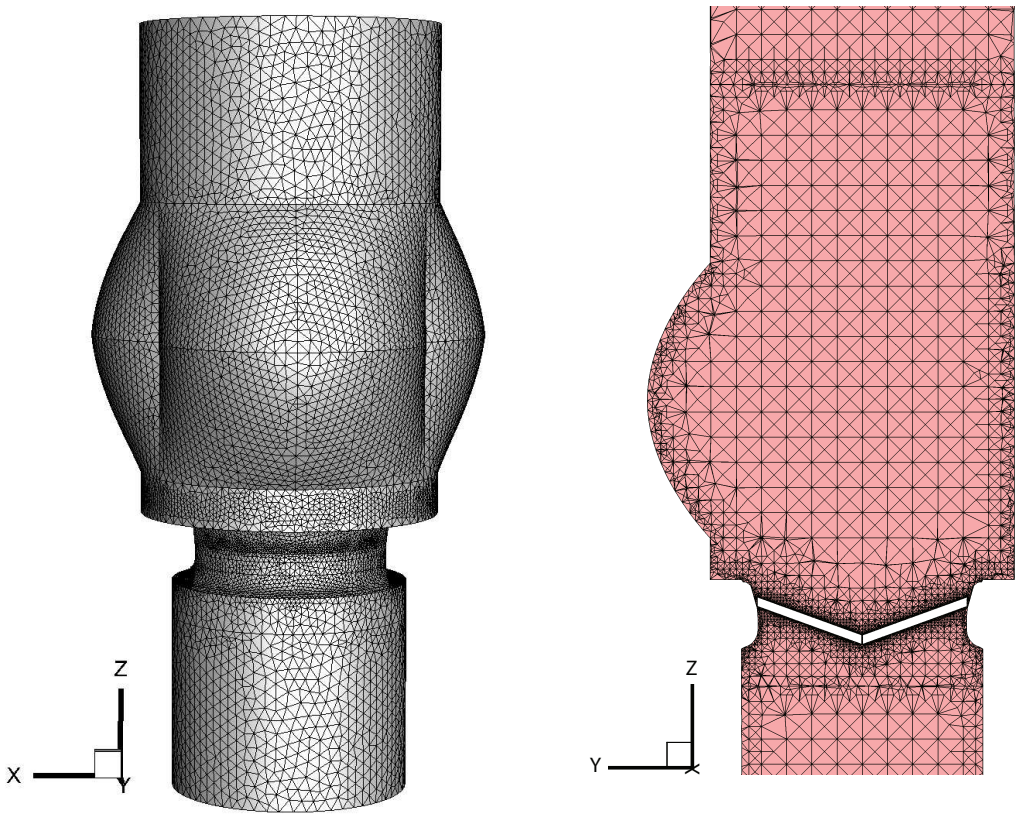

(a) **(b)**

Figure 4.5: In *(a)*, an overview of the surface mesh of the domain. In *(b)*, section of the mesh corresponding to the plane $x = 0$.

4.4 Boundary conditions

The velocity inlet is a uniform pulsatile flow which has been taken from experimental data. The measurements were interpolated using a Fourier series truncated up to the twelfth term and expressed as

$$u(t) = a_0 + \sum_{n=1}^{12} a_n \sin(a_n \omega t) + \sum_{n=1}^{12} \cos(a_n \omega t). \tag{4.1}$$

The fitting has been realised by means of the code `Fseries.m` written by M. Tearle and taken from the Matlab File Exchange [54]. Equation 4.1 has been implemented in a UDF which can be found in Appendix F. The representation of the time evolution of the velocity is shown in Figure 4.6. The overall cycle takes into account both systole and diastole. The flow pulse lasts 866 ms so it approximately corresponds to a heart beat frequency of 70 beats per minute. The average flow rate is equal to 5 l/min whereas the maximum velocity is 0.81 m/s. Small leakage is present for $t > 400$ ms which is typical of mechanical valves as fluid flows through

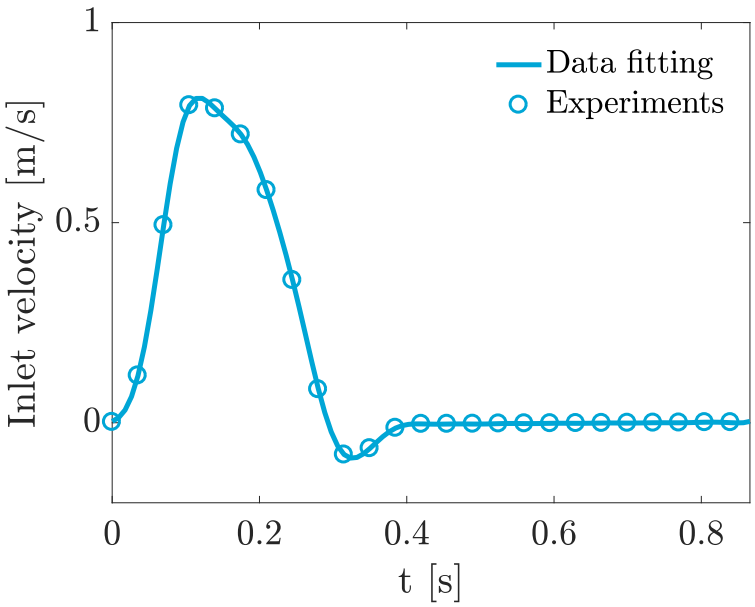

Figure 4.6: Velocity inlet profile as function of time for one cycle.

the gap formed by the hinges [13]. The density of blood ρ is chosen equal to 1060 kg/m^3 and the dynamic viscosity $\mu = 3.2 \times 10^{-3}\,\mathrm{kg\,(ms)}^{-1}$. The dimensionless numbers for this flow are

$$\mathrm{Re} = \frac{\rho u_{\max} D}{\mu} = 7200, \tag{4.2}$$

$$\mathrm{St} = \frac{fD}{u_{\max}} = 0.038. \tag{4.3}$$

The maximum value of Re suggests that the flow passes to a turbulent regime. As the simulation has been carried out using a turbulent model, turbulent quantities need to be estimated at the inlet as well. An initial guess of the turbulent intensity can be provided by the following expression

$$I = 0.16\mathrm{Re}^{-1/8} \sim 5\%$$

which yields a reasonable approximation for fully-developed internal pipe flows and based on the assumption of isotropic turbulence [55]. The characteristic hydraulic diameter has been set equal to d. In conclusion, at the outlet a constant gauge pressure of 0 Pa has been specified whereas the other boundaries are considered as walls, to which the no-slip condition is applied.

4.5 Valve motion and dynamic mesh

Mechanical heart valves have got the advantage that the leaflets behave as rigid structures. Consequentially, their kinematics can be described by a simple body motion. For this case,

the leaflets form an angle of 10° with the vertical at their maximum opening position and an angle of 70° when they reach the closed configuration. Thus, they perform a rotation of 60° during each cycle. The rotational axes are parallel to the x-axis with coordinates ±2.4894 and -4.86 mm, respectively for the y and z components. However, the motion of the leaflet has been further simplified. In the commercial valve, the motion is governed by a microscopic hinge mechanism which introduces a translation of the leaflets in the streamwise direction. This movement was not implemented in the simulation because of lack of experimental data.

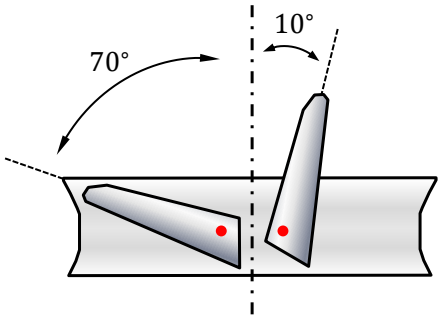

Figure 4.7: Schematics of the rotational kinematics of the leaflets. The red dots represent the axes of rotation.

Experimental opening angles were extracted from a high-speed recording camera. The analysis of the frames showed that the movement of the leaflets is asynchronous. This independent behaviour is more evident during the closure phase. As it can also be seen from the sequence of pictures in Figure 4.8, the leaflet on the right reaches the fully closed configuration with a delay of the order of 20 ms with respect to the other one.

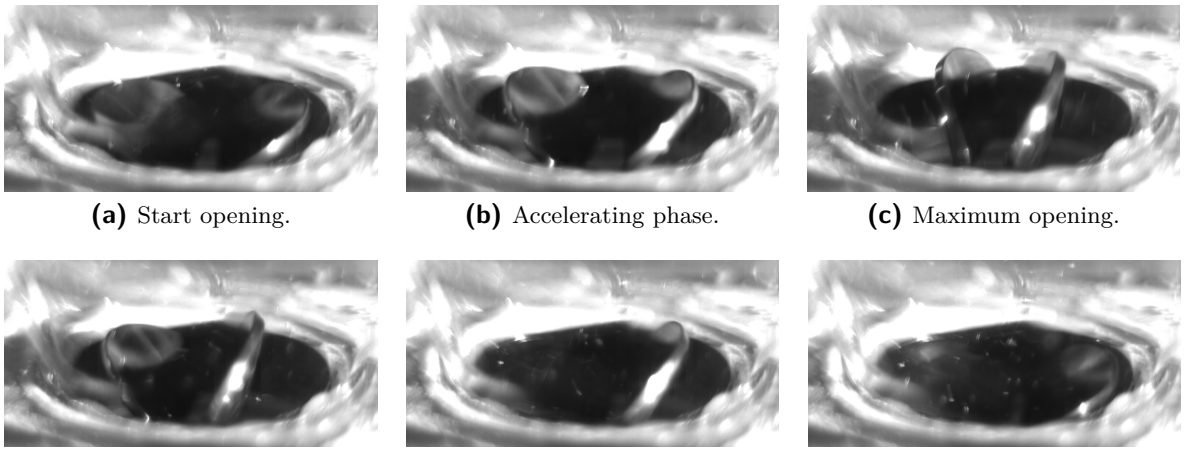

(a) Start opening. **(b)** Accelerating phase. **(c)** Maximum opening.

(d) Start closing. **(e)** Decelerating phase. **(f)** Closed valve.

Figure 4.8: Frames of the experimental valve kinematics for different instants of the cycle. Pictures from Cerroni, with permission [13].

The experimental data set was interpolated using piecewise cubic polynomials. First, results are shown independently for the two leaflets in Figure 4.9. Secondly, a direct comparison of the two cases is presented in Figure 4.10 where the normalised opening angle $\Lambda = (\alpha_{\text{open}} -$

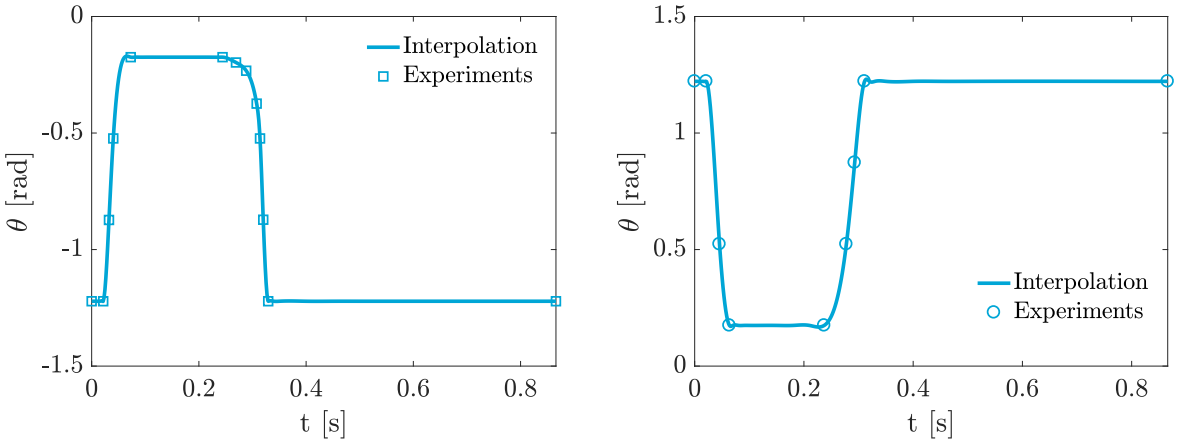

(a) Leaflet 1. **(b)** Leaflet 2.

Figure 4.9: Experimental (symbols) and interpolated (solid line) opening angle as a function of time for the two leaflets of the valve.

$\alpha)/(\alpha_{\text{open}} - \alpha_{\text{closed}})$ is plotted as function of time for one cycle. This graph is primarily shown to emphasise the different closing process of the two leaflets. In addition, the inlet velocity has also been included for reference.

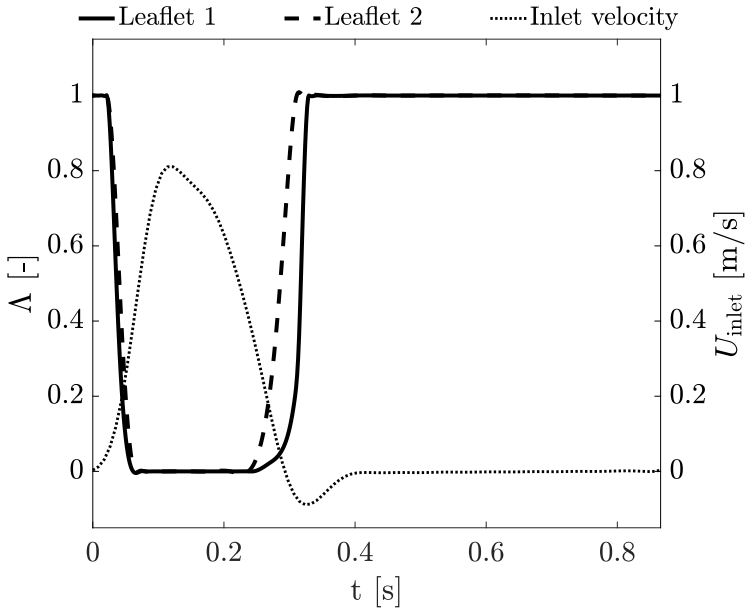

Figure 4.10: Temporal behaviour of the normalised opening angle for the two leaflets and the inlet velocity pulse.

The angular motion has been calculated by taking the derivative of the angle position and the function was implemented in a UDF in a similar approach as explained in section 3.4.

For the three-dimensional case, dynamic mesh was enabled to account for the rotation of

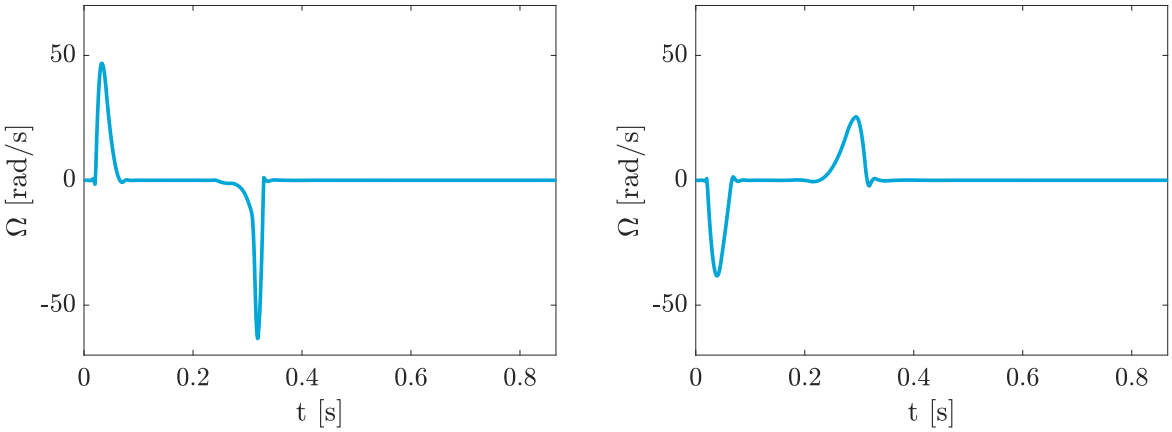

(a) Leaflet 1. **(b)** Leaflet 2.

Figure 4.11: Angular velocity of the two leaflets as function of time.

the leaflets during the simulations. The methods used are smoothing and remeshing. The parameters are presented in Table 4.3.

Table 4.3: Settings of the parameters for the dynamic mesh methods.

Smoothing		Remeshing	
Options	Setting	Options	Setting
Spring Constant Factor	0.5	Minimum Length Scale	0.054 mm
Convergence Tolerance	0.001	Maximum Length Scale	3.6 mm
Number of Iterations	50	Maximum Cell Skewness	0.75
Elements	Tet	Size Remeshing Interval	1

4.6 Simulation methods

The approach adopted in this thesis is the resolution of the RANS equations through the k-ε model. In order to have more details on the available turbulent models, the reader can refer to Appendix E. Moreover, the investigation has been enriched by employing another approach. More specifically, the model was examined with the same mesh but using a laminar mode analysis. This procedure has been conducted in order to be able to evaluate the influence of the turbulent model on the predictions of the flow. The settings for the simulations are summarised in Table 4.4. The residuals were set to 10^{-5} for momentum and turbulent equations and 10^{-4} for continuity. The time step used is $\Delta t = 0.2$ ms. The simulations were first run for one cycle with first order schemes to obtain a proper initialisation of the flow. Then, higher order schemes were employed for other two cycles. The results will be shown for the last one.

Table 4.4: Settings of the parameters for the three-dimensional simulations.

Options	Turbulent settings	Laminar settings
Model	RNG k-ε	Laminar
Near-wall treatment	Enhanced Wall Treatment	-
Solver Type	Pressure-based	Pressure-based
Pressure-velocity Coupling	PISO	PISO
Gradient	Least Squares Cell Based	Least Squares Cell Based
Pressure	Standard	Standard
Momentum	Second Order Upwind	Second Order Upwind
Turbulent quantities	Second Order Upwind	-
Transient Formulation	First Order Implicit	First Order Implicit

4.7 Results

The results are presented for the turbulent case with particular attention to the aortic root region. This part consists of the housing, the valve, the sinuses and the downstream part along the central plane corresponding to x = 0. In addition, two other locations are investigated to be able to compare the outcome of this research with experimental results. These are located at z = 5.41 mm and z = 23.23 mm from the leaflet tip in the opening position.

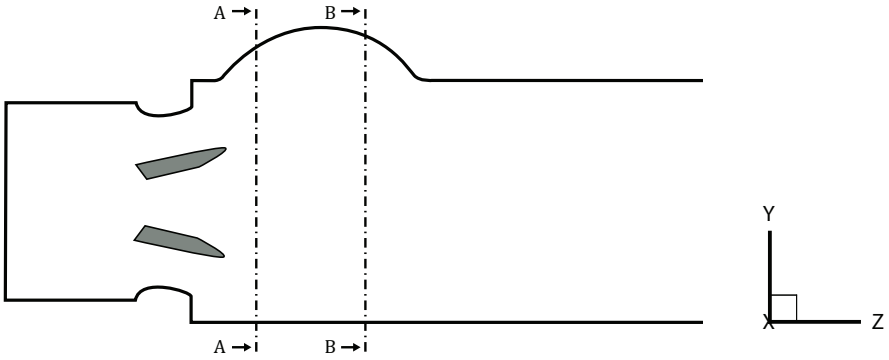

Figure 4.12: Sections A-A and B-B along the plane $x = 0$ for flow investigation.

The results are shown for five different instants of the inlet pulse. These moments coincide with a particular status of the leaflet kinematics and they occur at:

- $t \simeq 30\,\text{ms}$, when the valves start the opening phase;
- $t \simeq 70\,\text{ms}$, when both valves have reached the fully opened configuration;
- $t \simeq 110\,\text{ms}$, when the flow achieves its peak value;
- $t \simeq 230\,\text{ms}$, when the valves start undergoing the closing phase;
- $t \simeq 370\,\text{ms}$, when both valves have reached the fully closed position.

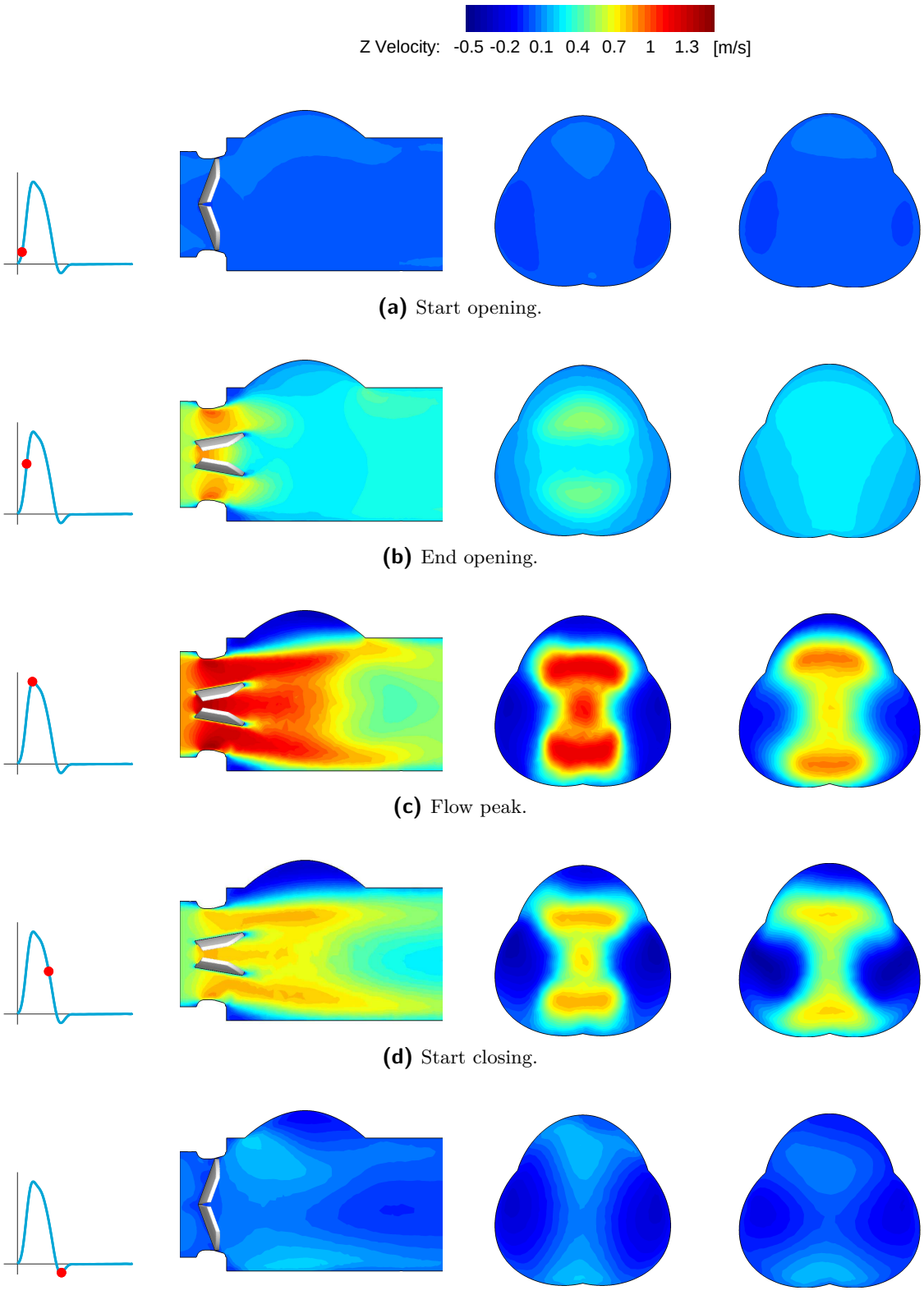

(a) Start opening.

(b) End opening.

(c) Flow peak.

(d) Start closing.

(e) End closing.

Figure 4.13: Velocity contours at five different time instants of the flow pulse along x = 0 and at sections A-A and B-B.

Figure 4.13 shows the streamwise velocity contours. At the beginning of the cycle, the flow appears quite stationary because of the absence of the mean flow during the diastolic part of the previous cycle. Later, the flow gradually develops at the onset of the rotation of the leaflets. When the opening phase is complete, the two lateral jets are more prominent than the central one. The reason is due to the motion of the leaflets whose kinematics favours the passage of the flow into the two lateral orifices and causes a delay of the flow in the central opening. The flow continues accelerating and at the flow peak, the three jets are well formed and they reach the maximum intensities. At the same instant, a vortex arises and a recirculating region is visible in the sinus cavity. When the valve begins to close, the main features of the flow remain almost the same but the intensity of the jets has decreased. As the decelerating phase takes place, the jets start decaying in an asymmetric manner. In fact, the jet on the side close to the sinus lasts longer than the other two. Finally, the valves reach the fully closed position at the negative peak of the inlet pulse. In this configuration, backflow of the central flow takes place because of the negative pressure gradient. This phenomenon causes the fluid on the sides to move upwards. In addition, leakage through the gaps is also observed. The same phenomena can be retrieved in the planes passing through the lines A-A and B-B and orthogonal to the central axis. The visualisation of the velocity field on these cross sections gives a more complete picture on the behaviour of the flow.

The vorticity field has been studied in the same locations introduced above and the results are reported in Figure 4.14. In the central plane x = 0, the out-of-plane vorticity, which is defined as

$$\omega_x = \frac{\partial u_z}{\partial y} - \frac{\partial u_y}{\partial z},$$

has been examined. Generally, this component is quite strong close to the leaflets and close to the aortic root wall because of the strong gradients arising from the fulfilment of the no-slip condition. Moreover, the contours confirm the presence of the three jets. The streamwise velocity undergoes an abrupt acceleration along the vertical direction because of the encountering with the jet. These areas are associated with strong vorticity values. The same situation occurs when the velocity field is subject to a decrement but the resulting vorticity field has a negative sign. In the instant corresponding to the flow peak, the vorticity field highlights the presence of a vortex in that region. In the cross sections corresponding to the planes passing through the lines A-A and B-B and orthogonal to the central axis of the domain, the streamwise vorticity component which is defined as

$$\omega_z = \frac{\partial u_y}{\partial x} - \frac{\partial u_x}{\partial y}$$

has been analysed in order to investigate the secondary motions. First of all, it can be seen that the vorticity field is very weak in both locations at the end of the opening phase. By the time the flow reaches its maximum value and a more turbulent regime has established, the vorticity field has become stronger. Then, when the leaflets start closing, the component has decayed in the first location whereas the field has strengthened further downstream. It can be observed that the two sinus cavities which are opposite the one with the other are mainly affected by the arising of stronger vortical structures and this might be induced by the alignment of the leaflets.

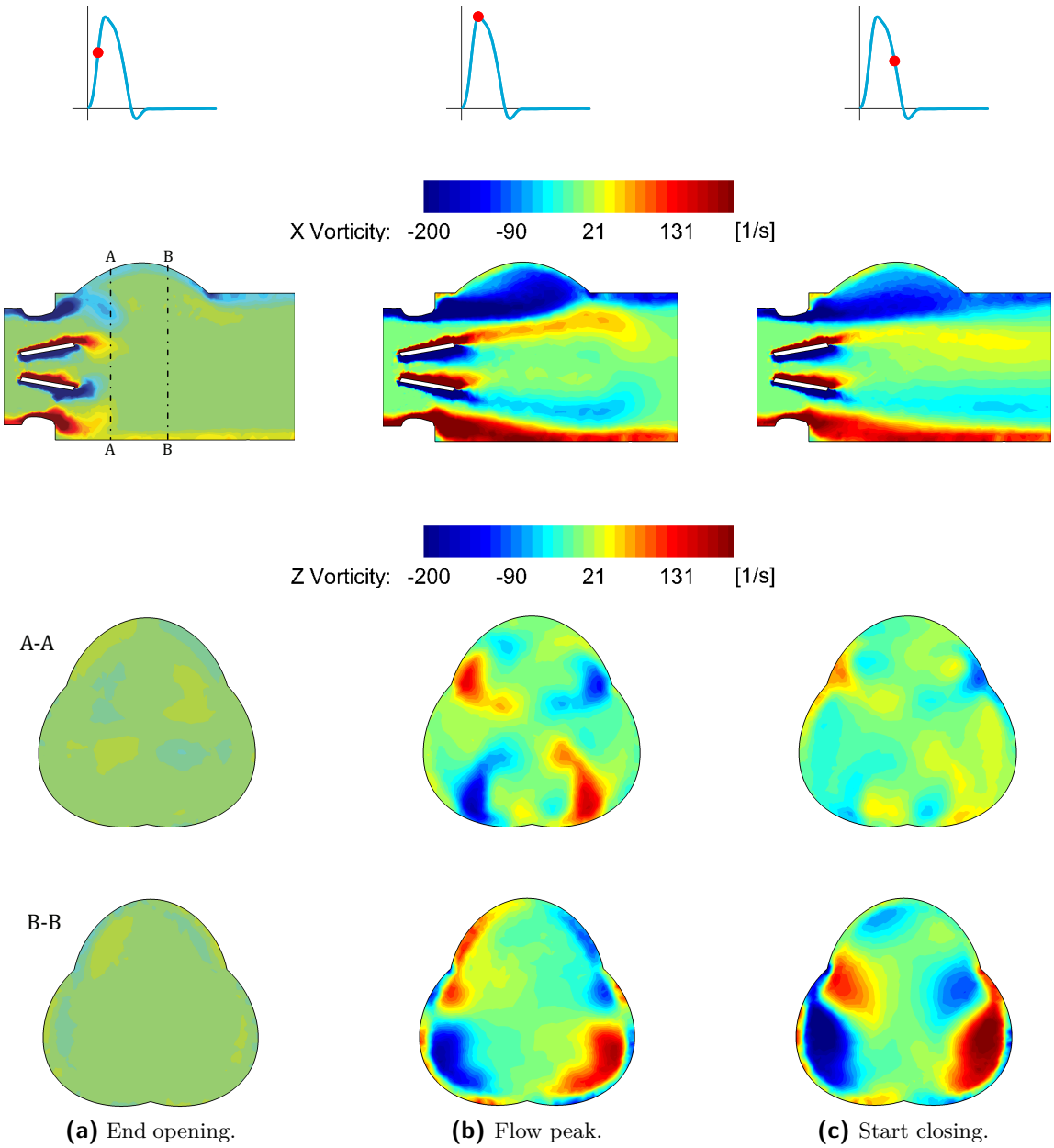

(a) End opening. **(b)** Flow peak. **(c)** Start closing.

Figure 4.14: Azimuthal vorticity contours ω_x in the plane x = 0 and streamwise vorticity contours ω_z along planes z = 5.41 mm and z = 23.23 mm from the leaflets' tips.

Finally, two different turbulent quantities have been analysed, namely the turbulent kinetic energy (TKE) and the eddy viscosity ratio μ_t/μ. TKE indicates the amount of energy associated with the velocity fluctuations. When the flow starts accelerating, the turbulence has declined because of the quiescent flow in the diastolic phase of the preceding cycle. When the valve reaches the fully open configuration, turbulence has not still developed because the flow is still in the transitional region. When the peak value is achieved, the unsteadiness of the flow increases which leads to a production of TKE. This phenomenon continues also during the deceleration of the flow because of the interactions between the recirculation zone in the

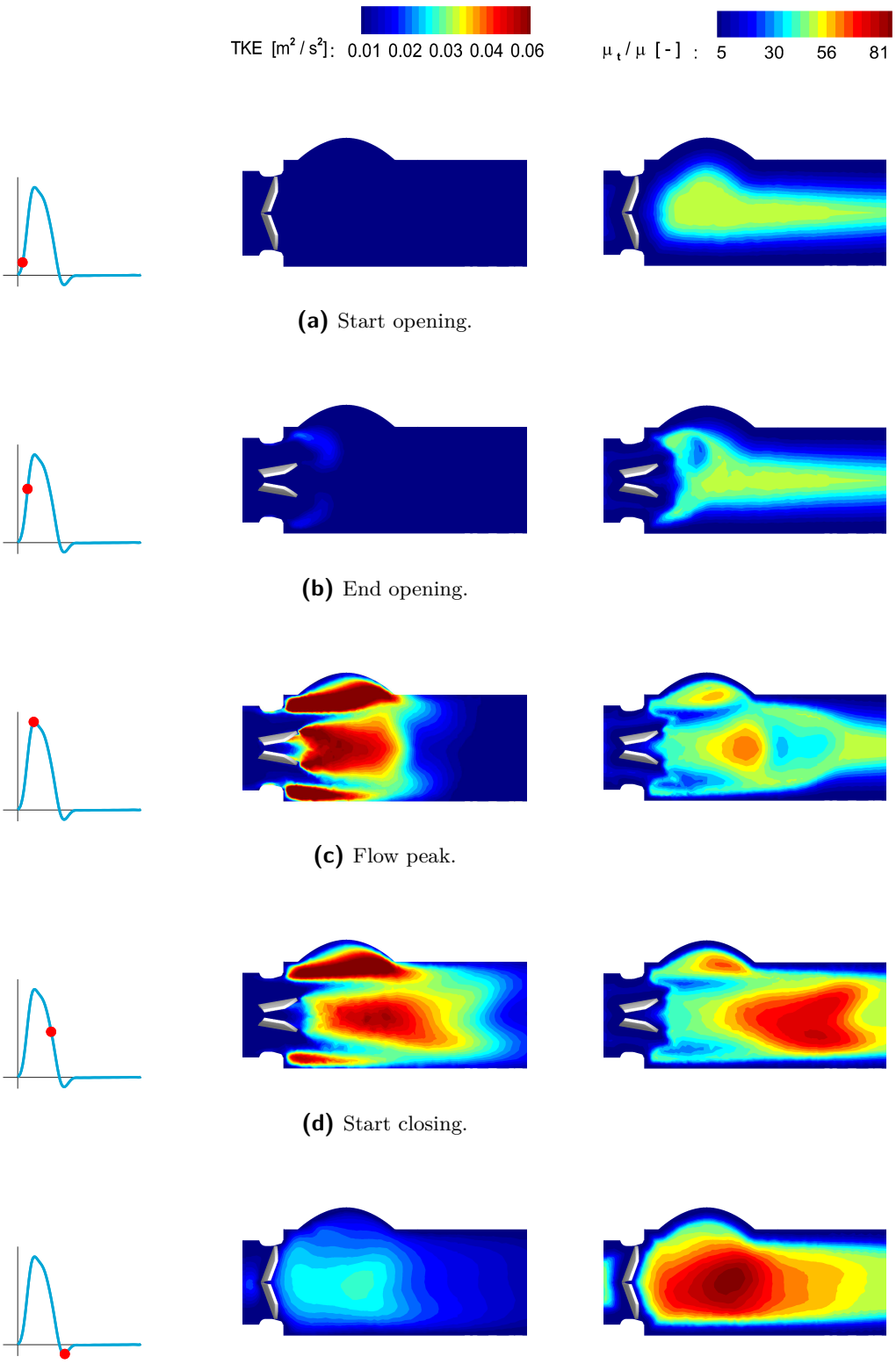

(a) Start opening.

(b) End opening.

(c) Flow peak.

(d) Start closing.

(e) End closing.

Figure 4.15: Contours of turbulent quantities on the plane x = 0 for the five time instants. The left images show turbulent kinetic energy; the right ones present the eddy viscosity ratio μ_t/μ.

sinus and the wake of the jet. Finally, after the valves have reached their closed configuration, turbulence starts decaying and it will eventually disappear up to the beginning of the next cycle. The eddy viscosity ratio is an index of how strong the influence of turbulent viscosity is with respect to the molecular viscosity. Momentum is transferred by the turbulent eddies in the bulk flow in all the cases. This suggests that turbulent mixing is quite strong in the wake of the jets. The highest values are recorded at the beginning of the closing phase and once the valves are completely closed. On the contrary, the molecular viscosity remains always prevalent in the regions close to the wall. In fact, it is where energy is dissipated.

4.8 Validation

In the current research, two methods were employed for the simulations, namely the turbulent model and the laminar approach with coarse grid. In this section, they are compared the one with the other to discuss the respective differences in the performances highlighting strengths or weaknesses of the methods. In addition, the results of the simulations are compared with the experimental and FSI data for the validation [14]. This scope is achieved by the analysis of the velocity profiles along the streamwise direction extracted in the sections already introduced in Figure 4.12.

To begin with, Figure 4.16 shows the profiles obtained along the first location close to the leaflets. At the beginning of the cycle, variations of the flow are not substantially perceived because of the initial quiescent velocity field. When the valve reaches its open configuration, the laminar and the turbulent models show comparable results concerning the acceleration of the flow. However, there are some discrepancies when compared to the FSI and the experimental outcomes. The central jet is not well detected by both the current models meaning that the flow has not completely developed yet. Furthermore, the peaks of the lateral jets are much smaller and they are not aligned with those of the FSI and experimental approaches but they are more shifted towards the central line. At the instant of maximum flow, the laminar case produces higher peaks than the turbulent model and less pronounced interactions between the jets. This behaviour is not surprising because the isotropic modelling of the turbulent viscosity in the k-ε method leads to stronger mixing processes. Therefore, velocity profiles appear to be smeared out. Nevertheless, both cases in question underestimate the maximum velocities when they are compared with FSI simulations and experiments. The recirculation zone in the sinus region is slightly more well resolved in the laminar case than in the turbulent model and it shows reasonable agreement with the result of FSI data. Similarly, the same observations are valid for the case when the leaflets start closing: qualitatively, the three-jet structures are retrieved but the maximum values do not match.

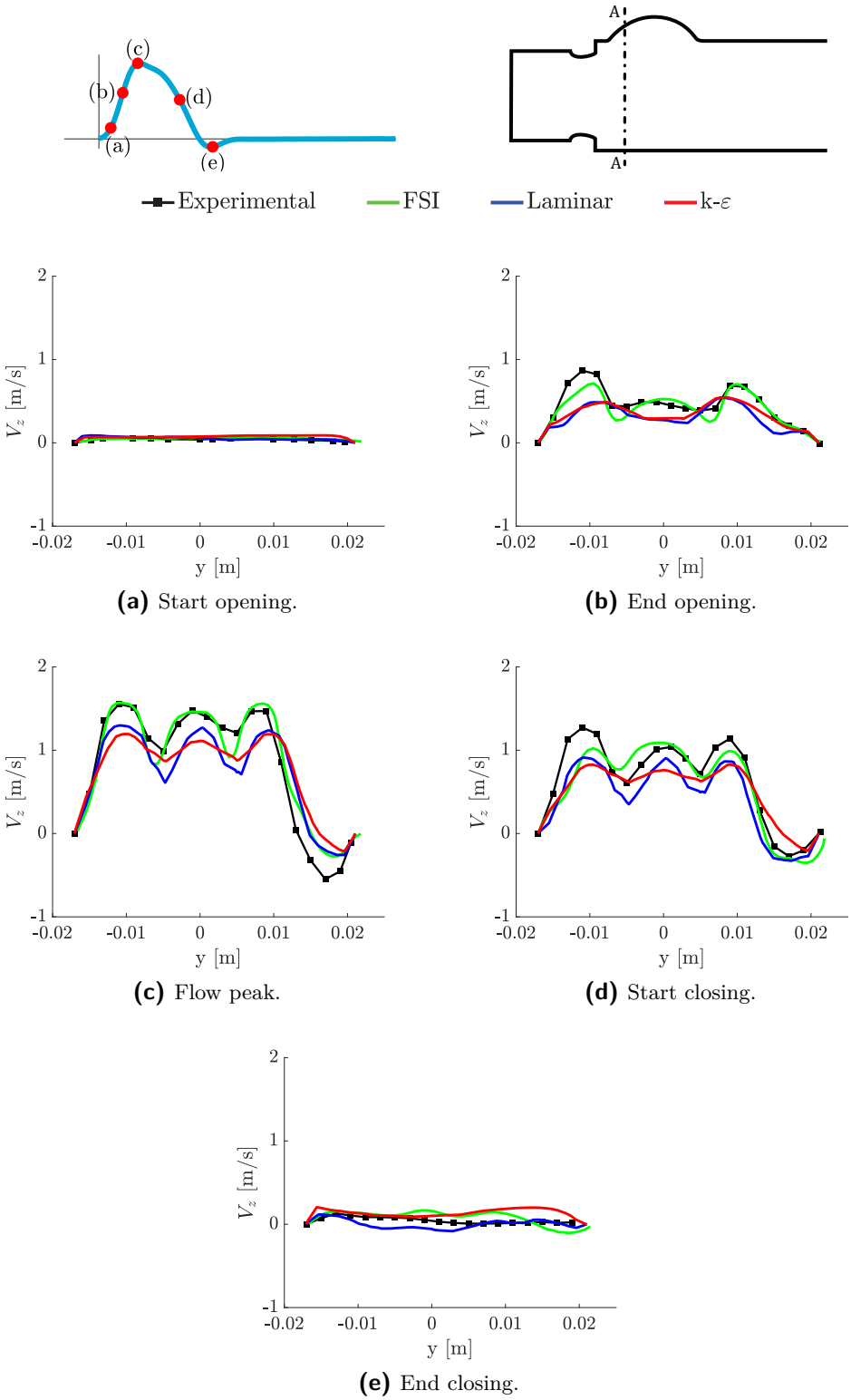

(a) Start opening.

(b) End opening.

(c) Flow peak.

(d) Start closing.

(e) End closing.

Figure 4.16: Streamwise velocity component along section A-A in the central plane at five instants of the flow pulse. Different methods are compared: experimental (black line), FSI (green line), laminar (blue line) and turbulent k-ε model (red line).

Figure 4.17 shows the velocity profiles extracted at the second location further downstream in the sinus region. First of all, it should not be overlooked that the strength of the jets has overall decreased in the wake region; as a consequence, lower values are encountered. The velocity profile appears to be rather flat and constant at the end of the opening phase for all the computational approaches. Comparable to the first location, the laminar and turbulent models are much weaker than the other two methods and they show sharper gradients in the proximity of the walls. The three-jet structure is only visible at the flow peak from the experimental point of view. The laminar model is able to catch this feature although the peaks are overestimated in this case. In contrast, the turbulent model does not distinguish the presence of the central jet because of the intense mixing. In addition, the current methods also reveal the presence of a recirculation zone in the upper part of the sinus region. When the valves start closing, the FSI and laminar methods present the same trend with unstable fluctuations in the central part. The turbulent model qualitatively follows the profile of the experiments despite the fact that the leftmost jet has a lower peak and the central field is more flattened. In the end, all the computational techniques struggle to predict the experimental measurements at the end of the closing phase.

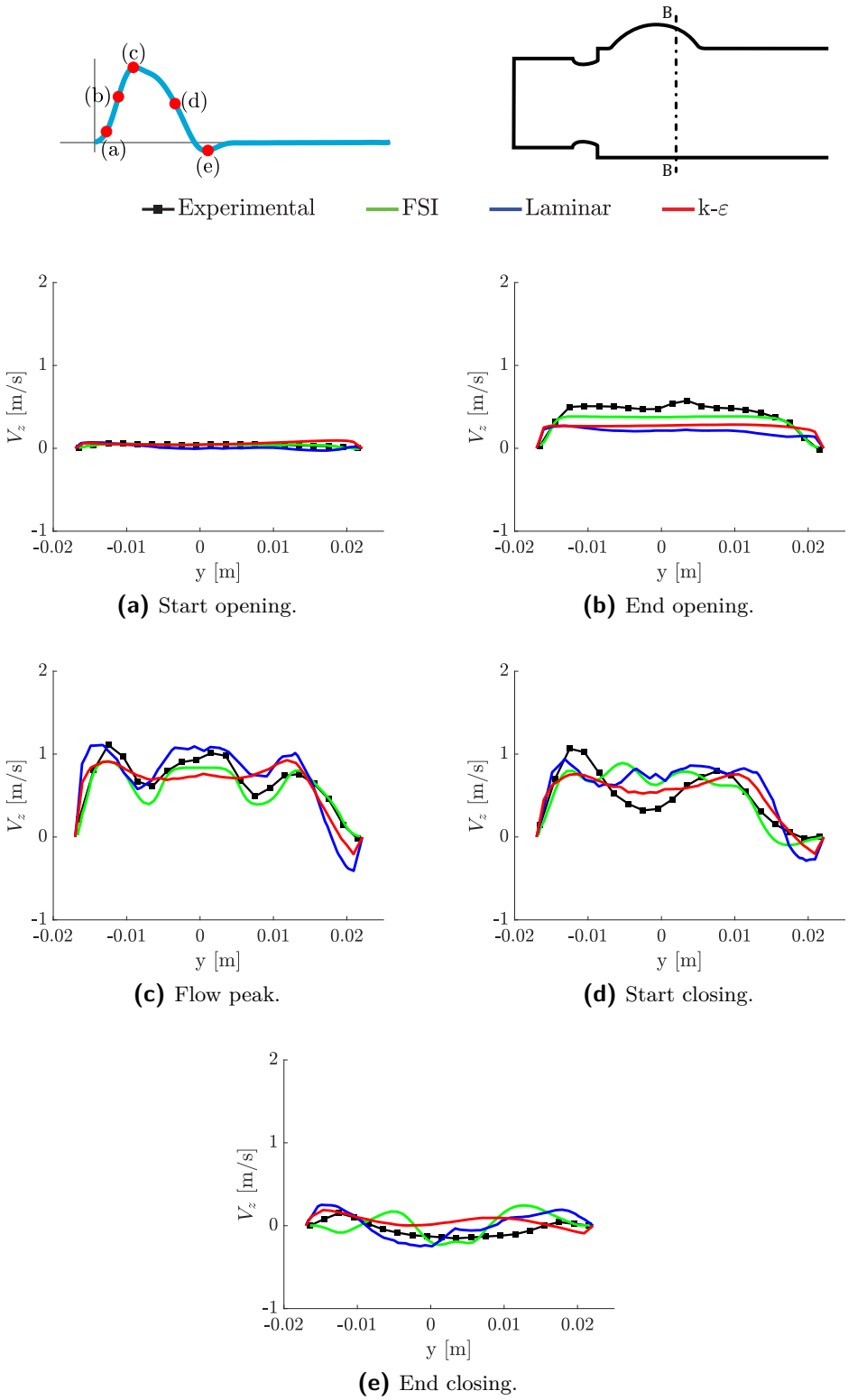

(a) Start opening.

(b) End opening.

(c) Flow peak.

(d) Start closing.

(e) End closing.

Figure 4.17: Streamwise velocity component along section B-B in the central plane at five instants of the flow pulse. Different methods are compared: experimental (black line), FSI (green line), laminar (blue line) and turbulent k-ε model (red line).

4.9 Summary

This chapter extended the same investigating methodology of the two-dimensional case to a more realistic three-dimensional case with the employment of a commercial mechanical bileaflet valve. The kinematics of the leaflet was prescribed in advance and it was taken from experimental measurements described in the initial paragraphs of the chapter. Two simulating approaches were chosen in order to predict the behaviour of the flow. Analysis of the hemodynamics highlights the complexity of the flow especially due to its transition to a turbulent regime. The results have been mainly examined in the central symmetry plane. Velocity contours show the gradual development of three jets as a result of the opening process. These structures are likely to lose strength and eventually decay when the leaflets rotate back to their fully-closed configuration. Out-of-plane vorticity analysis indicates the formation of a recirculating region in the sinus cavity, whereas turbulent quantities underline strong mixing and interactions in the aortic region. Validation of the current research was realised by comparison with experimental data and FSI simulations. Moreover, this analysis is also used in order to assess the powerfulness and the shortcomings of the settings used in the present study. The streamwise velocity component was analysed along two sections in the central plane for the different methods. For the most part, there is qualitative agreement in terms of the evolution of the flow. However, the simulations are not able to match experiments from the numerical point of view as they are characterised by an underestimation of the peaks. In conclusion, these preliminary results are considered to be promising and might lead the way to further investigations and improvements.

5 Conclusions & Recommendations

5.1 General conclusions

The current research dealt with the numerical simulations of the flow through the aortic valve. The main strategy of this analysis was based on prescribing the kinematics of the leaflets *a priori* whose motion was taken from experimental values. The simulations were conducted in the software Ansys Fluent with the aid of the dynamic mesh technique.
The aim of the project was to study the resulting hemodynamics and to verify the influence of the chosen approach on the flow patterns when compared to other investigating techniques such as experimental work and FSI simulations. To achieve this goal, the research was organised in a two-step process.

First, the methodology was tested in a two-dimensional geometry which embodies a simplified representation of the aortic root domain. For this case, the experimental work of Stijnen was followed [12]. The results show the development of a strong vortex in the sinus cavity during deceleration of the flow; furthermore, a secondary weaker counter-rotating vortex evolves just before the complete closure of the valve. The observed phenomena were found to be in line with the PIV measurements and the comparison between computational and experimental data results in a good qualitative agreement. In addition, the current test case was compared with genuine two-way FSI simulations performed within the same group. The streamwise velocity components were analysed for these two numerical methods and the profiles are found to be in good agreement. Little deviations can be explained by the different kinematics of the leaflet. In conclusion, the adopted approach was able to reproduce the proposed case to a great extent.

Secondly, a three-dimensional model was investigated by adopting a commercial bileaflet mechanical valve. For the analysis of the flow, two simulating methods were compared:

- resolution of the unsteady RANS equations with k-ε model;

- laminar simulation with coarse grid without the utilisation of a turbulent model.

The corresponding outcomes do not deviate much the one from the other as both methods are able to predict broadly the general traits of the flow. The results indicate the gradual development of three jets because of the acceleration of the bulk flow and the opening of the valve. Then, the three jets lose intensity as a consequence of the deceleration of the flow and they will eventually decay when the valve returns to its closed state. Transition to turbulent regime brings about the formation of tridimensional and asymmetrical structures. In particular, a vortex develops in the sinus cavity and strong mixing processes take place in the wake region. These results were also validated with experimental work and FSI simulations. For the most part, there is qualitative agreement with the present study in terms of the evolution of the flow. However, the current simulations are not able to match experiments from the numerical point of view as they are characterised by an underestimation of the peaks. In this perspective, the laminar approach yielded slightly better performances than the turbulent model. All in all, these preliminary results are considered to be promising.

All things considered, it can be finally stated that prescribing the motion of the leaflet in advance is an effective method capable of catching the main essential features of the flow with reduced computational costs and without the engagement of the structural solver. Nonetheless, the performances in the tridimensional case suggest that this approach has still room for improvement. For this reason, further test cases could be investigated to obtain more precise information on the flow.

5.2 Recommendations for future research

In light of the results discussed in the previous section, it is possible to introduce new directions to steer the research towards future investigations.

One of the greatest challenging associated to the analysis of flows through mechanical valves is the proper choice of the turbulent model [48]. The employment of the RANS model implies a loss of information because of the smoothing of the small scales. Thus, an alternative proposal can be identified with the use of the Detached Eddy Simulation (DES) model. This method is a hybrid approach which combines the resolution of the RANS equations near the wall but it activates the Large Eddy Simulation (LES) technique in the core region. The advantage of DES is the good compromise between computational costs and accuracy of the solution. This method was already taken into account in this research but imprecise settings did not lead to improvements of the resulting dynamics. Therefore, it needs to be investigated further in order to exploit its potentiality. With this in mind, additional studies can be also extended to pure LES.

Another feasible point of improvement concerns the comparison with experimental data. The validation was only conducted at two specific lines located in the central symmetry plane. In order to be able to have a more complete picture on the three-dimensionality of the flow, it could be recommended to extract and compare profiles on a line which extends in the in-plane direction.

Ultimately, may the current proposed approach turn out to have limitations in predicting the high three-dimensional flow structures, it would be interesting to perform proper FSI simu-

lations. A possible question might be related to quantify the increment in the computational demand in comparison with the overall improvement in the performances.

A

Mathematical models

A.1 Analytical representation of the geometry of the natural AV

The scope of this section is to highlight how the geometry of the aortic valve can be described in terms of mathematical equations. The section follows the work performed by Labrosse *et al.* [24]. For sake of completeness, the procedure to achieve the final formulation will be here explained in details, taking care of carrying out all the steps.

The input parameters can be classified in primary and secondary. The former group has been already presented in 2.1 whereas the latter are hereby introduced and visually summarised in Figure A.1. These are:

1. the angle α between the leaflet and the basal plane in closed position;
2. the coaption height, X_s;
3. the angle Ω between the leaflet free edge and the commissural plane in open position;
4. the height of the commissures, H_s;
5. the angle β between the leaflet and the vertical in open position .

Two different procedures are required, depending on whether the valve is in open or closed configurations.

A.1.1 Open valve representation

Referring to Figure 2.4 and Figure A.1, the free edge of the leaflet L_f spans a circular arc which lies on a plane inclined of the angle Ω with respect to the horizontal. The length of the arc is computed as

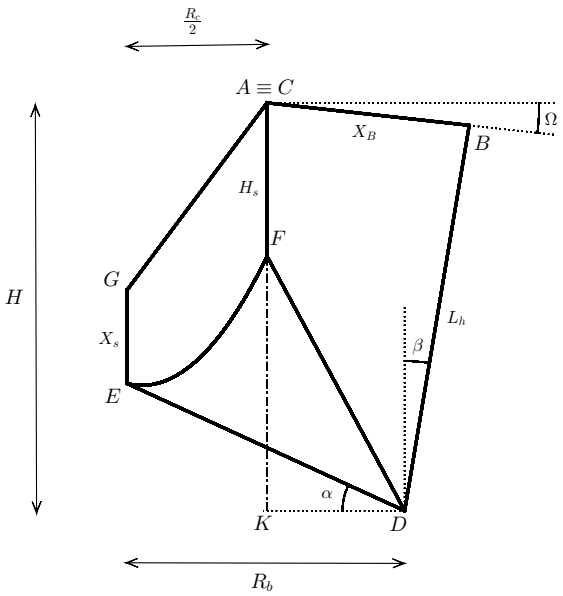

Figure A.1: Side view of one leaflet of the aortic valve in both open and closed configurations. The drawing shows the relevant parameters used for the mathematical formulation.

$$L_f = R\phi \tag{A.1}$$

where R is the radius and ϕ is the angle spanned by the arc expressed in radians. From a projected view on the commissural plane (Fig. A.2), it can be seen that the centre of the arc spanned by L_f does not coincide with the radius of the circle passing through points A and C but it is slightly shifted of a distance d. Thus, some preliminary computations are required to achieve the necessary measures.

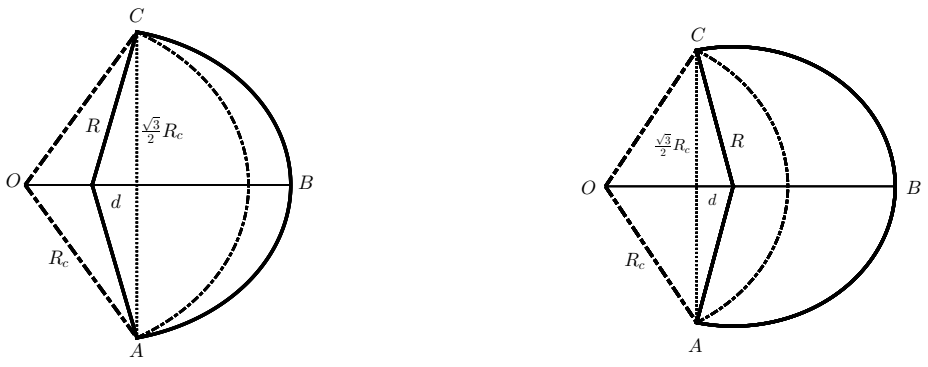

(a) **(b)**

Figure A.2: In *(a)*, top view of the valve when $L_f \leq \pi\frac{\sqrt{3}R_c}{2}$. In *(b)*, the same view when $L_f \geq \pi\frac{\sqrt{3}R_c}{2}$.

First of all, because of the symmetry in the model, the distance between the points A and C is

$$\overline{AC} = 2R_c \sin 60 = \sqrt{3}R_c.$$

Focussing on the right-angled triangle, the radius of the arc R can be found by Pythagoras' theorem as follows

$$R = \sqrt{d^2 + \left(\frac{\sqrt{3}}{2}R_c\right)^2}; \tag{A.2}$$

likewise the angle subtended by the arc is computed as

$$\phi = \begin{cases} 2\arctan\left(\frac{\sqrt{3}Rc}{2d}\right) & \text{if } L_f \leq \pi\frac{\sqrt{3}Rc}{2} \\ 2\left[\pi - \arctan\left(\frac{\sqrt{3}}{2d}Rc\right)\right] & \text{if } L_f \geq \pi\frac{\sqrt{3}Rc}{2} \end{cases} \tag{A.3}$$

Substituting Eq. A.2 and A.3 into Eq. A.1, a non linear equation is derived which can be computed numerically in terms of d if the initial value of L_f is known.

$$L_f = \begin{cases} 2\sqrt{d^2 + \left(\frac{\sqrt{3}}{2}R_c\right)^2}\arctan\left(\frac{\sqrt{3}Rc}{2d}\right) & \text{if } L_f \leq \pi\frac{\sqrt{3}Rc}{2} \\ 2\sqrt{d^2 + \left(\frac{\sqrt{3}}{2}R_c\right)^2}\left[\pi - \arctan\left(\frac{\sqrt{3}}{2d}Rc\right)\right] & \text{if } L_f \geq \pi\frac{\sqrt{3}Rc}{2} \end{cases}$$

Once that d and R are fully resolved, the distance between the commissure point and the middle point of the arc spanned by L_f can be derived. More in details, it is called X_b and it is defined as

$$X_B = \begin{cases} R - d & \text{if } L_f \leq \pi\frac{\sqrt{3}}{2}Rc \\ R + d & \text{if } L_f \geq \pi\frac{\sqrt{3}}{2}Rc \end{cases}$$

At this stage, all the necessary elements to characterise the angle Ω have been determined. To begin with, it can be expressed as a subtraction of two angles as:

$$\Omega = \frac{\pi}{2} - \widehat{KAD} - \widehat{DAB}. \tag{A.4}$$

To find a mathematical relation in terms of the geometrical components, the two angles introduced in Eq. A.4 need to be pointed out. $\widehat{KAD}$ can be found using goniometric relations applied to the triangle KAD:

$$\begin{aligned} \widehat{KAD} &= \arctan\left(\frac{\overline{KD}}{\overline{AK}}\right) \\ &= \arctan\left(\frac{R_b - \frac{R_c}{2}}{H}\right), \end{aligned} \tag{A.5}$$

whereas $\widehat{DAB}$ can be derived from the law of the cosine (Eq. A.6) applied to the triangle ABD.

$$\overline{DB}^2 = \overline{AD}^2 + \overline{AB}^2 - 2\overline{AD}\,\overline{AB}\cos\widehat{DAB} \tag{A.6}$$

Eq. A.6 can be manipulated and solved for the angle as follows

$$\begin{aligned} \widehat{DAB} &= \arccos\left(\frac{\overline{AD}^2+\overline{AB}^2-\overline{DB}^2}{2\overline{AD}\,\overline{AB}}\right) \\ &= \arccos\left(\frac{\left[\left(R_b-\frac{R_c}{2}\right)^2+H^2\right]+X_B^2-L_h^2}{2X_B\sqrt{\left(R_b-\frac{R_c}{2}\right)^2+H^2}}\right) \end{aligned} \tag{A.7}$$

Substituting Eq. A.5 and A.7 into Eq. A.4 and noting that

$$\arcsin\delta = \frac{\pi}{2} - \arccos\delta,$$

a formulation for the angle Ω can be finally expressed as:

$$\Omega = \arcsin\left(\frac{\left[\left(R_b-\frac{R_c}{2}\right)^2+H^2\right]+X_B^2-L_h^2}{2X_B\sqrt{\left(R_b-\frac{R_c}{2}\right)^2+H^2}}\right) - \arctan\left(\frac{R_b-\frac{R_c}{2}}{H}\right)$$

In conclusion, the angle β which the open leaflet forms with the vertical is left to compute. Calling B' the projection of the vertex B onto the horizontal line passing through the commissure (Fig. A.1), the value can be derived using geometrical and goniometric relations as follows,

$$\begin{aligned} \beta &= \arcsin\left(\frac{\overline{AB'}-\overline{KD}}{DB}\right) \\ &= \arcsin\left(\frac{X_B\cos\Omega-\left(R_b-\frac{R_c}{2}\right)}{L_h}\right). \end{aligned}$$

A.1.2 Closed valve configuration

The mathematical representation of the closed configuration is more straightforward. As a matter of fact, it is mainly driven by geometrical relations that can be derived from Figure A.1. In particular, the free-edge length L_f is given by

$$L_f = 2\sqrt{R_c^2 + (H - X_s - R_b \tan\alpha)^2};$$

the total leaflet height results from the sum of two segments, namely coaptation height X_s and the length of the load-bearing surface.

$$L_h = \overline{DE} + \overline{EG}$$

The equations above simultaneously describe the model through a system of nonlinear equations in the unknowns X_s and α according to

$$\begin{cases} L_f^2 = 4[R_c^2 + (H - X_s - R_b \tan\alpha)^2] \\ L_h = X_s + \frac{R_b}{\cos\alpha} \end{cases}$$

To complete the geometrical description of the aortic valve, one last dimension needs to be defined. This is the commissure height, H_s. To do so, the plane where the attachment line lies needs to be identified first. By assumption, this plane is considered to be the mirroring plane between the open and closed configurations. Thus, the attachment line divides the angle θ into two equal parts. Specifically, θ can be computed as

$$\theta = \frac{\pi}{2} - \alpha + \beta$$

and the mirroring plane is found at angle $\alpha + \frac{\theta}{2}$ with respect to the horizontal plane.

Following, the height of the commissures H_s is computed by geometrical derivations

$$\begin{aligned} H_s &= \overline{AK} - \overline{FK} \\ &= H - \left(Rb - \tfrac{R_c}{2}\right) \tan\left(\alpha + \tfrac{\theta}{2}\right). \end{aligned}$$

These equations were implemented in a code to derive the values of the quantities starting from the input parameters. The results were used to create three dimensional representations of the valve by means of ANSYS DesignModeler. Examples of the outcome are shown in Figure A.3 and Figure A.4.

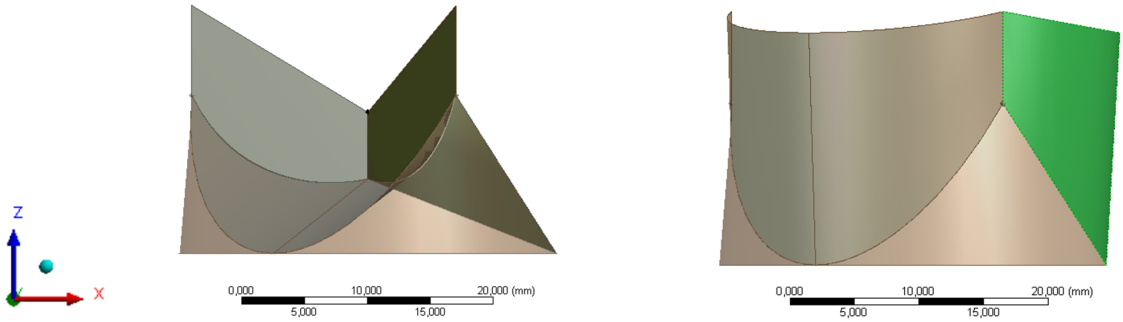

(a) Closed configuration. **(b)** Open configuration.

Figure A.3: Side view of the constructed trileaflet AV. One cusp is highlighted with a different brighter shade.

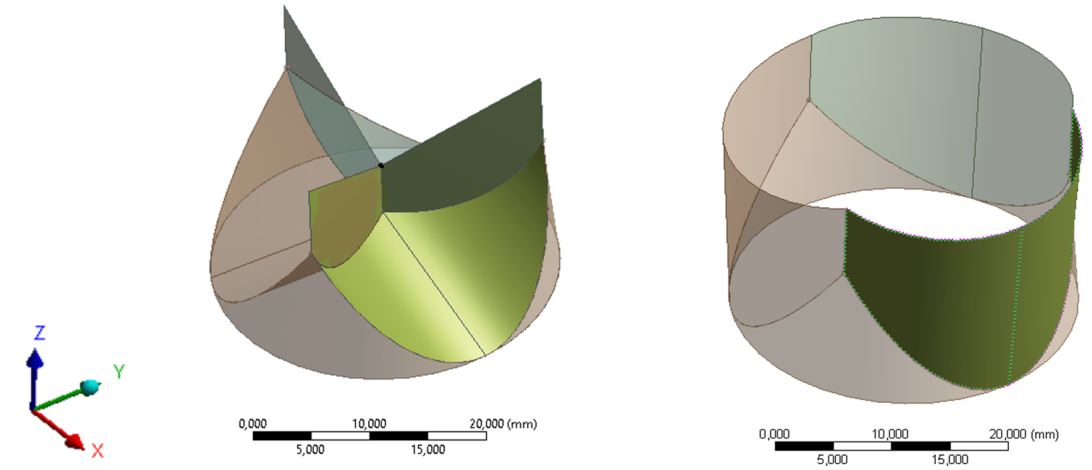

(a) Closed configuration. **(b)** Open configuration.

Figure A.4: Space view of the constructed trileaflet AV. One cusp is highlighted with a different brighter shade.

B

Dynamic mesh theory

The intention of this Appendix is to provide an insightful explanation of the concepts and theory used by the software Ansys Fluent regarding the dynamic mesh models. The theory presented here is taken from Ansys Fluent 15.0 Theory guide [56].

B.1 Dynamic mesh models

As already introduced in section 2.5.1, the dynamic mesh model is used when the shape of the domain changes with time because of moving objects or boundaries. As initial inputs, the model requires an initial mesh and the description of the motion for each of the moving zones. The motion can be formulated by using UDFs, boundary profiles or Six Degree of Freedom (6DOF) solver. The volume mesh is automatically updated at each time step. Three methods are available to adjust the mesh subject to motion or deformation. Namely, these are:

- smoothing methods;
- dynamic layering;
- local remeshing techniques.

B.1.1 Smoothing methods

The main characteristic of the smoothing methods is that they do not alter the total number of nodes in the mesh and the way these are connected. Different categories can be distinguished according to the working principle.

Spring-based smoothing method

In the spring-based smoothing method, every edge connecting two distinct nodes is associated to a spring.

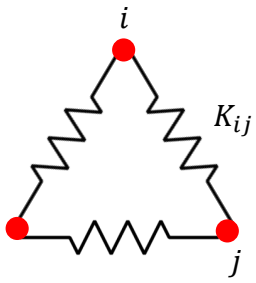

Figure B.1: Representation of the equivalent structure of the mesh with interconnecting springs.

The initial spacing between the nodes represents the equilibrium state. Then, the nodes are displaced because of motion of the mesh. The displacement triggers a force on the springs according to Hook's law. The force $\vec{F}_i$ acting on node i with its neighbouring node j is expressed as

$$\vec{F}_i = \sum_{j}^{n_i} K_{ij}(\Delta\vec{x}_j - \Delta\vec{x}_i) \tag{B.1}$$

where $\Delta\vec{x}_i$ and $\Delta\vec{x}_j$ are the displacements of the adjacent nodes and n_i is the number of nodes connected to i. The parameter K_{ij} is the spring constant and it is defined as

$$K_{ij} = \frac{1}{\sqrt{(||\vec{x}_i - \vec{x}_j||)}}.$$

At equilibrium, the sum of the forces acting on the node i must be zero. Applying this condition to Equation B.1 allows to derive an expression to find the displacement of the node. The iterative procedure results in

$$\Delta\vec{x}_i^{m+1} = \frac{\sum_j^{n_i} K_{ij}\Delta\vec{x}_j^m}{\sum_j^{n_i} K_{ij}}.$$

When convergence is reached, the position of the node is updated according to

$$\vec{x}_i^{n+1} = \vec{x}_i^n + \Delta\vec{x}_i^{m,\text{converged}},$$

where $n+1$ and n refer to the next and the current time step.
The user can select different parameters in order to control the solution of these equations. For instance, the influence of the spring stiffness can be regulated by the Spring Constant Factor. It takes as input a number between 0 and 1. A value of 0 means that no damping

is applied on the springs and the motion of the internal nodes is influenced more by the boundary nodes. On the contrary, a value of 1 applies the actual value of damping on the internal node displacement. Other parameters which can be imposed to reach convergence are the Convergence Tolerance and the Number of Iterations

Diffusion-based smoothing method

In the diffusion-based smoothing method, the smoothing process is ruled by the diffusion equation

$$\nabla \cdot (\gamma \nabla \vec{u}_b) = 0,$$

where $\vec{u}_b$ stands for the moving mesh velocity and γ is the diffusion coefficient. The parameter γ is an index of how much the interior nodes are affected by the boundary motion. It can be either constant or non uniform. There are two formulations for γ:

- the first one depends on a normalised boundary distance d, such that $\gamma = 1/d^{\alpha}$;
- the second depends on a normalised volume cell V, such that $\gamma = 1/V^{\alpha}$.

In the previous expressions, α is a user parameter provided that it is bigger than zero. From the computational point of view, this method is quite expensive since it requires the resolution of a partial differential equation. However, it produces good quality meshes, allowing for large boundary deformations.

Laplacian smoothing method

The Laplacian smoothing method adjusts the location of each vertex of the mesh to the geometric centre of its neighbouring vertices. The main advantage of this method is that it is computationally inexpensive. However, it does not always guarantee an improvement on the mesh quality. Therefore, the update of the mesh only occurs if the maximum skewness of the faces adjacent to the node i is improved. The new node position is defined as

$$\vec{x}_i^{m+1} = (1-\beta)\vec{x}_i^{m} + \beta\overline{\vec{x}_i^{m}},$$

where β is the boundary node relaxation factor and $\overline{\vec{x}_i^{m}}$ is the averaged position of node i at iteration m.

Boundary layer smoothing method

The boundary layer method is especially applied to preserve the height of the boundary layers when the mesh is moving and deforming.

B.1.2 Dynamic layering

The dynamic layering is principally used for prismatic and hexa meshes. This method is based on adding or removing layers of cells adjacent to a moving boundary. In case the moving part is an internal zone, the layers of cells on both sides are marked for remeshing. The criterion of splitting and merging a layer j with layer i depends on the height h of the deforming layer.

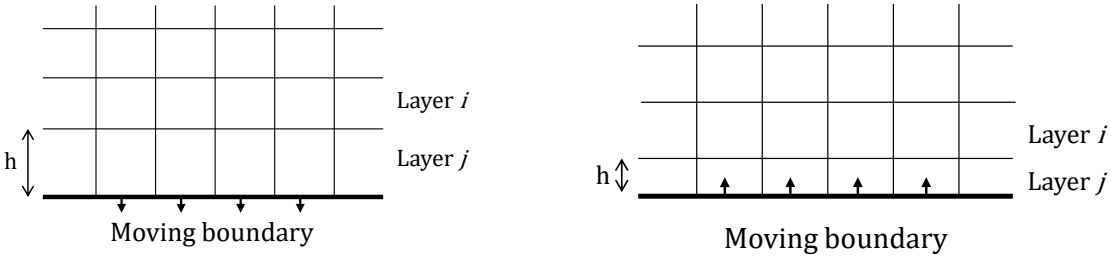

(a) Expansion. **(b)** Compression

Figure B.2: Dynamic layering model.

In case of expansion of a layer, the height is allowed to increase until

$$h_{\min} > (1 + \alpha_s) h_{\text{ideal}}$$

where α_s is known as layer split factor. The cells are split so two new layers are formed of height h_{ideal} and $h - h_{\text{ideal}}$. The ideal height h_{ideal} is defined by the user so it can be either fixed or time dependent. On the contrary, compression of a layer follows the law

$$h_{\min} = \alpha_c h_{\text{ideal}}$$

where α_c is defined as layer collapse factor.

B.1.3 Remeshing techniques

The quality of the mesh can be negatively affected when the displacement of the moving zones is large compared to the mesh size. The presence of distorted or invalid elements such as negative volume cells can lead to convergence problems. In order to circumvent this issue, remeshing techniques are employed. If there are cells which do not fulfil specific criteria related to size or skewness, the solver combines them in order to recreate new elements. Then, these are used to update the solution at the next time step.

Local remeshing

Local remeshing is the commonly used remeshing technique of Ansys Fluent. When it is enabled, each cell is evaluated to check if its skewness and size measures are below an acceptable

limit. The skewness factor is specified by the Maximum Cell Skewness. Default values are 0.6 for 2D and 0.9 for 3D simulations. The size criteria are determined by the Maximum Length Scale and Minimum Length Scale. The cell is marked for remeshing if:

- the skewness factor overcomes the maximum skewness value;
- it is smaller than the miminum length scale;
- it is greater than the maximum length scale.

An alternative local remeshing method makes use of size distributions in order to determine which cells need to be remeshed. The size distribution is generated by a size function which can be controlled by the Size Resolution Function and the Size Function Rate parameters. The mathematical theory to derive the size functions is beyond the scope of this thesis. The reader is advised to consult the manual for further details [56].

B.1.4 `DEFINE_CG_MOTION` macro

The motion of a dynamic zone can be specified by a UDF. In this thesis, the macro `DEFINE_CG_MOTION` has been selected to specify the linear and angular velocities at every time step. These are used by the software to automatically update the node positions of the mesh based on a solid-body motion. The function is fully determined by six arguments and it is structured as follows:

`DEFINE_CG_MOTION(name, dt, vel, omega, time, dtime).`

where

- `name` is the name of the motion supplied by the user;
- `dt` is the pointer which refers to the dynamic zone ID;
- `vel[]` is the array of linear velocity;
- `omega[]` is the array of angular velocity;
- `time` is the current flow time;
- `dtime` is the time step of the simulation.

The values of `dt`, `time` and `dtime` are supplied by the solver to the UDF; instead, the outputs are `vel` and `omega` which are returned to the solver of Fluent.

C

Numerical theory

This section aims to present the computational methods used by the solver. Particular attention is dedicated to the equations and differentiation schemes used in this thesis. The theory presented here is taken from Ansys Fluent 15.0 Theory guide [56].

C.1 Discretisation schemes

Fluent solver is based on the Finite Volume Method. In this method, the domain is divided into a finite set of control volumes. The governing partial differential equations are applied to each element of the domain and they are solved by numerical integration. This paragraph gives a general overview of the most used discretisation schemes which are implemented in the software in order to derive the solution field.

C.1.1 Spatial discretisation

Spatial discretisation schemes are used in order to derive quantities at cell faces by interpolation of the values stored in the cell centres. Values at the faces are required in order to compute convective terms. Figure C.1 represents a two dimensional grid with a highlighted control volume with node C. It can be used as reference for the explanation of the different methods in the following sections.

First-order upwind

First-order upwind method is acceptable when the flow is simple and well aligned with the mesh. If this condition is not fulfilled, especially for triangular and tetrahedral meshes, this discretisation scheme negatively affects the overall accuracy of the solution because of the introduction of numerical diffusion. However, the advantage is that it generally yields better

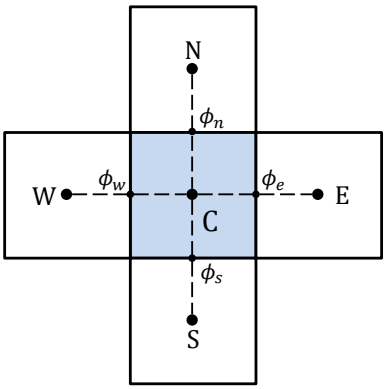

Figure C.1: Schematic drawing of a two-dimensional grid discretisation.

convergence so sometimes it is preferred for few initial iterations before switching to higher order schemes. For a first-order accuracy, the value ϕ at the centre of the cell is considered to be a cell-average value. Thus, quantities at cell surfaces are taken equal to the value of the upstream cell centre. In particular,

$$\phi_w = \begin{cases} \phi_W, & \text{if } u_x > 0, \\ \phi_C, & \text{if } u_x < 0. \end{cases}$$

Second-order upwind

Second-order upwind method is to be preferred because it yields better accuracy. The value at the faces of the cell ϕ_f is computed through a Taylor expansion as in

$$\phi_f = \phi_u + (\nabla\phi)_u \cdot \vec{r}$$

where the subscript u is used to denote the upwind value of ϕ and $\nabla\phi$ and $\vec{r}$ is the displacement vector from the upstream cell centroid to the face centroid. Evaluation of the gradient of a quantity is treated in section C.1.3.

C.1.2 Temporal discretisation

For transient calculations, the terms in the governing equations are to be integrated over a time step Δt. For a simplified expression of the form

$$\frac{\partial\phi}{\partial t} = F(\phi) \tag{C.1}$$

where ϕ is a scalar function and $F(\phi)$ is a function which accounts for any spatial discretisation, both terms in Equation C.1 need to be treated numerically.

The time derivative is discretised in Fluent using a backward difference method. In particular, a first-order accurate scheme is formulated as

$$\frac{\partial \phi}{\partial t} = \frac{\phi^{n+1} - \phi^n}{\Delta t},$$

whereas for a second-order accurate method, the discretisation is written as

$$\frac{\partial \phi}{\partial t} = \frac{3\phi^{n+1} - 4\phi^n + \phi^{n-1}}{2\Delta t}.$$

The right hand side of Equation C.1 can be assessed according to two options. When the function is evaluated at the next time level $F(\phi^{n+1})$, an implicit integration method has been employed. The advantage of this procedure is that it is unconditionally stable with respect to the size of the time step. However, the equation needs to be solved iteratively at each time step. On the other hand, if the right hand side is evaluated at the current time step $F(\phi^n)$, an explicit integration method is used. In this case, the choice of the time step Δt has numerical stability limitations.

C.1.3 Gradient and derivatives evaluation

The evaluation of gradients is required in order to calculate diffusion terms and velocity derivatives. The gradients are computed in Fluent according to three different methods:

1. Green-Gauss Cell-Based;
2. Green-Gauss Node-Based;
3. Least squares Cell-Based.

In general, the Green-Gauss theorem states that the computation of the gradient of a quantity ϕ at the centre of a cell c_0 can be formulated as

$$(\nabla \phi)_{c_0} = \frac{1}{\mathcal{V}} \sum_f \bar{\phi}_f \vec{A}_f \tag{C.2}$$

where $\bar{\phi}_f$ is the value of ϕ at the cell face centroid and summation takes over all the faces surrounding the cell. Evaluation of $\bar{\phi}_f$ in Equation C.2 determines whether the method is either cell or node based. If the Green-Gauss Cell-Based is selected, the quantity is computed by the arithmetic average of two neighbouring cell centres yielding

$$\bar{\phi}_f = \frac{\phi_{c_0} + \phi_{c_1}}{2}.$$

If the Green-Gauss Node-Based is chosen, the quantity is derived from the arithmetic average of the value at the nodes of the cell resulting in

$$\bar{\phi}_f = \frac{1}{N_f} \sum_{n}^{N_f} \bar{\phi}_n,$$

where N_f is the total number of nodes of the face.
The node-based gradient is known to be more accurate than the cell-based gradient particularly on irregular (skewed and distorted) unstructured meshes; however, it is relatively more expensive to compute than the cell-based gradient scheme [56].

The Least-Squared Cell-Based method assumes that the change in cell value varies linearly. The solution is computed from

$$(\nabla\phi)_{c_0} \cdot \Delta r_i = (\phi_{c_i} - \phi_{c_0})$$

where c_0 and c_i are respectively the centres of two neighbouring cells separated by the vector Δr_i. On irregular (skewed and distorted) unstructured meshes, the accuracy of the least-squares gradient method is comparable to that of the node-based gradient [56]. The advantage is that it is less computationally expensive.

C.2 Pressure interpolation

Ansys Fluent uses a collocated scheme meaning that pressure is stored at the centre of the cell. In order to derive the quantity at the cell face, the solver offers different interpolation methods. These are:

- *Linear*: face pressures are computed as the average of the pressure values in the adjacent cells;
- *Standard*: the quantities at cell faces are obtained using momentum equation coefficients. This scheme works well for smooth transition of pressure between cells. Thus, it is not recommended when there are steep gradients or sudden jumps such as in strong swirling flows or flows with large body forces;
- *Second Order*: interpolation is obtained using a central differencing scheme and it may provide better accuracy with respect to the previous two;
- *PRESTO!*: the face pressure is computed using the discrete continuity balance for staggered control volumes.

C.3 Pressure-velocity coupling

In this thesis, the solver used was the pressure-based solver. The algorithm is based on the solution of a pressure equation derived from the manipulations of continuity and momentum equations. The solution of the pressure equation determines the velocity field in such a way that it satisfies mass conservation equation. Because the governing equations are coupled

the one with the other, the solution is reached after an iterative procedure. The pressure-based solver can be either segregated or coupled. In the segregated pressure-based solver, the individual equations are solved independently the one after the other. This method is advantageous from the memory point of view since the discretised equations are stored only one at a time. Figure C.2.a summarises the main steps of the algorithm. There are three main segregated choices in Fluent:

- *SIMPLE*: this iterative method starts with an initial guess of the pressure field in order to compute the velocity. Then, the pressure correction is calculated and it is used to update both pressure and velocity fields. This process is repeated until the residuals are below the stated residual by the user.
- *SIMPLEC*: this procedure is similar to the SIMPLE method. The only difference lies in the expression used for the face flux correction. SIMPLEC method allows to reach faster convergence; however, a skewness correction needs to be accounted for in distorted meshes to avoid instabilities;
- *PISO*: this scheme is similar to SIMPLE family and it is based on the higher degree of the approximate relation between the corrections for pressure and velocity. In order to improve accuracy, the algorithm is able to perform two additional corrections, i.e. neighbour and skewness corrections. PISO is recommended for transient flows with large time steps.

The coupled pressure-based method is based on the simultaneous resolution of the governing equations for pressure and momentum. Then, other remaining variables including turbulence or energy equations are solved in a decoupled manner. This method allows to have a faster rate of convergence than the segregated algorithm but the memory requirement is more demanding since all the discretised equations for pressure and momentum are stored at the same time. Figure C.2.b shows the implementation of the steps.

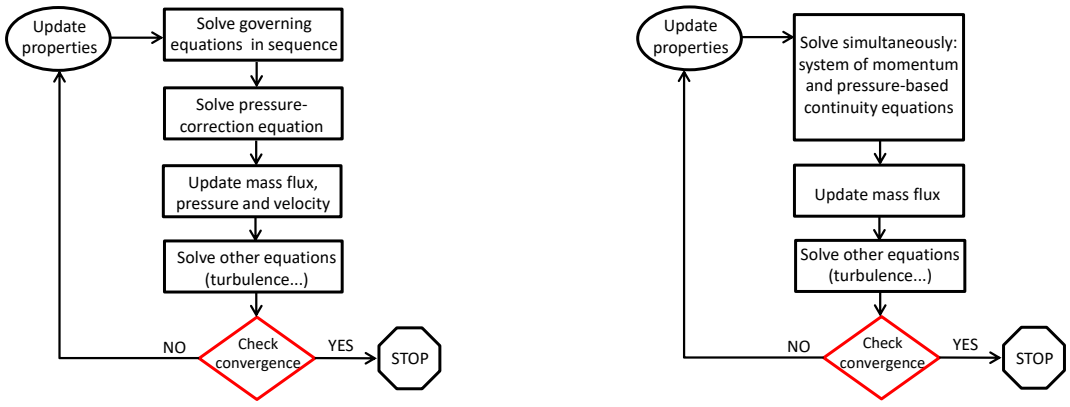

(a) Segregated algorithm. **(b)** Coupled algorithm.

Figure C.2: Implementation of the steps for the two pressure-based solvers.

D

Mesh validation

This Appendix shows the mesh independence tests performed for the analysed cases. Therefore, it is divided in two sections: the first one shows the investigation for the two-dimensional situation whereas the second deals with the three-dimensional case.

D.1 Two-dimensional case

For the two-dimensional case, three meshes have been generated in total in order to test the validation of the simulations. First, a coarse mesh has been generated (Fig. D.1). Then, two sets of refinements have been realised by doubling the number of nodes for each edge. In this manner, the overall cell density differs by a factor 4 when comparing one mesh with the other. The mesh shown in section 3.2 corresponds to the second grid. The refinement mainly produces an effect on the cell size values which reasonably decrease. On the contrary, the quality metre parameters do not necessarily experience a significant improvement. The main features of the three meshes are summarised in Table D.1.

Table D.1: Summary of the parameters of the two-dimensional finer mesh.

Type	Elements	Nodes	Min size [mm]	Max size [mm]	Min skew	Min quality	Max aspect ratio
Coarse	12.5k	6.2k	0.13	1.68	0.76	0.84	3.6
Fine	48.9k	24.3k	0.0575	0.9	0.76	0.88	3.24
Finest	192.9k	96.3k	0.029	0.58	0.88	0.77	3.27

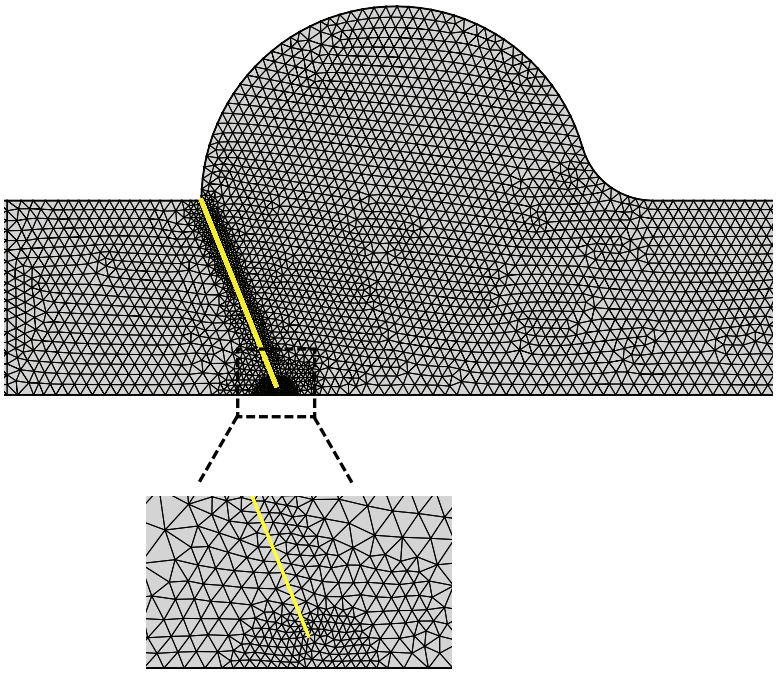

Figure D.1: Two-dimensional coarse grid with magnified gap region. The leaflet is highlighted in yellow.

An investigation of the dynamic mesh parameters was realised for each case after the modification of the mesh. This is required in order to ensure that the quality of the mesh is preserved and to avoid the development of negative volume cells. The settings for smoothing were left unaltered with respect to the base case; on the contrary, the parameters for remeshing needed to be modified according to the new maximum and minimum length scales.

In order to assess grid independence, the velocity components which were recorded in the monitoring points listed in Table 3.6 are compared for the three different grids. Overall, the three meshes give acceptable and similar results. However, the coarser mesh is the one which deviates from the rest of the two especially for monitor point 1, i.e. the point at the centre of the sinus cavity. The deviation is highest during the acceleration of the leaflet and at the onset of reversed back flow. This is explained by the fact that both of these moments are characterised by strong vortexes in the sinus cavity. Thus, for the coarser mesh the number of control volumes is not enough to accurately capture the main features of the flow. The greatest difference is recorded at the beginning of the cycle ($t \sim 0.1$ s) for the y-component of the velocity and it is found to be 75%. In other cases, differences between the coarse and the fine mesh do not overshoot 12%. The other two meshes, respectively the fine and the finest, are in very good agreement. Differences are hardly noticeable and they are confined below 2 % for all the cases analysed. In conclusion, the mesh chosen for the simulation is considered to yield appreciable and reliable results.

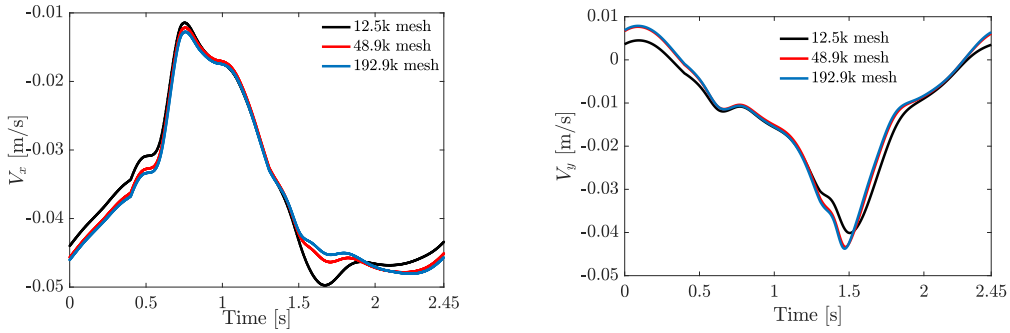

(a) Monitor point 1.

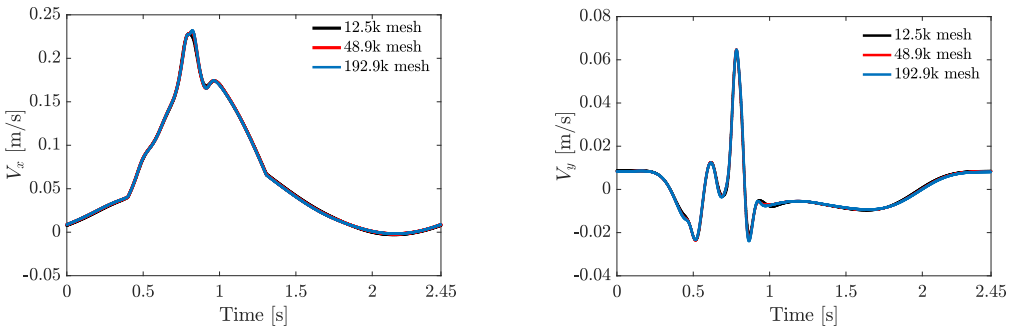

(b) Monitor point 2.

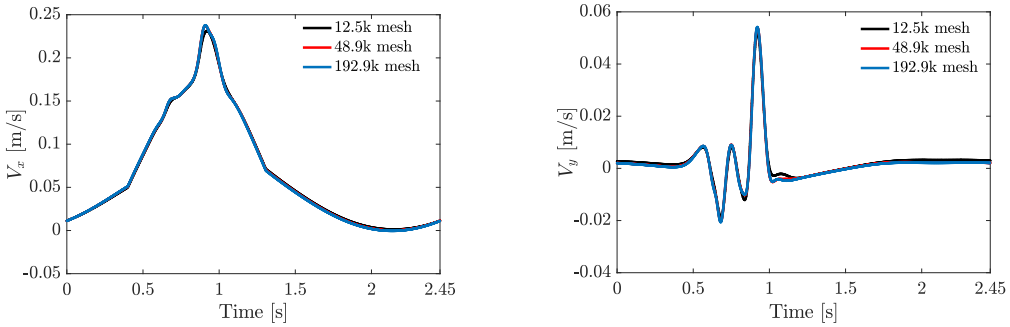

(c) Monitor point 3.

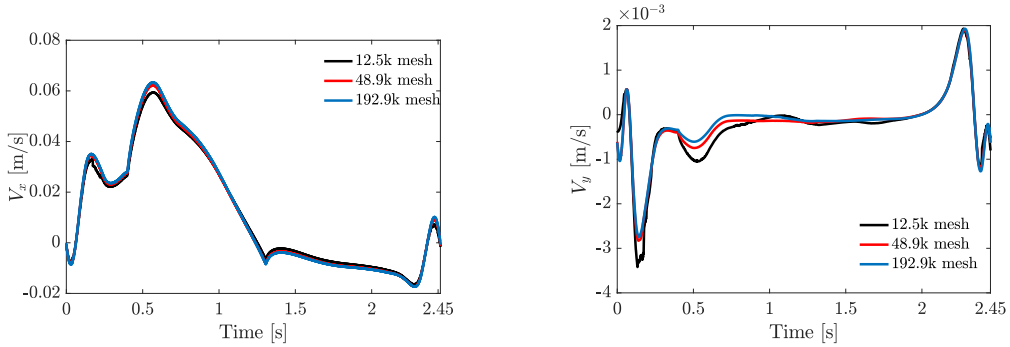

(d) Monitor point 4.

Figure D.2: Mesh dependency check for the x-velocity (left) and y-velocity (right) components.

D.2 Three-dimensional case

For the three-dimensional case, a partial mesh independence test has been conducted. A finer mesh has been generated starting from the one introduced in section 4.3. The refinement has been applied along the spanwise direction. A comparison between the coarse and fine mesh can be observed in Figure D.3. In the end, the overall density of cells is increased by a factor approximately equal to 2.7.

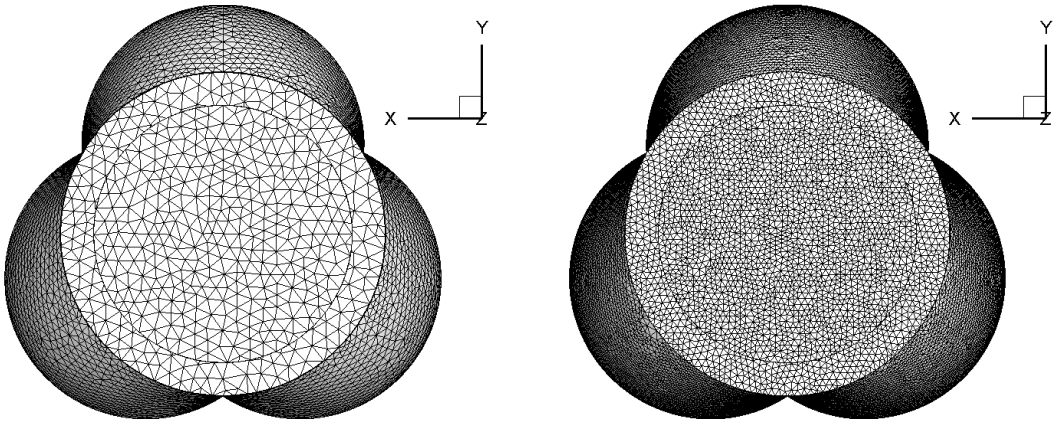

(a) Coarser mesh. **(b)** Finer mesh.

Figure D.3: Top-view comparison of the two meshes for the three-dimensional case.

Table D.2: Summary of the parameters of the three-dimensional finer mesh.

Elements	Nodes	Min size [mm]	Max size [mm]	Min skew	Min quality	Max aspect ratio
3.3M	567k	0.0217	1.66	0.70	0.76	16.3

The simulation was only tested for the laminar case. The performances were first assessed by the analysis of the instantaneous streamwise velocity component at three monitoring points located on the line A-A of Figure 4.12. As it can be seen in Figure D.4, the finer mesh shows a lot of fluctuations and instabilities although the same flow evolution as in the coarser case can be recognised. This can be explained by the fact that the solver is able to capture more vortical structures associated to the smallest scales since the total number of cells has increased. For this reason, three cycles are not enough and further statistical values need to be collected and averaged in order to draw more precise conclusions. The velocity profiles were also compared along the section A-A for different instants of the cycle. The outcome is reported on the left of Figure D.5. There is fair agreement between the two grids at the end of the opening phase. At flow peak, there is a sharp difference between the two cases related to the interaction between the jets. Those computed with the finer mesh undergo less mixing as a consequence of the reduced numerical diffusion. The last case associated to the beginning of the closing phase presents the largest deviations between the two cases. The

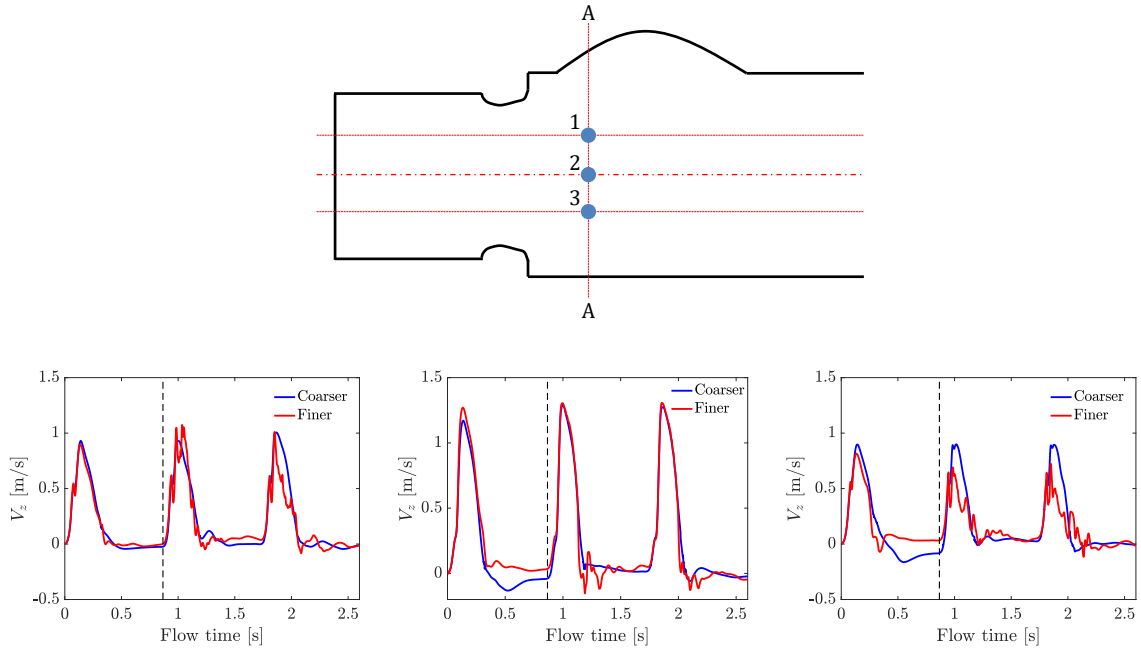

(a) Monitor point 1. **(b)** Monitor point 2. **(c)** Monitor point 3.

Figure D.4: Instantaneous streamwise velocity comparison between coarser (blue line) and finer (red line) grids at the three monitoring points indicated in the sketch above.

finer simulation still shows less interaction between the jets; moreover, the recirculation zone in the sinus cavity is not well resolved as it shows an opposite trend.

For sake of completeness, the comparison of the performances of the two grids is also shown for section B-B of Figure 4.12. The extraction of the z-velocity component for the same time instants is reported on the right of Figure D.5. This location shows analogous features with respect to the previous case. In fact, the two grids yield comparable results for the case in which the valve reaches its open configuration. At flow peak, the reduction of numerical diffusion due to increased number of cells is responsible for the reduced interactions between the jets and for a stronger central jet peak. Besides, the region in the sinus cavity has improved and its prediction is closer to experimental results. Finally, the last case is the one which shows the greatest discrepancies. Compared to the coarser mesh, the refinement has reduced the instabilities in the central part. On the other hand, there is a complete deviation from the experimental case as the central jet still preserves considerable strength. In light of the above results, it can be concluded that grid independence was not entirely achieved.

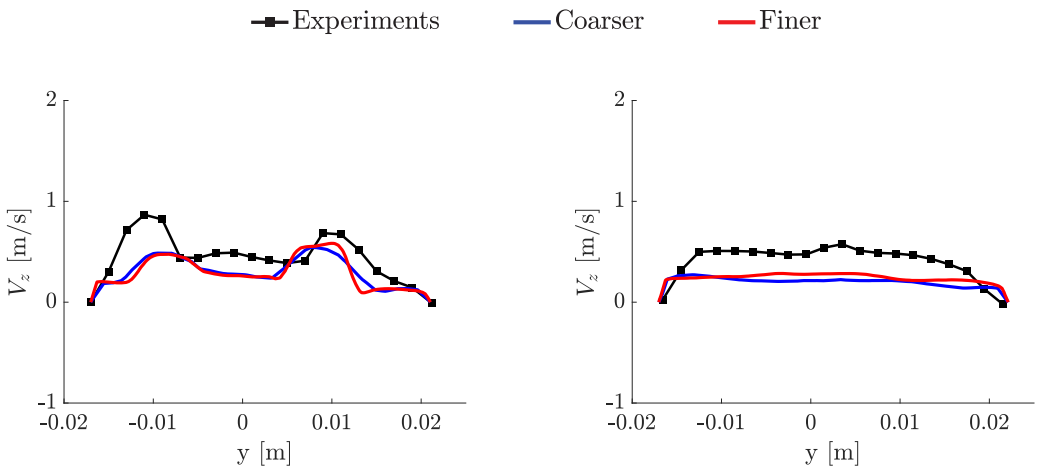

(a) End opening.

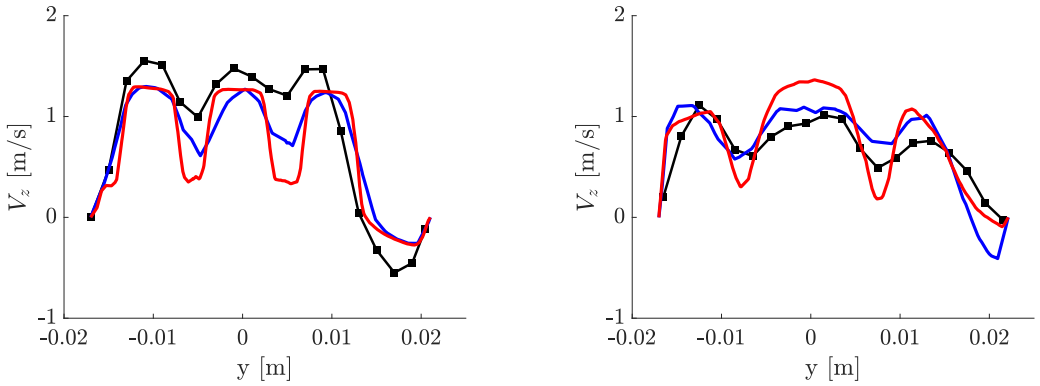

(b) Flow peak.

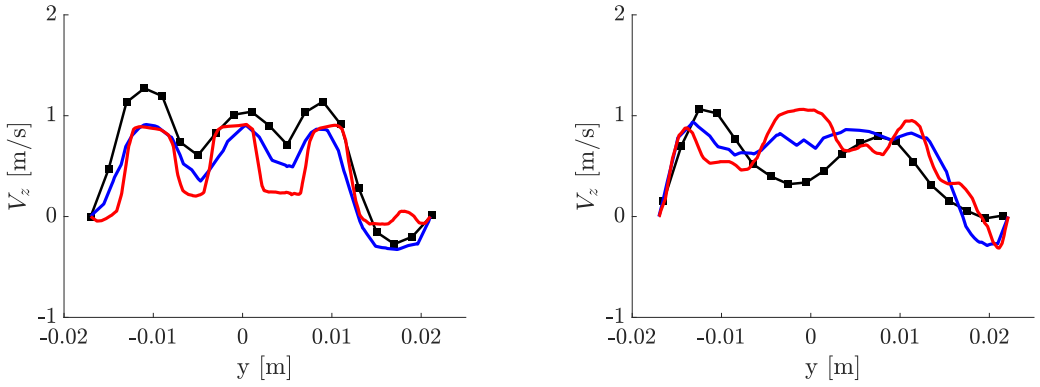

(c) Start closing.

Figure D.5: Streamwise velocity comparison along the line A-A (left) and along line B-B (right) between coarser (blue line) and finer (red line) grids for three different instants of the cycle.

E

Turbulence models

Turbulent flows are chaotic and unstable flows which show fluctuations of the main physical variables. They are commonly characterised by the presence of three-dimensional vortical structures called eddies which eventually break down in smaller whirls. Energy is produced at the large scales and it is transferred from the large eddies to the small ones triggering an energy cascade. At the smallest scales, energy is dissipated by viscosity. This type of regime is also very effective in mixing flow properties such as momentum, kinetic energy, species concentration. The challenge linked to turbulent flows concerns the accurate resolution of all the scales of the spectrum. In particular, there are different techniques to model turbulence. Direct Numerical Simulation (DNS) allows to resolve all the scales of the spectrum. The main shortcoming is in terms of computational costs since very fine grids and small time steps are required. Another alternative is to use the Large Eddy Simulation (LES) method. In this case, large eddies are computed directly whereas the smaller ones are modelled. The governing equations are filtered either by Fourier space or configuration space. Coarser meshes than in DNS are allowed but simulations need to be run for a longer flow time in order to have stable statistics of the flow [56]. Finally, a last approach consists of solving the Reynolds-averaged Navier-Stokes (RANS) equations. By applying a time averaging to the Navier-Stokes equations, the average flow quantities are modelled. In this thesis, this last method was used so it will be discussed further in the next section.

E.1 Governing equations

The idea behind the RANS is to decompose the flow properties into a superposition of a mean and a fluctuating term. For a velocity component, it is represented by $u_i = \bar{u}_i + u_i^{'}$; analogously, for other scalar quantities such as pressure the decomposition results in $\phi = \bar{\phi} + \phi^{'}$. First, these expressions are substituted in the Navier-Stokes equations; then, a time average is performed which leads after some manipulations to the RANS equations. For an incompressible flow,

they are written as

$$\frac{\partial \bar{u}_i}{\partial x_i} = 0 \tag{E.1}$$

$$\frac{\partial \bar{u}_i}{\partial t} + \frac{\partial (\bar{u}_i \bar{u}_j)}{\partial x_j} = -\frac{1}{\rho}\frac{\partial \bar{p}}{\partial x_i} + \nu \frac{\partial^2 \bar{u}_i}{\partial x_j^2} - \frac{\partial \overline{u_i' u_j'}}{\partial x_j}. \tag{E.2}$$

As it can be seen in Equation E.2, additional terms arise from this operation. They represent the transport of the fluctuations of the momentum and they are equivalent to stresses and they are so called Reynolds turbulent stresses. Since new unknowns appear in the problem, it is necessary to introduce new models in order to close the system and resolve the RANS. A common assumption is represented by the Boussinesq approximation which states that

$$\rho \overline{u_i' u_j'} = \frac{2}{3}\rho k \delta_{\mathrm{ij}} - \mu_t \left(\frac{\partial \bar{u}_i}{\partial x_j} + \frac{\partial \bar{u}_j}{\partial x_i} \right),$$

where μ_t is the turbulent viscosity. Turbulent models which employ the Boussinesq approximation are finalised to compute μ_t so that a relation between the physical properties of the system and the Reynolds stresses can be established. There are different available models, namely Spalart-Almaras (one-equation model), k-ε (two-equation model), k-ω (two-equation model). In the following paragraph, the k-ε model will be discussed.

E.2 k-ε model

The standard k-ε model employs two additional transport equations, respectively for the turbulent kinetic energy k and the turbulent dissipation rate ε, represented as follows

$$\frac{\partial k}{\partial t} + \bar{u}_j \frac{\partial k}{\partial x_j} = P + \frac{\partial}{\partial x_j}\left[\left(\nu + \frac{\nu_t}{\sigma_k} \right) \frac{\partial k}{\partial x_j} \right] - \varepsilon$$

$$\frac{\partial \varepsilon}{\partial t} + \bar{u}_j \frac{\partial \varepsilon}{\partial x_j} = \frac{\varepsilon}{k}\left(C_{\varepsilon 1} P - C_{\varepsilon 2} \varepsilon \right) + \frac{\partial}{\partial x_j}\left[\left(\nu + \frac{\nu_t}{\sigma_\varepsilon} \right) \frac{\partial \varepsilon}{\partial x_j} \right]$$

where P is related to the production of turbulent kinetic energy and defined as $2\nu_t \bar{S}_{\mathrm{ij}} \bar{S}_{\mathrm{ij}}$. The turbulent viscosity μ_t is computed as

$$\mu_t = \rho C_\mu \frac{k^2}{\varepsilon}.$$

The model constants have been tuned experimentally and they have the following values

$$C_\mu = 0.09, \quad \sigma_k = 1, \quad \sigma_\varepsilon = 1.3, \quad C_{\varepsilon 1} = 1.44, \quad C_{\varepsilon 2} = 1.92.$$

Two additional variants of this model are available, namely the RNG k-ε and the realisable k-ε models. The former has been chosen for the current research. The RNG alternative is found to

perform better with respect to the standard option for a wider class of flows [56]. The method is derived from the instantaneous Navier-Stokes equations, using a mathematical technique called "renormalisation group" (RNG) methods [56]. The main differences are related to the way the turbulent viscosity is calculated and to the presence of an extra term in the equations for ε which allows to cope with rapidly strained flows.

E.3 Near-wall treatment

Near-wall regions play an important role in wall-bounded turbulent flows. In fact, the presence of the wall influences both the kinematics of the mean flow through the no-slip condition and the level of turbulence because of the effects of viscosity. As a consequence, the flow properties in these regions are subjected to strong gradients which need to be resolved accurately in order to obtain reliable predictions of the solution. Generally, the near-wall region can be divided in three parts:

- the *viscous sublayer* corresponds to the most internal layer. It is characterised by a laminar-regime flow where viscosity plays an important role for the governing equations;
- the *log-law layer* represents the outermost layer. In this region, the flow is fully turbulent;
- the *buffer layer* is located between the two above extreme cases. In this region, neither turbulence nor viscosity is predominant but they are equally important.

The behaviour of the flow in these layers can be described in terms of two quantities: the dimensionless grid distance $y^+ = u_t y/\nu$ and the dimensionless velocity $u^+ = u/u_t$, where u_t is the friction velocity defined as $\sqrt{\tau_w/\rho}$. The linear relation $u^+ = y^+$ holds in the viscous sublayer as long as y^+ is smaller than 5. As the distance from the wall is greater than 30, the flow is described by a logarithmic law as follows

$$u^+ = \frac{1}{\kappa} \log y^+ + C$$

where κ and C are constant respectively equal to 0.41 and 5 for smooth walls. Moreover, the two previous laws intersect at the value $y^+ = 11$ in the buffer layer. However, none of the two is predominant over the other. In Figure E.1, the dimensionless velocity profile is shown as function of the aforementioned regions.

There are two ways to treat the near-wall region in Fluent. In the first method, the buffer layer and the viscous sublayer are not resolved. A set of semi-empirical formulae known as wall functions is introduced in order to connect the fully-turbulent region to the area near the wall which is affected by viscosity. The use of these equations avoids the need to modify and adapt the turbulent model. However, the drawback is that the solution might not be accurate for mesh refinements, especially when y^+ is below 15. Fluent offers different groups of wall functions. Standard Wall Functions are the default option and they are based on the work of Launder & Spalding [56]. The second method is named near-wall model because it resolves all the layers up to the wall. The Enhanced Wall Treatment falls within this category

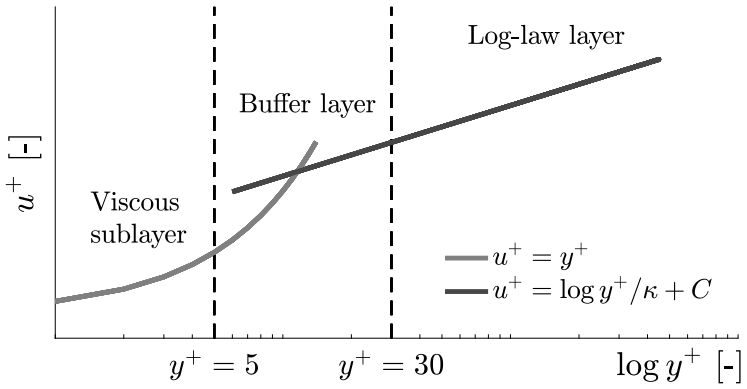

Figure E.1: Near-wall velocity profile u^+ as function of the dimensionless grid distance y^+. The different near-wall layers are indicated in the plot.

and it is the option selected for this thesis. This treatment blends the linear and logarithmic law of the wall through the following equation

$$u^+ = e^{\Gamma} u^+_{\text{lam}} + e^{1/\Gamma} u^+_{\text{turb}}, \tag{E.3}$$

where $\Gamma = \dfrac{a(y^+)^4}{1+by^+}$ with $a = 0.01$ and $b = 5$. This formula guarantees the perfect asymptotic behaviour for large and small values of y^+; in addition, it performs interpolation to yield a reasonable representation of the velocity profiles whenever y^+ is within the buffer region [56]. Qualitative y^+ contours have been reported in Figure E.3 for the five investigated time instants; instead, Figure E.2 shows a scatter plot for leaflet 1 as function of the y direction at flow peak.

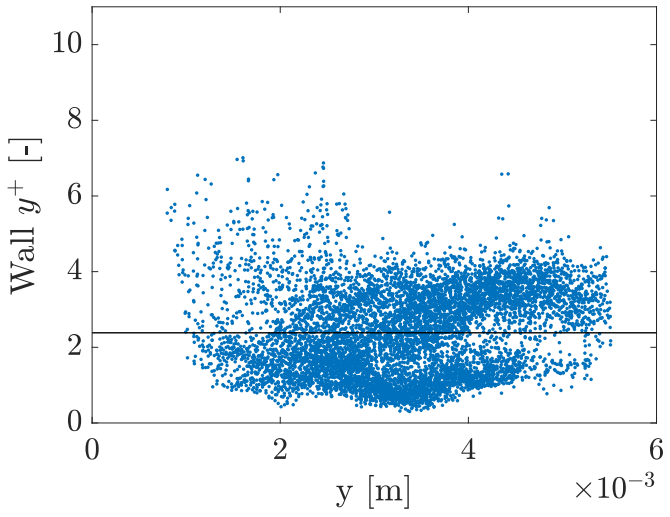

Figure E.2: Scatter plot of y^+ for leaflet 1 at flow peak. The line shows the mean value equal to 2.3.

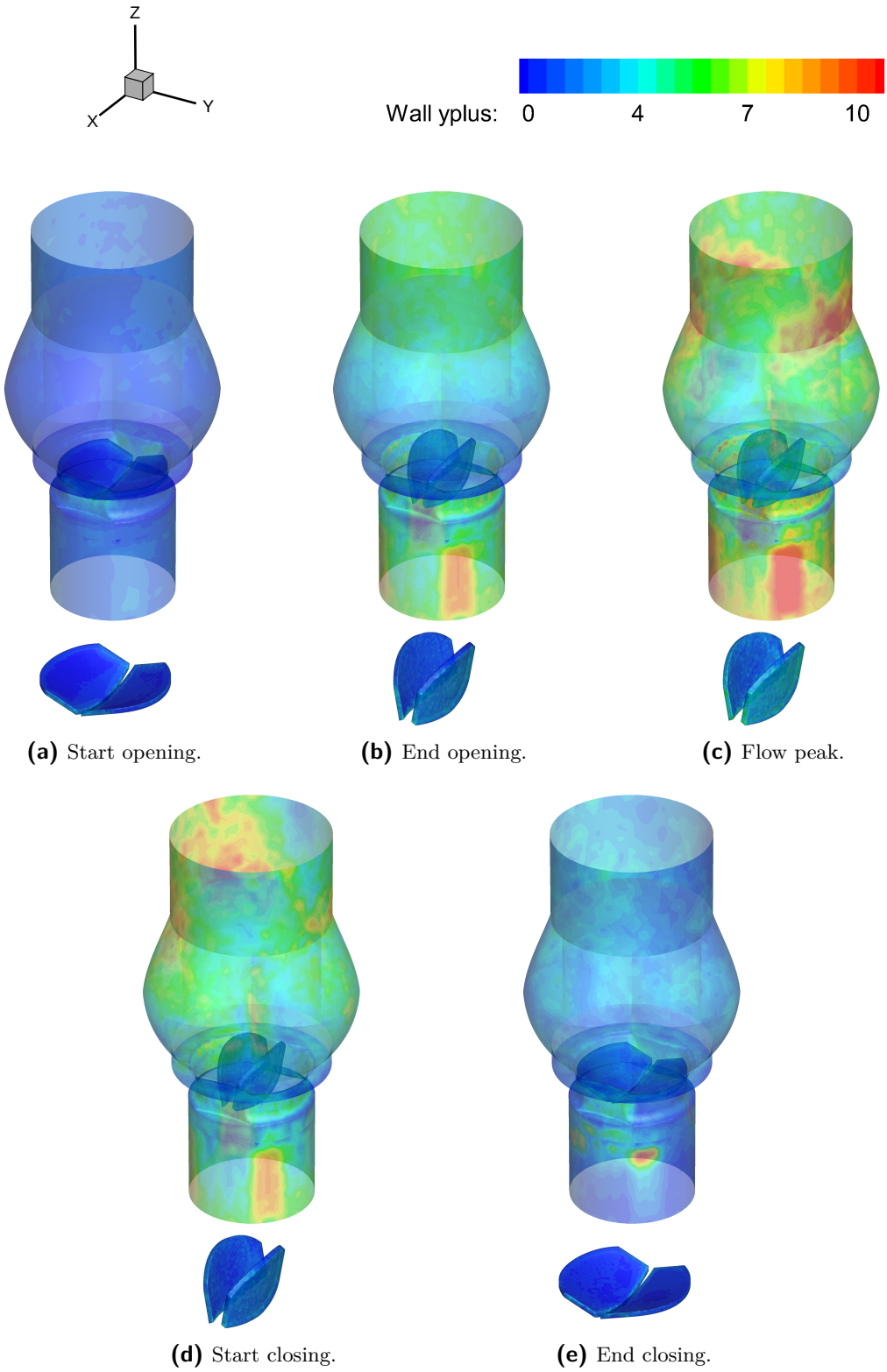

(a) Start opening. **(b)** End opening. **(c)** Flow peak.

(d) Start closing. **(e)** End closing.

Figure E.3: y^+ contours for the aortic root for five different instants in the flow.

E.4 Kolmogorov scale estimation

A further analysis on the turbulent characteristics of the flow regards the estimation of the dimensions of the smallest scales. This is done in order to gain a feeling for the numerical demand which is required to solve all the spectrum for this type of flow. In addition, it can also be used as a reference for future studies.

The smallest length scale η, also known as the Kolmogorov length scale, determines the size of the small eddies where dissipation of energy takes place because of viscosity. Mathematically, this is defined as

$$\eta = \left(\frac{\nu^3}{\varepsilon}\right)^{\frac{1}{4}} \tag{E.4}$$

where ν is the kinematic viscosity and ε is the turbulent dissipation rate. In order to have a first estimate of the value, Equation E.4 can be alternatively expressed in terms of Re and the characteristic length of the large eddies as

$$\eta = d\,\mathrm{Re}^{-3/4} \simeq 34.5\,\mu m.$$

The Kolmogorov length scale is an important parameter because it sets the minimum size of the grid cells if the smallest eddies are to be resolved in the simulations. Thus, the elements of the mesh which was used for the current research were analysed in order to assess how much they deviate from the minimum size. To obtain a reasonable approximation, Equation E.4 was solved by taking the dissipation rate from the RANS model. Then, the length ratio $\mathcal{L}/\eta$ was evaluated, where $\mathcal{L} = (\Delta V)^{\frac{1}{3}}$ is the characteristic length of the mesh cells. The results are reported in Figure E.4 for the five different instants of the flow.

The analysis of the contours highlights that the size of the mesh is bigger than the Kolmogorov length scale especially in the core region of the domain. Furthermore, this discrepancy is more pronounced at peak flow and at the beginning of the closing phase. This means that further refinement should be performed in order to be able to catch smaller scales. Nevertheless, there are some regions in the proximity of the leaflets and the housing where this ratio approaches one. Not surprisingly, these locations coincide with those where extra refinements were already accomplished.

Finally, it can be concluded that the mesh for the simulation carried out with laminar approach was not suitable for a proper DNS analysis because it would need additional refinements. Thus, the aid of a turbulent model allowed to cope with this limitation so to derive reasonable predictions on the main structures of the flow.

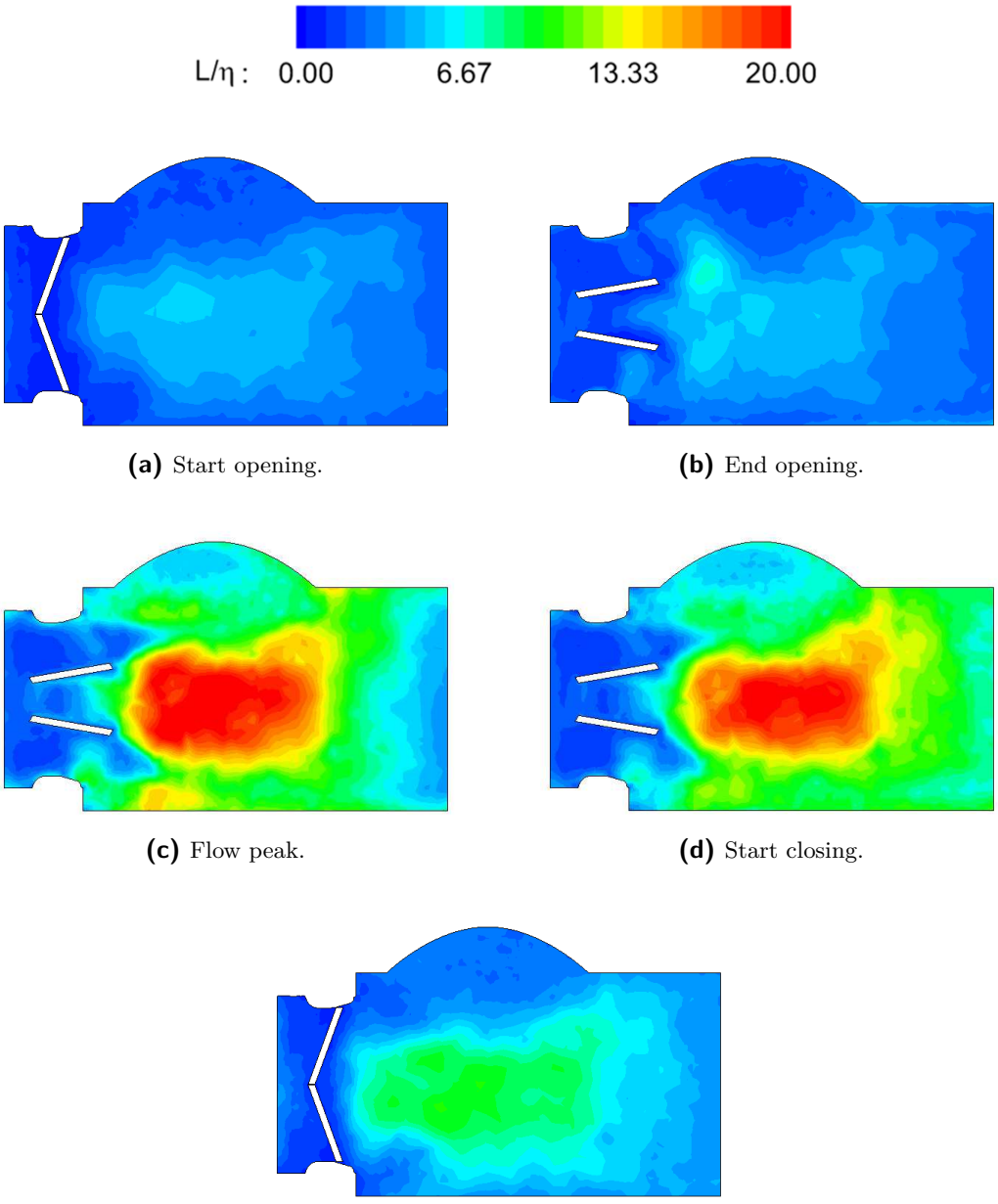

(a) Start opening.

(b) End opening.

(c) Flow peak.

(d) Start closing.

(e) End closing.

Figure E.4: Estimation of the ratio between the Kolmogorov scale and the characteristic cell size.

F
Codes

In this appendix, the UDFs used in the simulations will be presented.

F.1 Velocity inlet

F.1.1 Two-dimensional case

Code F.1: 2D pulsatile inlet profile.

```
#include "udf.h"
#define PI 3.141592654
#define h 0.02
#define u_mean 0.04
#define u_ampl 0.11
#define Tp 2.45
#define tau 2.45

DEFINE_PROFILE(Inlet_profile,thread,i)
{
  real u, current_time;
  face_t f; /*face identifier*/

  current_time = CURRENT_TIME;

  /*Loop on all faces belonging to the current thread*/
  begin_f_loop(f,thread)
  {
    double time = current_time/tau-floor(current_time/tau); //t is the local time within each period

    if (time >= 0 && time < 0.4/Tp)
    {
      u = u_mean + 0.5*u_ampl*sin(2*PI*((time*Tp+2.05)/Tp+0.26)/1.26);
      F_PROFILE(f,thread,i) = u;
    }
    if (time > 0.4/Tp && time < (0.37*Tp+0.4)/Tp)
    {
      u = u_mean + u_ampl*sin(2*PI*(time*Tp-0.4)/Tp/0.74);
      F_PROFILE(f,thread,i) = u;
    }
    if (time >= (0.37*Tp+0.4)/Tp && time < 1)
    {
    u =  u_mean + 0.5*u_ampl*sin(2*PI*((time*Tp-0.4)/Tp+0.26)/1.26);
    F_PROFILE(f,thread,i) = u;
    }
  }
  end_f_loop(f,thread);
}
```

F.1.2 Three-dimensional case

Code F.2: 3D pulsatile inlet profile.

```
#include "udf.h"
#define PI 3.141592654
#define tau 0.866

#define a0  0.151914481028658
#define a1  -0.145306785908299
#define a2  -0.122738065399385
#define a3  0.130835940279886
#define a4  -0.020444864298718
#define a5  0.026000343865393
#define a6  -0.017878348562487
#define a7  -0.007640774002263
#define a8  0.004748442443840
#define a9  -0.006466264705808
#define a10  0.005020011309145
#define a11  -0.000872977762983
#define a12  -0.000669296626788

#define b1  -0.249145432351456
#define b2  0.190973324706922
#define b3  0.015634681807180
#define b4  -0.033742186871017
#define b5  0.003471021918152
#define b6  -0.029558589692211
#define b7  0.017815655087999
#define b8  -0.006618483932442
#define b9  0.004389603403783
#define b10 0.001608315879452
#define b11  -0.002381655366404
#define b12 0.000824527759244

DEFINE_PROFILE(inlet_3D, thread, i)
{
  real u, t, t_tilda, t_bar;
  face_t f; /*face identifier*/
  t = CURRENT_TIME;

  begin_f_loop(f, thread)
  {
    t_tilda = tau*(t/tau-floor(t/tau));
    t_bar = 2*PI/tau*t_tilda-PI;

    u = a0 + a1*cos(t_bar) + b1*sin(t_bar) + a2*cos(2*t_bar) + b2*sin(2*t_bar) + a3*cos(3*t_bar) +
        b3*sin(3*t_bar) + a4*cos(4*t_bar) + b4*sin(4*t_bar) + a5*cos(5*t_bar) + b5*sin(5*t_bar) + a6
        *cos(6*t_bar) + b6*sin(6*t_bar) + a7*cos(7*t_bar) + b7*sin(7*t_bar) + a8*cos(8*t_bar) + b8*
        sin(8*t_bar) + a9*cos(9*t_bar) + b9*sin(9*t_bar) + a10*cos(10*t_bar) + b10*sin(10*t_bar) +
        a11*cos(11*t_bar) + b11*sin(11*t_bar) + a12*cos(12*t_bar) + b12*sin(12*t_bar);
    F_PROFILE(f, thread, i) = u;
  }
  end_f_loop(f, thread);
}
```

F.2 Leaflet motion

F.2.1 Two-dimensional case

Code F.3: 2D leaflet motion.

```
#include "udf.h"
#include <math.h>
#include <float.h>

float quadratic(a,b,c,time) {
return (a*time*time+b*time+c);
}

DEFINE_CG_MOTION(leaflet_1, dt, vel, omega, time, dtime)
{
  real omega_1, omega_2, omega_3, ang_vel;
  const float tau = 2.45;
  const float timefrac=time/tau-(int)(time/tau); /* time = (i-1+timefrac) * tau ;  time-(i-1)*tau =
      timefrac * tau  */
  float a,b,c;
  NV_S(vel, =, 0.0);
```

```
16    NV_S(omega, =, 0.0);
17    if (timefrac < 0.05) /*interval 1*/
18    {
19      a=-26.807120505489387; b=9.266727689156195; c=0.000783615629158;
20    } else if (timefrac < 0.1) /*interval 2*/
21    {
22      a=26.143008222835348; b=3.706053849283352; c=0.795366484858580;
23    } else if (timefrac < 0.15) /*interval 3*/
24    {
25      a=-62.227840037379096; b=39.595661798221720; c=-4.509093681960790;
26    } else if (timefrac < 0.2)
27    {
28      a=22.014041773849364; b=-22.322121333031205; c=6.868298968406935;
29    } else if (timefrac < 0.25)
30    {
31      a=61.537085350967729; b=-61.054704038607206; c=16.357781731273054;
32    } else if (timefrac < 0.3)
33    {
34      a=-140.6306707877134; b=186.6007972312772; c=-59.4867155326291;
35    } else if (timefrac < 0.35)
36    {
37      a=64.4809667496437; b=-114.9133099486378; c=51.3197188559897;
38    } else if (timefrac < 0.4)
39    {
40      a=16.952600460845829; b=-33.402161763349390; c=16.371814071547309;
41    } else if (timefrac < 0.45)
42    {
43      a=-18.353027926247968; b=35.796869875354453; c=-17.535711431417571;
44    } else if (timefrac < 0.5)
45      a=1.873538907743977; b=-8.802709993597796; c=7.049806971342358;
46    } else if (timefrac < 0.55)
47    {
48      a=29.747005290877198; b=-77.092702632274197; c=48.877427462531664;
49    } else if (timefrac < 0.65)
50    {
51      a=-6.682622822327147; b=21.085145132811512; c=-17.269897469194834;
52    } else if (timefrac < 0.7)
53    {
54      a=-4.841648539176466; b=15.221642040976592; c=-12.601083132321280;
55    } else if (timefrac < 0.75)
56    {
57      a=-1.453888636656024; b=3.601625575331484; c=-2.636919013030608;
58    } else if (timefrac < 0.85)
59    {
60      a=5.771080376282004; b=-22.950135547215780; c=21.757511518309698;
61    } else if (timefrac < 0.95)
62    {
63      a=1.205836496414086; b=-3.935894787565893; c=1.958933327324252;
64    } else if (timefrac < 1)
65    {
66      a=30.9773615736470; b=-142.5223440220852; c=163.2389136239961;
67    }
68    omega_1 =  quadratic(a,b,c,timefrac*tau);
69    omega_2 =  quadratic(a,b,c,timefrac*tau+dtime);
70    omega_3 =  quadratic(a,b,c,timefrac*tau+dtime/2);
71    omega[0] = (omega_1+omega_2+4*omega_3)/6;
72  }
```

F.2.2 Three-dimensional case

Code F.4: Motion of Leaflet 1.

```
1   #include "udf.h"
2   #include <math.h>
3   #include <float.h>
4   #include "dynamesh_tools.h"
5
6   float quadratic(a,b,c,time) {
7   return (a*time*time+b*time+c);
8   }
9
10  DEFINE_CG_MOTION(leaflet_1, dt, vel, omega, time, dtime)
11  {
12    real omega_1, omega_2, omega_3, ang_vel;
13    const float tau = 0.866;
14    const float timefrac=time/tau-floor(time/tau); /* time = (i-1+timefrac) * tau ;  time-(i-1)*tau =
          timefrac * tau  */
15    float a,b,c;
16
17    NV_S(vel, =, 0.0);
18    NV_S(omega, =, 0.0);
19
20    if (timefrac < 0.005773672055427) /*interval 1*/
21    {
```

```
22        a=2159.567580764660; b=-2.407990408052271; c=-0.011976420486241;
23      }   else if (timefrac < 0.011547344110855) /*interval 2*/
24      {
25        a=-9353.043658991941; b=112.7181219895138; c=-0.299791701480157;
26      }   else if (timefrac < 0.017321016166282) /*interval 3*/
27      {
28        a=35252.60705520311; b=-779.3948922943873; c=4.160773369939347;
29      }   else if (timefrac < 0.023094688221709) /*interval 4*/
30      {
31        a = -131657.3845618204; b=4227.904856216317; c=-33.393974743890929;
32      }   else if (timefrac < 0.024868233256351) /*interval 5*/
33      {
34        a=2920261.616349375; b=-117848.8551802315; c=1187.373625620587;
35      }   else if (timefrac < 0.037302355658199) /*interval 6*/
36      {
37        a=-365233.9921034529; b=23663.28885801484; c=-336.4213582153271;
38      }   else if (timefrac < 0.046555658198614)   /*interval 7*/
39      {
40        a = -162416.5824265572; b = 10559.72655518106; c = -124.7736681849403;
41      }   else if (timefrac < 0.084147170900693)  /*interval 8*/
42      {
43        a = 42576.16211265033; b = -5969.740405091208; c=208.4372444804041;
44      }   else if (timefrac < 0.092378752886836) /*interval 9*/
45      {
46        a = -20234.20914190231; b = 3184.425251623931; c = -125.1014179921131;
47      }  else if (timefrac < 0.103926096997691) /*interval 10*/
48      {
49        a = 3347.322773267875; b = -588.6198548032982; c=25.820386264976047;
50      }  else if (timefrac < 0.115473441108545) /*interval 11*/
51      {
52        a = -822.1505422079276; b=161.8853419823463; c=-7.952347590377953;
53      }  else if (timefrac < 0.138568129330254) /*interval 12*/
54      {
55        a = 80.748591112431384; b=-18.694484681725509; c = 1.076643742825639;
56      } else if (timefrac < 0.161662817551963) /*interval 13*/
57      {
58        a = -22.027986676271947; b = 5.971893987563289; c=-0.403338977331689;
59      } else if (timefrac < 0.184757505773672) /*interval 14*/
60      {
61        a = 7.363355592656569; b = -2.257681847736697; c = 0.172731331139310;
62      } else if (timefrac < 0.207852193995381) /*interval 15*/
63      {
64        a = -7.425435694354287; b = 2.474731364106778; c =-0.205861725808168;
65      } else if (timefrac < 0.230946882217090) /*interval 16*/
66      {
67        a = 22.338387184760542; b = -8.240244872374561; c = 0.758486135475152;
68      } else if (timefrac < 0.254041570438799) /*interval 17*/
69      {
70        a = -81.928113044688018; b = 33.466355219404868; c = -3.412173873702791;
71      } else if (timefrac < 0.277136258660508) /*interval 18*/
72      {
73        a =  305.3740649939915; b =-136.9466031176141; c=15.333251543369297;
74      } else if (timefrac < 0.281936408775982) /*interval 19*/
75      {
76        a= -13130.97063516483; b= 6312.498852958620; c =-758.6002031857787;
77      } else if (timefrac < 0.310852956120092) /*interval 20*/
78      {
79        a= 2228.830690351691; b=-1187.905021137469; c=157.0375886439250;
80      } else if (timefrac < 0.332829538106236) /*interval 21*/
81      {
82        a = -6155.874070173570; b= 3326.397550920574; c=-450.5845129723644;
83      } else if (timefrac < 0.355384457274827) /*interval 22*/
84      {
85        a =-14393.66072449542; b=8075.158306388804; c=-1134.953071511212;
86      } else if (timefrac < 0.362613591224018) /*interval 23*/
87      {
88        a = -639757.5318874783; b = 393002.8054241905; c = -60368.18525363982;
89      } else if (timefrac < 0.369553568129330) /*interval 24*/
90      {
91        a = 950770.4401230697; b = -605923.1022758455; c =96474.85470449734;
92      } else if (timefrac < 0.380252690531178) /*interval 25*/
93      {
94        a =  405707.0600396792; b = -257046.1396899536; c =40648.71618986424;
95      } else if (timefrac < 0.381062355658199) /*interval 26*/
96      {
97        a = -7508412.242555561; b =4955174.313960103; c = -817540.3323546525;
98      } else if (timefrac < 0.392609699769053) /*interval 27*/
99      {
100       a=23723.78254569855; b=-16035.46260672731; c=2709.280778874747;
101     } else if (timefrac < 0.404157043879908) /*interval 28*/
102     {
103       a = -5289.074758614119; b = 3693.280360205310; c = -644.6055255037981;
104     } else if (timefrac < 0.461893764434180) /*interval 29*/
105     {
106       a = 115.0279593400804; b=-89.591542362629752; c=17.397057445591507;
107     } else if (timefrac < 0.519630484988453) /*interval 30*/
108     {
109       a = -30.821547225992603; b= 27.088062890228635; c=-5.938863604980173;
110     } else if (timefrac < 0.577367205542725) /*interval 31*/
111     {
```

```
112       a = 8.258229563890023; b = -8.083736220665731; c = 1.9747911949710 59;
113     } else if (timefrac < 0.635103926096998) /*interval 32*/
114     {
115       a = -2.211371029567491; b = 2.385864372791783; c= -0.642608953393320;
116     }
117     else if (timefrac < 0.692840646651270) /*interval 33*/
118     {
119       a = 0.587254554379956; b= -0.692623769550409; c =0.203975285750783;
120     } else if (timefrac < 0.750577367205543) /*interval 34*/
121     {
122       a =  -0.137647187952325; b = 0.177258321248328; c= -0.056989341488838;
123     } else if (timefrac < 0.808314087759815) /*interval 35*/
124     {
125       a = -0.036665802570653; b =  0.045982520252154; c =-0.014324706165081;
126     } else if (timefrac < 0.866050808314088) /*interval 36*/
127     {
128       a =  0.284310398234938; b= -0.403384160875673; c =0.142953632229658;
129     } else if (timefrac < 0.923787528868360) /*interval 37*/
130     {
131       a = -1.100575790369095; b= 1.673945122030377; c= -0.636044848860111;
132     } else if (timefrac < 0.981524249422633) /*interval 38*/
133     {
134       a = 4.117992763241454; b =-6.675764563746503; c =2.703839025450642;
135       } else if (timefrac <1) /*interval 39*/
136     {
137       a = -85.400423181754974; b=145.5055425427474; c= -61.973216494809272;
138     }
139
140     omega_1 =  quadratic(a,b,c,timefrac*tau);
141     omega_2 =  quadratic(a,b,c,timefrac*tau+dtime);
142     omega_3 =  quadratic(a,b,c,timefrac*tau+dtime/2);
143     omega[0] = (omega_1+omega_2+4*omega_3)/6;
144   }
```

Code F.5: Motion of Leaflet 2.

```
1   #include "udf.h"
2   #include <math.h>
3   #include <float.h>
4   #include "dynamesh_tools.h"
5
6   float quadratic(a,b,c,time) {
7   return (a*time*time+b*time+c);
8   }
9
10  DEFINE_CG_MOTION(leaflet_1, dt, vel, omega, time, dtime)
11  {
12    real omega_1, omega_2, omega_3, ang_vel;
13    const float tau = 0.866;
14    const float timefrac=time/tau-floor(time/tau); /* time = (i-1+timefrac) * tau ;  time-(i-1)*tau =
          timefrac * tau  */
15    float a,b,c;
16
17    NV_S(vel, =, 0.0);
18    NV_S(omega, =, 0.0);
19
20    if (timefrac < 0.005773672055427) /*interval 1*/
21    {
22      a=-875.8464325456546; b=0.295292037672549; c=0.006560490177032;
23    }   else if (timefrac < 0.011547344110855) /*interval 2*/
24    {
25      a=4202.056940124745; b=-50.483741689031447; c=0.133508074493792;
26    }   else if (timefrac < 0.017321016166282) /*interval 3*/
27    {
28      a=-15932.38132795332; b=352.2050236725299; c=-1.879935752314014;
29    }   else if (timefrac < 0.023094688221709) /*interval 4*/
30    {
31      a = 59527.46837168851; b=-1911.590467316725; c=15.098530430105395;
32    }   else if (timefrac < 0.024579076212471) /*interval 5*/
33    {
34      a=-1778223.139322904; b=71598.43384046695; c=-720.0017126477314;
35    }   else if (timefrac < 0.052516166281755) /*interval 6*/
36    {
37      a=114860.7112041767; b=-8991.963036967351; c=137.7009278156138;
38    }   else if (timefrac < 0.073448048498845)   /*interval 7*/
39    {
40      a = 11357.07634147828; b = 422.52058287397 15; c = -76.379722457767997;
41    }   else if (timefrac < 0.080831408775982)  /*interval 8*/
42    {
43      a = -177022.0556438293; b = 24386.61048857155; c=-838.5097935491177;
44    }   else if (timefrac < 0.092378752886836) /*interval 9*/
45    {
46      a = 25125.55535085136; b = -3914.055050683734; c = 152.0135003248174;
47    }  else if (timefrac < 0.103926096997691) /*interval 10*/
48    {
49      a = -6684.586284893617; b = 1175.567611035462; c=-51.571406143950426;
50    }  else if (timefrac < 0.115473441108545) /*interval 11*/
51    {
```

```
52      a = 1612.789788723116; b=-317.9600822155500; c=15.637340052345099;
53    }  else if (timefrac < 0.138568129330254) /*interval 12*/
54    {
55      a = -114.0635498399625; b=27.410585497065767; c = -1.631193333285689;
56    } else if (timefrac < 0.173210161662818) /*interval 13*/
57    {
58      a = -53.639372329547143; b = 12.908782894566080; c=-0.761085177135708;
59    } else if (timefrac < 0.207852193995381) /*interval 14*/
60    {
61      a = 264.6635081002591; b = -82.582081234375792; c = 6.400729632534933;
62    } else if (timefrac < 0.242494226327945) /*interval 15*/
63    {
64      a = -1005.014660071489; b = 374.5020593074536; c =-34.736843016229713;
65    } else if (timefrac < 0.273839769053118) /*interval 16*/
66    {
67      a = 4310.168459180391; b = -1857.874850778336; c = 199.6627325427781;
68    } else if (timefrac < 0.320684584295612) /*interval 17*/
69    {
70      a = 6095.541535326831; b = -2704.660304042907; c = 300.0683023142460;
71    } else if (timefrac < 0.338323683602771) /*interval 18*/
72    {
73      a =  -17593.27281025357; b =10452.71598602113; c=-1526.917931703810;
74    } else if (timefrac < 0.359143602771363) /*interval 19*/
75    {
76      a= -67494.95781298065; b= 39693.93669622384; c =-5810.585850813456;
77    } else if (timefrac < 0.369515011547344) /*interval 20*/
78    {
79      a= 159136.7913985799; b=-101279.3332311979; c=16112.05175751855;
80    } else if (timefrac < 0.381062355658199) /*interval 21*/
81    {
82      a = -33408.87207849664; b=21949.89139413112; c=-3604.624182534087;
83    } else if (timefrac < 0.404157043879908) /*interval 22*/
84    {
85      a =2893.751969000316; b=-2009.840477216871; c=348.7315762383329;
86    } else if (timefrac < 0.461893764434180) /*interval 23*/
87    {
88      a = -200.0075304606758; b = 155.7911724058237; c = -30.253962445638713;
89    } else if (timefrac < 0.519630484988453) /*interval 24*/
90    {
91      a = 52.883587302339961; b = -46.521721804588900; c =10.208616396443807;
92    } else if (timefrac < 0.577367205542725) /*interval 25*/
93    {
94      a =  -11.526818748684136; b = 11.447643641332791; c =-2.834490828888575;
95    } else if (timefrac < 0.923787528868360) /*interval 26*/
96    {
97      a = 0.141665383197176; b =-0.220840490548522; c = 0.082630204081753;
98    } else if (timefrac < 1) /*interval 27*/
99    {
100     a=2.192938750799924; b=-3.502877878712918; c=1.395445159347512;
101   }
102
103   omega_1 =  quadratic(a,b,c,timefrac*tau);
104   omega_2 =  quadratic(a,b,c,timefrac*tau+dtime);
105   omega_3 =  quadratic(a,b,c,timefrac*tau+dtime/2);
106   omega[0] = (omega_1+omega_2+4*omega_3)/6;
107 }
```

G

Part of this work has been presented at the 12th International Symposium on Biomechanics in Vascular Biology and Cardiovascular Disease in Rotterdam on 4 and 5 April 2017. Hereby, the submitted abstract and the informative poster will be presented.

Verification of aortic valve's leaflet motion using CFD and FSI methods

Edoardo Antonini[1], G. Fagioli[2], S. S. Khalafvand[2], S. Kenjeres[2]

[1]Department of Mechanical Engineering, Faculty of Civil and Industrial Engineering, La Sapienza University of Rome, Italy

[2]Department of Chemical Engineering, Faculty of Applied Sciences, Delft University of Technology, The Netherlands

Introduction

Valvular heart diseases represent a category of pathologies which affect heart valves. The present research is aimed to reproduce the behaviour of a patient-specific heart valve. This study shows an intermediate step to validate two different numerical approaches with experimental results of Stijnen *et al*. [1]. Therefore, the behaviour of blood patterns in the aortic root is investigated.

Methods

The Arbitrary Lagrangian-Eulerian (ALE) method along with remeshing techniques was employed to perform numerical simulations using ANSYS Fluent. The geometry was constructed to mimic the experimental setup. Two different approaches were used to investigate the opening and closing motion of the leaflet: two-way fluid-structure interaction (FSI) and prescribed rigid motion of the leaflet. In addition, analysis of the resulting hemodynamics was also performed.

Results

The results are shown for the instant when the inlet velocity reaches its mean value during deceleration. At this instant, leaflet has already started the closing phase. Velocity profiles and velocity contours are compared; the flow patterns highlight the formation of a counterclockwise vortex in the aortic sinus.

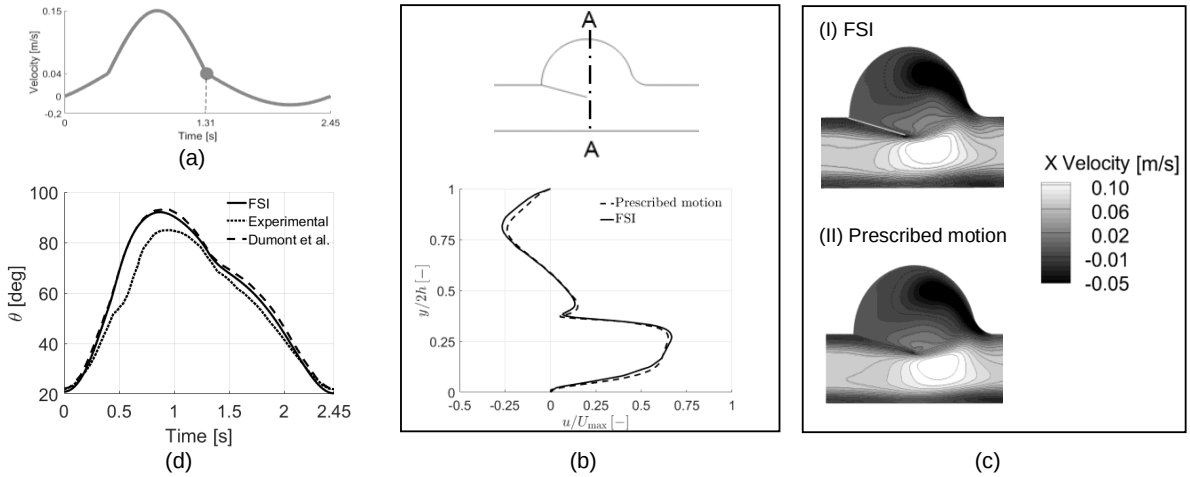

Figure 1. (a) Pulsatile inlet velocity profile; (b) Sketch of the geometry with velocity profile comparison in section A-A; (c) velocity contours comparison; (d) leaflet opening angle.

Conclusions

The results show that the two numerical approaches are in good agreement. Moreover, the opening angle from our FSI reflects the same trend of experimental data and the FSI investigation of Dumont *et al.* [2].

References

[1] J. Stijnen, J. de Hart, P. Bovendeerd, and F. van de Vosse, "Evaluation of a fictitious domain method for predicting dynamic response of mechanical heart valves," *Journal of Fluids and Structures*, vol. 19, 835–850, 2004.

[2] K. Dumont, J. M. a. Stijnen, J. Vierendeels, F. N. van de Vosse, and P. R. Verdonck., "Validation of a fluid-structure interaction model of a heart valve using the dynamic mesh method in fluent.", Computer methods in biomechanics and biomedical engineering, vol. 7, no. 3, pp. 139–146, 2004.

Verification of aortic valve leaflet motion using CFD and FSI methods

E. Antonini[1], G. Fagioli[2], S. S. Khalafvand[2], S. Kenjeres[2]

[1]Department of Mechanical Engineering, Faculty of Civil and Industrial Engineering, La Sapienza University of Rome, Italy
[2]Department of Chemical Engineering, Faculty of Applied Sciences, Delft University of Technology, The Netherlands

1 Introduction

Valvular heart diseases represent a category of pathologies which affect heart valves. The present research is aimed to reproduce the behaviour of a patient-specific heart valve. This study shows an intermediate step to validate two different numerical approaches with experimental results of Stijnen *et al.* [1]. Therefore, the behaviour of blood patterns in the aortic root is investigated.

Figure 1. Experimental setup from TU/e (Stijnen et al., 2004).

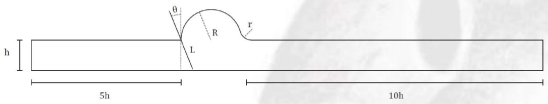

Figure 2. Geometric 2D sketch of the computational domain.

2 Methods

The Arbitrary Lagrangian-Eulerian (ALE) method along with remeshing techniques was employed to perform numerical simulations using ANSYS Fluent. Two different approaches were used to investigate the opening and closing motion of the leaflet: two-way Fluid-Structure Interaction (FSI) and prescribed rigid motion of the leaflet.

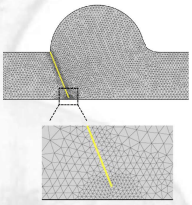

Figure 3. Mesh of the fluid domain.

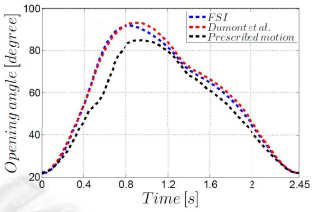

Figure 4. Validation and comparison of the leaflet opening angle.

3 Results

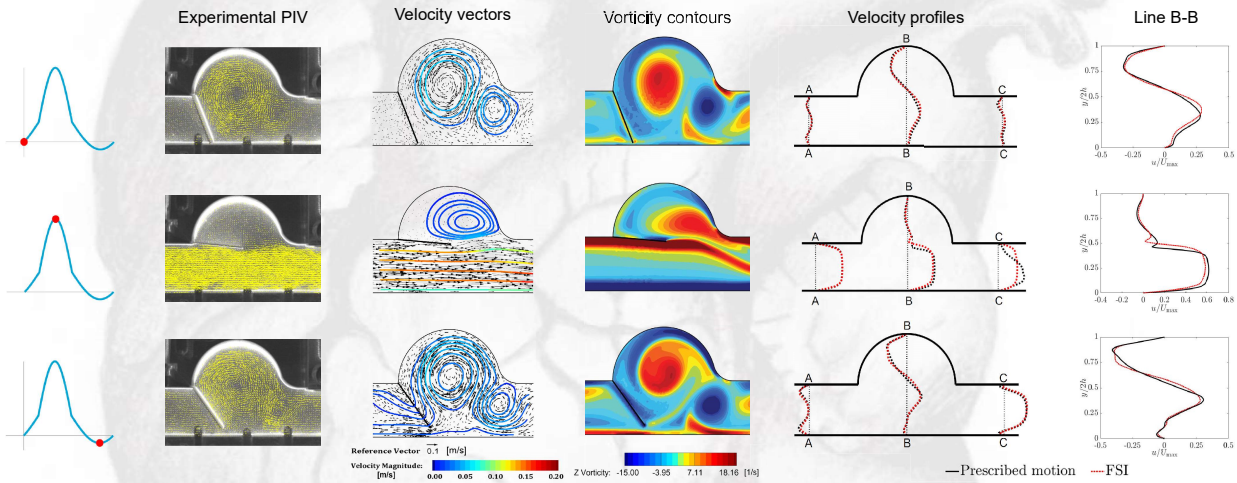

4 Extension to 3D

The approach of prescribed motion is applied to a three-dimensional model with a mechanical bileaflet valve. The results are validated with the experimental work of Cerroni and Romano and with the FSI simulation of De Tullio *et al.* [3].

Figure 5. Sketch of the geometry and mesh of the computational domain at x = 0.

Figure 6. Aortic root and the mechanical valve in open configuration.

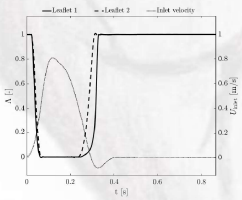

Figure 7. Opening angle and inlet profile as function of time.

5 3D preliminary results

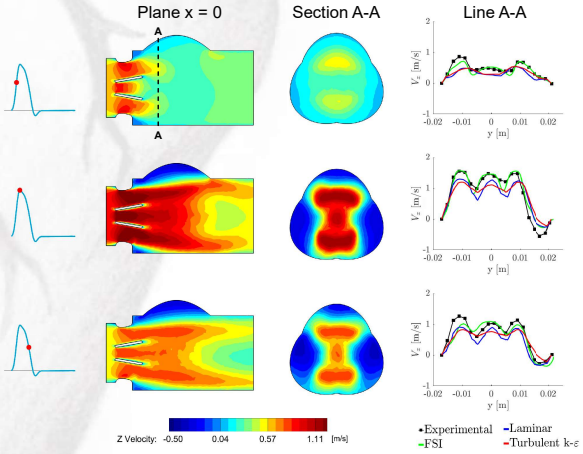

References

[1] J. Stijnen, J. de Hart, P. Bovendeerd, and F. van de Vosse, "Evaluation of a fictitious domain method for predicting dynamic response of mechanical heart valves", Journal of Fluids and Structures, vol. 19, 835–850, 2004.
[2] K. Dumont, J. M. A. Stijnen, J. Vierendeels, F. N. van de Vosse, and P. R. Verdonck, "Validation of a fluid-structure interaction model of a heart valve sing the dynamic mesh method in fluent.", Computer methods in biomechanics and biomedical engineering, vol. 7, no. 3, pp. 139–146, 2004.
[3] M. D. De Tullio, A. Cristallo, E. Balaras, and R. Verzicco, "Direct numerical simulation of the pulsatile flow through an aortic bileaflet mechanical heart valve", Journal of Fluid Mechanics, vol. 622, p. 259, 2009.

Contact Information
Edoardo Antonini: E.Antonini@tudelft.nl
Giorgio Fagioli: G.Fagioli@student.tudelft.nl
S. Kenjeres: S.Kenjeres@tudelft.nl
S. S. Khalafvand: S.S.Khalafvand@tudelft.nl

SAPIENZA UNIVERSITÀ DI ROMA
TU Delft

Bibliography

[1] S. Mendis, P. Puska, and B. Norrving, "Global atlas on cardiovascular disease prevention and control", *World Health Organization*, pp. 2–14, 2011.

[2] World Health Organization, "Global action plan for the prevention and control of noncommunicable diseases 2013-2020", *World Health Organization*, p. 102, 2013.

[3] B. Iung and A. Vahanian, "Epidemiology of valvular heart disease in the adult", *Nature Reviews Cardiology*, vol. 8, pp. 162–172, mar 2011.

[4] MedlinePlus - Normal heart anatomy (cut section), https://medlineplus.gov/ency/imagepages/8672.htm.

[5] J. P. Sutton, S. Y. Ho, and R. H. Anderson, "The forgotten interleaflet triangles: A review of the surgical anatomy of the aortic valve", *The Annals of Thoracic Surgery*, vol. 59, no. 2, pp. 419–427, 1995.

[6] M. Thubrikar, S. P. Nolan, L. Bosher, and J. Deck, "The cyclic changes and structure of the base of the aortic valve", *American Heart Journal*, vol. 99, pp. 217–224, feb 1980.

[7] Cardiac cycle - from *Wikipedia*, https://en.wikipedia.org/wiki/Cardiac_cycle.

[8] L. P. Dasi, H. A. Simon, P. Sucosky, and A. P. Yoganathan, "Fluid mechanics of artificial heart valves", 2009.

[9] medGadget - SJM Masters HP Series, https://www.medgadget.com/2015/02/sjm-masters-hp-series-worlds-smallest-pediatric-heart-valve-going-on-\trial-in-u-s.html.

[10] Sorin Group - Aortic Valve Products - Mitroflow with PRT http://www.livanova.sorin.com/products/cardiac-surgery/aortic

[11] K. Dumont, J. M. a. Stijnen, J. Vierendeels, F. N. van de Vosse, and P. R. Verdonck, "Validation of a fluid-structure interaction model of a heart valve using the dynamic mesh method in fluent.", *Computer methods in biomechanics and biomedical engineering*, vol. 7, no. 3, pp. 139–146, 2004.

[12] J. Stijnen, J. de Hart, P. Bovendeerd, and F. van de Vosse, "Evaluation of a fictitious domain method for predicting dynamic response of mechanical heart valves", *Journal of Fluids and Structures*, vol. 19, pp. 835–850, jul 2004.

[13] G. Cerroni, *Studio sperimentale del campo fluidodinamico a valle di una valvola cardiaca artificiale e in un dispositivo di circolazione assistita mediante tecnica PIV*. MSc thesis, Università degli studi di Roma La Sapienza, 2006.

[14] M. D. De Tullio, a. Cristallo, E. Balaras, and R. Verzicco, "Direct numerical simulation of the pulsatile flow through an aortic bileaflet mechanical heart valve", *Journal of Fluid Mechanics*, vol. 622, p. 259, 2009.

[15] F. Robicsek, "Leonardo da Vinci and the sinuses of Valsalva", *The Annals of Thoracic Surgery*, vol. 52, no. 2, pp. 328–335, 1991.

[16] M. Thubrikar, R. Harry, and S. P. Nolan, "Normal aortic valve function in dogs", *The American Journal of Cardiology*, vol. 40, no. 4, pp. 563–568, 1977.

[17] P. Dagum, G. R. Green, F. J. Nistal, G. T. Daughters, T. a. Timek, L. E. Foppiano, a. F. Bolger, N. B. Ingels, and D. C. Miller, "Deformational dynamics of the aortic root: modes and physiologic determinants.", *Circulation*, vol. 100, no. 19 Suppl, pp. II54–I62, 1999.

[18] E. Lansac, H. S. Lim, Y. Shomura, K. H. Lim, N. T. Rice, W. Goetz, C. Acar, and C. M. G. Duran, "A four-dimensional study of the aortic root dynamics", *European Journal of Cardio-thoracic Surgery*, vol. 22, no. 4, pp. 497–503, 2002.

[19] R. Gramiak and P. M. Shah, "Echocardiography of the aortic root.", *Investigative radiology*, vol. 3, no. 5, pp. 356–66.

[20] M. Handke, G. Heinrichs, F. Beyersdorf, M. Olschewski, C. Bode, and A. Geibel, "In vivo analysis of aortic valve dynamics by transesophageal 3-dimensional echocardiography with high temporal resolution", *Journal of Thoracic and Cardiovascular Surgery*, vol. 125, no. 6, pp. 1412–1419, 2003.

[21] M. Thubrikar, W. C. Piepgrass, T. W. Shaner, and S. P. Nolan, "The design of the normal aortic valve.", *The American journal of physiology*, vol. 241, no. 6, pp. H795–H801, 1981.

[22] D. Berdajs, P. Lajos, and M. Turina, "The anatomy of the aortic root", *Cardiovascular Surgery*, vol. 10, no. 4, pp. 320–327, 2002.

[23] W. SWANSON and R. E. CLARK, "Dimensions and Geometric Relationships of the Human Aortic Value as a Function of Pressure", *Circulation Research*, vol. 35, no. 6, pp. 871–882, 1974.

[24] M. R. Labrosse, C. J. Beller, F. Robicsek, and M. J. Thubrikar, "Geometric modeling of functional trileaflet aortic valves: Development and clinical applications", *Journal of Biomechanics*, vol. 39, no. 14, pp. 2665–2672, 2006.

[25] B. J. Bellhouse and L. Talbot, "Fluid mechanics of the aortic valve.", *J. Fluid Mech.*, vol. 35, no. 4, pp. 721–735, 1969.

[26] A. A. Van Steenhoven, M. E. H. Van Dongen, and M. E. H. Van Steenhoven A. A.; Van Dongen, "Model studies of the closing behaviour of the aortic val", *J. Fluid. Mech.*, vol. 90, pp. 21–32, 1979.

[27] C. S. Peskin, "The Fluid Dynamics of Heart Valves: Experimental, Theoretical, and Computational Methods", *Annual Review of Fluid Mechanics*, vol. 14, pp. 235–259, jan 1982.

[28] R. Mittal and G. Iaccarino, "Immersed Boundary Methods", *Annual Review of Fluid Mechanics*, vol. 37, no. 1, pp. 239–261, 2005.

[29] E. Fadlun, R. Verzicco, P. Orlandi, and J. Mohd-Yusof, "Combined immersed-boundary finite-difference methods for three-dimensional complex flow simulations", *Journal of Computational Physics*, vol. 161, no. 1, pp. 35–60, 2000.

[30] A. Cristallo and R. Verzicco, "Combined Immersed Boundary/Large-Eddy-Simulations of Incompressible Three Dimensional Complex Flows", *Flow, Turbulence and Combustion*, vol. 77, no. 1-4, pp. 3–26, 2006.

[31] M. D. de Tullio, L. Afferrante, G. Demelio, G. Pascazio, and R. Verzicco, "Fluid-structure interaction of deformable aortic prostheses with a bileaflet mechanical valve", *Journal of Biomechanics*, vol. 44, no. 9, pp. 1684–1690, 2011.

[32] R. Glowinski, T.-W. Pan, and J. Periaux, "A fictitious domain method for Dirichlet problem and applications", *Computer Methods in Applied Mechanics and Engineering*, vol. 111, no. 3, pp. 283–303, 1994.

[33] J. De Hart, G. W. M. Peters, P. J. G. Schreurs, and F. P. T. Baaijens, "A two-dimensional fluid-structure interaction model of the aortic value", *Journal of Biomechanics*, vol. 33, no. 9, pp. 1079–1088, 2000.

[34] J. De Hart, G. W. M. Peters, P. J. G. Schreurs, and F. P. T. Baaijens, "A three-dimensional computational analysis of fluid-structure interaction in the aortic valve", *Journal of Biomechanics*, vol. 36, pp. 103–112, jan 2003.

[35] A. Gilmanov and F. Sotiropoulos, "A hybrid Cartesian/immersed boundary method for simulating flows with 3D, geometrically complex, moving bodies", *Journal of Computational Physics*, vol. 207, pp. 457–492, 2005.

[36] I. Borazjani, L. Ge, and F. Sotiropoulos, "Curvilinear Immersed Boundary Method for Simulating Fluid Structure Interaction with Complex 3D Rigid Bodies.", *Journal of computational physics*, vol. 227, pp. 7587–7620, aug 2008.

[37] I. Borazjani, L. Ge, and F. Sotiropoulos, "High-resolution fluid-structure interaction simulations of flow through a bi-leaflet mechanical heart valve in an anatomic aorta.", *Annals of biomedical engineering*, vol. 38, pp. 326–44, feb 2010.

[38] L. Ge and F. Sotiropoulos, "A Numerical Method for Solving the 3D Unsteady Incompressible Navier-Stokes Equations in Curvilinear Domains with Complex Immersed Boundaries.", *Journal of computational physics*, vol. 225, pp. 1782–1809, aug 2007.

[39] L. P. DasiL GeH A SimonF SotiropoulosA P Yoganathan, L. P. Dasi, L. Ge, H. A. Simon, F. Sotiropoulos, and A. P. Yoganathan, "Vorticity dynamics of a bileaflet mechanical heart valve in an axisymmetric aorta", *Citation: Phys. Fluids*, vol. 19, 2007.

[40] L. Ge and F. Sotiropoulos, "Direction and Magnitude of Blood Flow Shear Stresses on the Leaflets of Aortic Valves: Is There a Link With Valve Calcification?", *Journal of Biomechanical Engineering*, vol. 132, no. 1, p. 014505, 2010.

[41] P. D. Thomas and C. K. Lombard, "Geometric Conservation Law and Its Application to Flow Computations on Moving Grids", *AIAA Journal*, vol. 17, pp. 1030–1037, oct 1979.

[42] C. B. Moler, *Numerical Computing with Matlab*. Society for Industrial and Applied Mathematics, jan 2004.

[43] E. Antonini, *Blood Patterns and Leaflet Motion of the Aortic Valve using Fluid-Structure Interaction*. MSc thesis, Università degli studi di Roma La Sapienza, 2017.

[44] G. PEDRIZZETTI and F. DOMENICHINI, "Flow-driven opening of a valvular leaflet", *Journal of Fluid Mechanics*, vol. 569, p. 321, dec 2006.

[45] D. M. Stevenson, A. P. Yoganathan, and F. P. Williams, "Numerical simulation of steady turbulent flow through trileaflet aortic heart valves–II. Results on five models.", *Journal of biomechanics*, vol. 18, no. 12, pp. 909–26, 1985.

[46] C. Kiris, D. Kwak, S. Rogers, and I.-D. Chang, "Computational Approach for Probing the Flow Through Artificial Heart Devices", *Journal of Biomechanical Engineering*, vol. 119, no. 4, p. 452, 1997.

[47] D. Bluestein, E. Rambod, and M. Gharib, "Vortex Shedding as a Mechanism for Free Emboli Formation in Mechanical Heart Valves", *Journal of Biomechanical Engineering*, vol. 122, no. 2, p. 125, 2000.

[48] A. P. Yoganathan, K. B. Chandran, and F. Sotiropoulos, "Flow in prosthetic heart valves: State-of-the-art and future directions", *Annals of Biomedical Engineering*, vol. 33, no. 12 SPEC. ISS., pp. 1689–1694, 2005.

[49] K. Chandran, G. Cabell, B. Khalighi, and C.-J. Chen, "Laser anemometry measurements of pulsatile flow past aortic valve prostheses", *Journal of Biomechanics*, vol. 16, pp. 865–873, jan 1983.

[50] A. P. Yoganathan, Y.-R. Woo, and H.-W. Sung, "Turbulent shear stress measurements in the vicinity of aortic heart valve prostheses", *Journal of Biomechanics*, vol. 19, pp. 433–442, jan 1986.

[51] W. L. Lim, Y. T. Chew, T. C. Chew, and H. T. Low, "Particle Image Velocimetry in the Investigation of Flow Past Artificial Heart Valves", *Annals of Biomedical Engineering*, vol. 22, pp. 30–318, 1994.

[52] C. Brücker, U. Steinseifer, W. Schröder, and H. Reul, "Unsteady flow through a new mechanical heart valve prosthesis analysed by digital particle image velocimetry", *Measurement Science and Technology*, vol. 13, p. 311, jul 2002.

[53] K. B. Manning, V. Kini, A. A. Fontaine, S. Deutsch, and J. M. Tarbell, "Regurgitant flow field characteristics of the St. Jude bileaflet mechanical heart valve under physiologic pulsatile flow using particle image velocimetry.", *Artificial organs*, vol. 27, pp. 840–6, sep 2003.

[54] Simple real Fourier series approximation - from *MathWorks File Exchange*, https://nl.mathworks.com/matlabcentral/fileexchange/.

[55] Turbulence intensity - from *CFD Online: CFD-WIKI*, https://www.cfd-online.com/Wiki/Turbulence_intensity.

[56] A. Fluent, "15.0 Theory Guide", *Ansys Inc.*, 2013.